

Biomechanics of single cells under compression

Citation for published version (APA):

Peeters, E. A. G. (2004). *Biomechanics of single cells under compression*. [Phd Thesis 1 (Research TU/e / Graduation TU/e), Biomedical Engineering]. Technische Universiteit Eindhoven.
<https://doi.org/10.6100/IR573819>

DOI:

[10.6100/IR573819](https://doi.org/10.6100/IR573819)

Document status and date:

Published: 01/01/2004

Document Version:

Publisher's PDF, also known as Version of Record (includes final page, issue and volume numbers)

Please check the document version of this publication:

- A submitted manuscript is the version of the article upon submission and before peer-review. There can be important differences between the submitted version and the official published version of record. People interested in the research are advised to contact the author for the final version of the publication, or visit the DOI to the publisher's website.
- The final author version and the galley proof are versions of the publication after peer review.
- The final published version features the final layout of the paper including the volume, issue and page numbers.

[Link to publication](#)

General rights

Copyright and moral rights for the publications made accessible in the public portal are retained by the authors and/or other copyright owners and it is a condition of accessing publications that users recognise and abide by the legal requirements associated with these rights.

- Users may download and print one copy of any publication from the public portal for the purpose of private study or research.
- You may not further distribute the material or use it for any profit-making activity or commercial gain
- You may freely distribute the URL identifying the publication in the public portal.

If the publication is distributed under the terms of Article 25fa of the Dutch Copyright Act, indicated by the "Taverne" license above, please follow below link for the End User Agreement:

www.tue.nl/taverne

Take down policy

If you believe that this document breaches copyright please contact us at:

openaccess@tue.nl

providing details and we will investigate your claim.

Biomechanics of single cells under compression

CIP-DATA LIBRARY TECHNISCHE UNIVERSITEIT EINDHOVEN

Peeters, Emiel A.G.

Biomechanics of single cells under compression / by Emiel A.G. Peeters. –
Eindhoven : Technische Universiteit Eindhoven, 2004.

Proefschrift. – ISBN 90-386-2925-7

NUR 954

Subject headings: cell mechanics / nuclear mechanics / cytoskeletal mechanics / cells ; elastic properties / cells ; viscoelastic properties / confocal microscopy / three-dimensional cell deformation / image analysis / mathematical modelling / pressure ulcers / decubitus / laminopathies / nuclear lamins / fibroblasts / C2C12 cells / cell damage / cell loading device / cell compression

Copyright ©2004 by E.A.G. Peeters

All rights reserved. No part of this book may be reproduced, stored in a database or retrieval system, or published, in any form or in any way, electronically, mechanically, by print, photoprint, microfilm or any other means without prior written permission of the author.

Cover design: Calle de Blok/Pieter Lievense/Emiel Peeters.

Printed by Universiteitsdrukkerij TU Eindhoven, Eindhoven, The Netherlands.

Biomechanics of single cells under compression

PROEFSCHRIFT

ter verkrijging van de graad van doctor
aan de Technische Universiteit Eindhoven,
op gezag van de Rector Magnificus, prof.dr. R.A. van Santen,
voor een commissie aangewezen door het College voor Promoties
in het openbaar te verdedigen op
woensdag 7 april 2004 om 16.00 uur

door

Emiel Andreas Godefridus Peeters

geboren te Geldrop

Dit proefschrift is goedgekeurd door de promotoren:

prof.dr.ir. F.P.T. Baaijens

en

prof.dr. D.L. Bader

Copromotor:

dr. C.V.C. Bouten

The uniformity of earth's life, more astonishing than its diversity, is accountable by the high probability that we derived, originally, from a single cell.

Lewis Thomas, 1974

Contents

Summary	xi
1 Introduction	1
1.1 Cell biomechanics	2
1.2 Cell architecture	2
1.3 Experimental studies of cell biomechanics	4
1.4 Objectives	9
1.5 Clinical applications	10
1.5.1 Pressure ulcers	10
1.5.2 Laminopathies	11
1.6 Outline	13
2 A new loading device for compression of single attached cells	15
2.1 Introduction	16
2.2 Materials and methods	17
2.2.1 Experimental equipment	17
2.2.2 Data acquisition	18
2.2.3 Experimental procedure	19
2.3 Results	20
2.3.1 Performance	20
2.3.2 Deformation experiment	23
2.4 Discussion	25
3 Anisotropic, three-dimensional deformation of single attached cells under compression	27
3.1 Introduction	28
3.2 Materials and methods	29
3.2.1 Cell culture	29
3.2.2 Loading device	29
3.2.3 Experimental procedure	31
3.2.4 Data analysis	32
3.3 Results	35
3.4 Discussion	38

3.5	Appendix A, Image analysis validation	41
4	Load-bearing properties of attached cells under compression	43
4.1	Introduction	44
4.2	Materials and methods	45
4.2.1	Cell culture and loading device	45
4.2.2	Experimental procedure	45
4.2.3	Data analysis	46
4.3	Finite element model	47
4.3.1	Assumptions and mesh generation	47
4.3.2	Constitutive equations	47
4.3.3	Estimation of Young's modulus	48
4.4	Results	48
4.5	Discussion	52
5	Viscoelastic properties of single attached C2C12 myoblasts	55
5.1	Introduction	56
5.2	Materials and methods	57
5.2.1	Cell culture and loading device	57
5.2.2	Dynamic experiments	57
5.2.3	Data analysis	58
5.2.4	Viscoelastic model	59
5.3	Results	60
5.4	Discussion	64
6	Decreased mechanical resistance to deformation in cells lacking LMNA gene expression	69
6.1	Introduction	70
6.2	Materials and methods	71
6.2.1	Cell culture	71
6.2.2	Transfection	72
6.2.3	Immunofluorescence studies	72
6.2.4	Actin detection	73
6.2.5	Mechanical compression experiments	73
6.2.6	Confocal laser scanning microscopy	74
6.3	Results	74
6.4	Discussion	83
7	General discussion	87
7.1	Introductory remarks	88
7.2	Loading device	88
7.3	Cell deformation	89
7.4	Mechanical characterisation	91

7.4.1	Load-bearing properties	91
7.4.2	Viscoelastic properties	92
7.5	Clinical applications	93
7.5.1	Pressure ulcers	93
7.5.2	Laminopathies	95
7.6	Future perspectives on cell biomechanics	96
7.7	General conclusions	97
	Bibliography	99
	Samenvatting	117
	Dankwoord	119
	Curriculum Vitae	121

Summary

Eukaryotic cells actively respond to mechanical stimuli. These stimuli and associated cellular deformations induce a variety of biological processes, including morphological changes, differentiation, alterations in gene expression and protein synthesis. The field of cell biomechanics examines how cells move, deform, and interact, as well as how they sense, generate, and respond to mechanical stimuli. Within this field a variety of experimental techniques and computational models may be used. Experimental techniques can be distinguished by their ability to deform the cell either locally or globally.

This thesis focuses on the biomechanics of attached cells, i.e. cells that are anchored to a substrate *in vitro* and to the extracellular matrix *in vivo*. For this purpose, a new loading device was designed to compress single attached cells, either statically or dynamically, while measuring the resulting forces. The design allows global compression of the cell to examine the global mechanical properties, rather than the properties of the substructures of the cell. An advantage of the loading device is its incorporation of optimal culture conditions during compression. In this respect, the device enables the mechanical evaluation of cells in a physiological environment with the potential for long-term experiments. In this thesis, the biomechanical response of single attached cells was examined with reference to two different clinical problems, in which mechanical factors and especially the biomechanics of cells play a major role. The first application involves pressure ulcers and the second focuses on laminopathies.

Pressure ulcers are painful, difficult to treat, and contribute significantly to the health care budget of many countries. Although it is known that they are caused by sustained mechanical loading, the aetiology of pressure ulcers is poorly understood. In particular muscle tissue is highly susceptible to compression and the most severe and problematic pressure ulcers often initiate in the deeper muscle layers. To unravel the mechanobiological pathways leading to cell damage, it is important to study the biomechanical response of single muscle cells to compression. Based on three-dimensional confocal images obtained during stepwise compression of cells, several geometric parameters were calculated to quantify cell deformation. These parameters will be valuable to define threshold levels for cell damage at certain values of cell deformation. The experiments revealed that cells and their nuclei deform perpendicular to their long axis if they have a preferred direction of orientation when attached. It was argued that this anisotropic deformation was caused by orientated actin filaments, which

are indirectly connected to the nucleus and the underlying substrate of the cell.

With respect to the mechanical behaviour of individual muscle cells, two types of experiments were performed. In the first set of experiments, individual cells were compressed completely within 15 seconds. This approach yielded a non-linear force indentation relationship, from which the bursting strength, the corresponding axial deformation and, to a first approximation, the Young's modulus of the cell could be estimated. In the second set of experiments, cells were loaded dynamically to provide information regarding their viscoelastic behaviour. A non-linear viscoelastic model was presented to describe this behaviour. The two experiments revealed the elastic and viscoelastic properties of the muscle cells and provide input parameters for computer models of tissues and engineered tissue constructs. Ultimately, such models will relate local cell deformations to possible damage or adaptation in response to tissue compression as seen in pressure ulcers.

Laminopathies are inherited diseases caused by mutations in the lamin (LMNA) A/C gene. These include, for example, Emery Dreifuss muscular dystrophy, dilated cardiomyopathies, and partial lipodystrophy. While the mechanisms underlying these diseases remain obscure, two major working hypotheses are currently exploited. The first hypothesis states that mutations in A-type lamins cause a loss of gene regulatory functions. The second hypothesis, the *mechanical stress* hypothesis, suggests that patients with laminopathies experience mechanical weakness in cells, caused by a disturbed nuclear architecture. The latter hypothesis was tested using the loading device. Wild-type and LMNA knockout mouse fibroblasts were compared and the former type exhibited a significant higher mechanical resistance to deformation. Simultaneous recordings by confocal microscopy showed that the nucleus in knockout cells was severely damaged after a compression experiment, a finding not observed in wild-type cells. Another important observation was the anisotropic deformation of the nuclei within wild-type cells. By contrast, the nuclei of LMNA knockout cells deformed isotropically. It was proposed that this difference was caused by an impaired attachment of the nuclear envelope to the actin cytoskeleton. Visualisation of actin filaments showed a disturbed actin cytoskeleton around the nucleus of LMNA knockout cells and confirmed this assumption. The present studies revealed a direct correlation between the absence of lamin A-type proteins and cellular fragility, thereby supporting the *mechanical stress* hypothesis.

In conclusion, the loading device and experimental techniques used in this study have proven to be a useful tool to study the biomechanics of attached cells in general, and more specific the aetiology of pressure ulcers and laminopathies.

Chapter 1

Introduction

1.1 Cell biomechanics

All tissues in mammalian organisms are composed of assemblages of cells. Cells in these organisms are subjected to mechanical stimuli either arising from the external or the internal environment of the cell. For example, within the musculoskeletal system, the external environment imposes mechanical stimuli on the cells within muscles, bones, and connective tissues when motion is generated by muscular contractions. Within the cardiovascular system, endothelial cells are exposed to shear stresses, whereas cardiac cells and vascular smooth muscle cells are subjected to stretch due to the beating heart. Especially in attached cells, which are physically connected to the surrounding extracellular matrix, the mechanical stimuli of the external environment are directly transferred to the cell. The internal environment imposes mechanical stimuli by the conversion of chemical energy into mechanical energy. Mechanical energy is actively generated during processes such as attachment, spreading, and motility of cells. Another example is the active contraction of muscle cells by the sliding of actin filaments against myosin filaments.

Cells positively respond to mechanical stimuli by changing their own behaviour and by modifying their environment. For example, forces applied to the cell and the consequent cellular deformations induce a variety of processes, including morphological changes, growth (Clarke and Feedback, 1996), differentiation (Vandenburgh, 1992), secretion (Perrone et al., 1995), gene expression (Frenette and Tidball, 1998) and altered extracellular matrix production (Mol et al., 2003). This response can either lead to cell adaptation to counteract the effect of the applied stimuli or to cell damage or death when the applied stimuli exceed the adaptive capacity of the cell.

The field of cell biomechanics studies how cells move, deform, and interact, as well as how they sense, generate, and respond to mechanical stimuli (Zhu et al., 2000). Both experimental approaches and computational approaches are used to investigate these processes. The former use a variety of loading techniques to deform the cell and to determine its mechanical properties or to examine adaptation or damage phenomena. Computational approaches, including mechanical models of the cell or the cell and its external environment are of particular value in predicting how mechanical stimuli are transferred from the external environment to the cell and distributed throughout the cell and vice versa. Both approaches contribute not only to the knowledge of how healthy cells respond to mechanical stimuli, but also provide an insight into the pathogenesis of specific diseases by examining the mechanical response of diseased cells (Thoumine and Ott, 1997a; Wu et al., 2000).

1.2 Cell architecture

This section covers the most important cellular structures, relevant for the mechanical properties and mechanical integrity of the cell.

All mammalian cells are surrounded by a plasma membrane, providing a barrier

between the internal and the external environment. It consists of a lipid bilayer and proteins, which regulate transport of specific molecules into and out of the cell. Some membrane proteins, such as members of the integrin family, link the membrane to the internal cytoskeleton and/or to proteins of the extracellular matrix or to an adjacent cell (Luna and Hitt, 1992; Yamada and Miyamoto, 1995; Maniotis et al., 1997).

The cell interior, excluding the nucleus, is called the cytoplasm and is composed of the largely aqueous cytosol and cell specific organelles, such as mitochondria and the endoplasmic reticulum. A complex network of protein filaments extending throughout the entire cell and/or bound to the plasma membrane constitutes the cytoskeleton. It provides a continuous, dynamic connection between nearly all cellular structures (Maniotis et al., 1997; Janmey, 1998).

The cytoskeleton is involved in regulating cell shape, resistance to deformation, and elasticity as well as in active processes such as cell division, locomotion, and the transport of intracellular particles (Elson, 1988). Furthermore, the cytoskeleton is believed to be involved in many cell signalling processes (Ben-Ze'ev, 1991; Ingber, 1997). It consists of microfilaments (F-actin), microtubules, and intermediate filaments (IF's) composed of, respectively, three chemically distinct subunits, actin, tubulin, and a family of related fibrous proteins, such as vimentin and lamin. The localisation of the three types within the cell is schematically shown in figure 1.1.

F-actin assembles in a variety of structures including isotropic networks of filaments within the cytoplasm, contractile actin filament bundles often called stress fibres and highly organised parallel arrays of filaments in such structures as microspikes (thin, stiff protrusions of the plasma membrane) and lamellipodia (sheet-like extensions on the cell surface). Actin filaments are thin, typically 8 nm in diameter, flexible and appear to be the most resistant of the cytoskeleton elements to deformation, but rupture and begin to flow at high strains (Janmey et al., 1991).

Microtubules are long, hollow, rigid cylinders with extreme outer and inner diameters of 30 and 18 nm respectively, and with lengths of up to and exceeding 100 μm . They extend throughout the cytoplasm and determine the location of membrane-bound organelles and other cell components (Alberts et al., 1994). It is believed that microtubules serve as stabilising elements within a network of the other two cytoskeletal filaments (Janmey et al., 1991). Although individual microtubules are stiff and rigid over cellular dimensions (Gittes et al., 1993), microtubule networks are easily deformed and begin to flow when stretched beyond 50 % of their original length (Janmey et al., 1991).

IF's are tough and durable fibrous proteins, which are organised in ropelike arrays and have a typical diameter of 10 nm, intermediate between thin actin filaments and thick microtubules. They can be found around the nucleus, extending out through the cytoplasm and eventually forming close associations with the cell membrane at the cell adhesion sites (Goldman et al., 1996). Moreover, IF's also appear as a fibrous protein meshwork underlying the inner nuclear membrane. These so-called nuclear lamins are believed to be connected to the nuclear membrane and other cytoskeletal elements (Penman, 1995; Stuurman et al., 1998). IF's are specifically found in cells, which are regularly subjected to mechanical stresses, like epithelial cells and all kinds of muscle

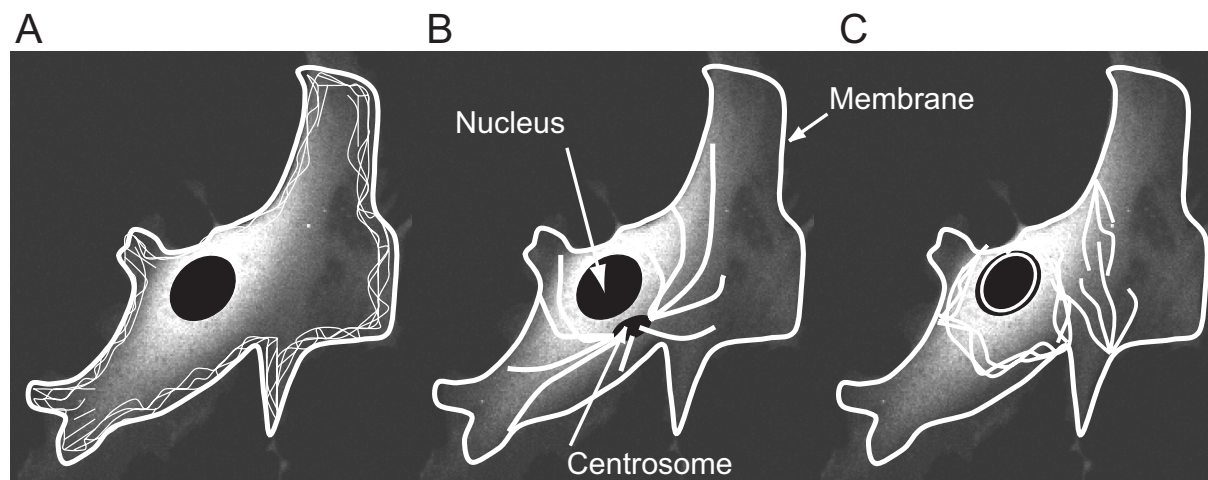


Figure 1.1: Distribution of the three filament types, which form the cytoskeleton: F-actin (A), microtubules (B) and intermediate filaments (C). At the centrosome, microtubules elongate randomly towards the periphery of the cell. The intermediate filaments also form a lamina around the nucleus.

cells. Moreover, disassembly of IF's is accompanied by dramatic changes in shape and mechanical properties of the cell (Goldman et al., 1998).

The nucleus of all mammalian cells consists of a nuclear envelope surrounding the nucleoplasm, with distinct components such as the inner and outer nuclear membrane, the nuclear lamina, and the nuclear pore complexes (Stuurman et al., 1998). From a structural point of view, the nucleus is mechanically stiffer than the cell cytoplasm (Guilak et al., 2000; Caille et al., 2002).

1.3 Experimental studies of cell biomechanics

The biomechanics of cells has been studied using a wide range of experimental techniques, loading cells in a variety of ways appropriate to their *in vivo* environment. They provide a well-controlled method to examine contributions of biochemical and physical factors, e.g. nutrition, temperature, degree of cellular attachment, drugs, and damage induced by diseases. An important issue in examining these characteristics is to identify the contribution of the different cellular components to the mechanical response.

This section will only review techniques in which single cells are directly deformed. For indirect loading, or simultaneous loading of groups of cells the reader is referred to review articles by Brown (2000) and Tran-Son-Tay (1993).

The direct loading techniques may be classified into two distinct groups:

1. techniques designed for local loading of single cells and
2. techniques designed for global loading of cells.

Tables 1.1 and 1.2 summarise the most commonly used techniques and their characteristics. In general, local loading of cells reveals the mechanical properties of certain structures or parts of cells (atomic force microscopy, cell poking), or the force transmitting chains within cells (microbead manipulation). However, for some applications it is more important to evaluate the properties of the cell as a whole, as opposed to the properties of the substructures of the cell. In those cases, it is necessary to use a technique for global loading of single cells.

It must be stated that different techniques often provide a range of results, even for the same cell type (Bader et al., 2002; Laurent et al., 2002). This phenomenon may be attributed to the structures, which are deformed during these different experiments. For example, an atomic force microscope indents a small part of the cell membrane and underlying actin filaments of the cytoskeleton, whereas microplates compress the membrane, the underlying cytoskeleton, and the nucleus.

One of the most frequently used techniques involves micropipette aspiration. However, this technique is often applied to investigate suspended cells, even though most cells are anchored to the extracellular matrix *in vivo* and are attached to a substrate *in vitro*. Therefore, loading of attached cells is often physiologically more relevant. Moreover, deformation of attached cells depends much more on cytoskeletal and environmental conditions, than that of suspended cells (Wang and Ingber, 1994; Choquet et al., 1997; Thoumine and Carodoso, 1999). The mechanical properties of attached cells are usually examined by either compression of specific parts of the cell with a small indenter (cell poker or atomic force microscopy) or compression of the complete cell with an indenter with a comparable size to the cell (microplates or micromanipulation).

Many experiments have revealed the viscoelastic nature of the cell (Elson, 1988). Furthermore, a number of studies has highlighted differences in the mechanical and deformation properties between healthy cells and their diseased counterparts (Thoumine and Ott, 1997a; Jones et al., 1999; Wu et al., 2000). The measured forces range from several piconewtons to micronewtons, whereas deformations range from several nanometers to micrometers.

Although most studies have been performed at room temperature, cells in organisms and in culture exist at a temperature of 37 °C. Several studies have shown the influence of temperature on the mechanical properties (Petersen et al., 1982; A-Hassan et al., 1998). Another important feature of many of the techniques is that few provide an optimal, physiological environment (tables 1.1 and 1.2). To keep cells viable for several hours, temperature, humidity (avoiding evaporation) and level of CO₂ should be controlled.

Visual observations of cellular deformations are often made using conventional brightfield microscopy, providing information of cell deformation in two-dimensions.

This necessitates the assumptions that the shape of the cell is spherical or at least axisymmetric. However, this is not the case for attached cells, which often have rather irregular shapes. The use of confocal microscopy has the potential to provide full three-dimensional information of cell deformation. Moreover, fluorescent labelling of specific cellular components or proteins would increase the knowledge concerning local deformations within the cell and the contribution of the individual components of the cell (Cubitt et al., 1995; Guilak et al., 1995; Gerdes and Kaether, 1996; Lee et al., 2000; Arnoczky et al., 2002).

Based on the limitations of existing techniques and requirements listed above, an improved technique to directly load single cells should be able to:

- perform experiments on attached cells,
- reveal global cell mechanical properties,
- maintain cell viability for several hours by providing an optimal, physiological environment,
- impose deformations at the micro- and nanometer scale,
- measure forces at the micro- and nanonewton scale,
- visualise the cells and sub-cellular structures using confocal laser scanning microscopy,
- quantify the elastic properties of cells,
- perform dynamic or relaxation experiments, to quantify the viscoelastic properties of cells, and
- examine changes in the mechanical and deformation characteristics between healthy cells and cells subjected to disease, trauma or genetic modifications.

These features are currently only partly satisfied by the existing experimental techniques.

Besides experimental techniques, mechanical models are used in studies of cell biomechanics. They aim to describe and quantify the mechanical properties of cells. These models provide a way to investigate the influence of specific biophysical factors on the biomechanical response of cells. Moreover, they provide both valuable information on the intra- and extracellular loading condition of the cell and a means to compare outcomes of different experimental studies.

Table 1.1: Characteristics of loading techniques designed for local loading of cells.

	partial micropipette aspiration	cell poking	AFM	bead micro-manipulation
cell presentation	suspended cells	spread cells	spread cells	spread cells
physical principle	suction of part of cell	indentation	indentation	twisting (T) or moving (M) of attached microbeads with magnetic field or laser tweezers
control of	pressure	axial deformation	force or axial deformation	torque or force
size of load applicator	NA	2 μm	pyramid shape, radius of curvature < 50 nm	bead diameter: 0.2-5.5 μm
force / pressure / torque range	~ 0.01 -1 kPa	5-400 nN	pN-nN	20 pN - 10 nN (M), 0.1-10 Pa (T), pN. μm -nN. μm (T)
deformation range	depends on cell/pipette diameter ratio	max 50 %	max 10 %	max 2 μm (M), max 10 $^\circ$ (T)
resolution	0.2 μm , 0.1 Pa	0.02 μm , 5 nN	nm, pN	0.1 μm (M), 1 pN (M), 20 pN. μm (T)
visualisation	brightfield microscopy	brightfield microscopy	brightfield, confocal microscopy	brightfield, fluorescence, confocal microscopy
operating temperature	RT	RT and 37 $^\circ\text{C}$	RT and 37 $^\circ\text{C}$	RT
controlled environment?	no	no	no	no
references	1,2,3	4,5	6,7,8	9,10,11,12,13

RT=room temperature, NA=not applicable.

References are 1: Wu et al. (2000), 2: Guilak et al. (2002), 3: Sato et al. (1990), 4: Petersen et al. (1982), 5: McConnaughey and Petersen (1980), 6: Alcaraz et al. (2003), 7: Mathur et al. (2001), 8: Sato et al. (2000), 9: Laurent et al. (2002), 10: Puig-De-Morales et al. (2001), 11: Bausch et al. (1998), 12: Yamada et al. (2000), 13: Wang and Ingber (1994).

Table 1.2: Characteristics of loading techniques designed for global loading of cells.

	full micropipette aspiration	microplates	micro-manipulation	cyto-indentation
cell presentation	suspended cells	suspended and semi-spread cells	suspended and spread cells	spread cells
physical principle	suction of complete cell	unconfined compression and traction	unconfined compression	unconfined compression
control of	pressure	axial deformation	axial deformation	force
size of load applicator	NA	width=20 μm , length > 100 μm	50 μm	5 μm
force/pressure range	$\sim 0.1\text{-}2$ kPa	$1\text{-}1.10^3$ nN	10 nN-50 μN	1-100 nN
deformation range	depends on cell/pipette diameter ratio	max 50 %	total cell compression	NR
resolution	0.2 μm , 0.1 Pa	0.12 μm , 1 nN	0.2 μm , 10 nN	0.1 μm , 1 nN
visualisation	brightfield microscopy	brightfield microscopy	brightfield microscopy	brightfield microscopy
operating temperature	RT	RT	37 °C	RT
controlled environment?	no	no	no	no
references	1,2,3	4,5	6,7	8

RT=room temperature, NA=not applicable, NR=not reported.

References are 1: Jones et al. (1999), 2: Needham and Hochmuth (1990), 3: Evans and Yeung (1989), 4: Thoumine et al. (1999), 5: Thoumine and Meister (2000), 6: Zhang et al. (1991), 7: Zhang et al. (1992), 8: Koay et al. (2003).

1.4 Objectives

The present thesis examines the biomechanics of single attached cells under compression. In order to compress single attached cells, *the first objective is to develop a new experimental technique, fulfilling all the characteristics as described in section 1.3.*

Because deformation of cells is believed to influence their biochemistry, function and structure (Watson, 1991), it is important to quantify cell deformation. Only then it is possible to quantitatively relate cell deformation with changes in these three properties. As the deformation of attached cells has to be quantified, it is not appropriate to assume either a spherical or axisymmetric cell shape or to consider two-dimensional deformations alone. Therefore, *the second objective of this thesis is to quantify the three-dimensional deformation of single attached cells under compression.* Confocal microscopy combined with custom made image analysis software is required to observe and quantify cell deformation.

The degree of cell deformation largely depends on the mechanical properties of the cell. The mechanical properties can be subdivided into elastic and viscoelastic properties. *The third objective is to investigate the elastic mechanical properties.* These properties can be characterised by measuring the force versus strain relationship and the maximum force at breakdown of cells under compression at relatively low rates of compression (Zhang et al., 1992). This requires global loading of single cells by applying large deformations while measuring the associated forces, which can be accomplished using a loading device.

As cells are viscoelastic, *the fourth objective is to quantify the viscoelastic properties of single attached cells.* Dynamic experiments need to be conducted with a loading device and a viscoelastic model could be used to quantify these properties.

The mechanical properties are largely dependent on the cells and their sub-cellular structures, which can be altered by, for example, adaptation, specific diseases or mechanically induced cell damage. *The fifth objective is to detect changes in the deformation behaviour and mechanical properties of cells, which lack a specific protein thought to be important in maintaining cellular integrity.* Therefore, compression experiment could be performed on cells with and without A-type lamins. From these experiments it can be derived whether there are differences in the load-bearing properties between these cells. Furthermore, differences in deformation behaviour and damage as a result of large deformations could be observed using confocal microscopy.

1.5 Clinical applications

In this thesis, the biomechanical response of single attached cells is examined with reference to two different clinical problems, in which mechanical factors and especially the biomechanics of cells play a major role. The first application involves pressure ulcers and the second focuses on laminopathies.

1.5.1 Pressure ulcers

Pressure ulcers are defined as localised areas of degenerated skin and underlying soft tissues, caused by sustained mechanical loads (APUAP, 1989). They mainly affect patients who are bedridden, wheelchair bound or wear orthoses or prostheses. Prevalence figures range between 14 % and 33 % in health care institutions (Bours et al., 2002). Pressure ulcers are very painful and difficult to treat. Furthermore, because of the expensive preventive and treatment measures and costs of extended hospitalisation periods, they contribute significantly to the health care budget of many countries.

Pressure ulcers may be classified into two types:

1. superficial ulcers
2. deep ulcers.

Superficial ulcers develop within the skin layer and may or may not progress towards deeper layer, whereas deep ulcers are initiated in underlying muscles and progress towards the skin surface (Kosiak, 1961; Daniel et al., 1981; Bouten et al., 2003b). Skeletal muscle tissue degeneration starts at the cellular level and is characterised by nuclear pyknosis and an early disintegration of the contractile proteins in the cells, followed by inflammatory reactions (Kosiak, 1961; Nola and Vistnes, 1980; Bouten et al., 1999). Superficial ulcers are predominantly caused by shear stresses within the skin layers, whereas deep ulcers are mainly caused by sustained compression. Deep ulcers show extensive ulceration, develop faster and are more harmful and more difficult to prevent and treat than superficial ulcers (Nola and Vistnes, 1980; Daniel et al., 1981; Bliss, 1993). Furthermore, muscle tissue is highly susceptible to sustained compression applied at the skin surface (Nola and Vistnes, 1980).

Despite considerable efforts to prevent pressure ulcers, data on prevalence are still unacceptably high. A better understanding of the aetiology of pressure ulcers can decrease the prevalence and provide more effective ways to prevent and identify patients at risk (Barbenel, 1991; Bouten et al., 2003b). Several theories have been proposed to explain the onset of pressure ulcers, involving localised ischaemia, impaired interstitial fluid flow and lymphatic drainage, reperfusion injury, and sustained deformation of cells (Bouten et al., 2003b).

The work described in this thesis is part of a research programme at the Eindhoven University of Technology, which aims at the understanding of the basic pathways whereby mechanical loading leads to soft tissue breakdown in the form of pressure

ulcers. The research conducted in this project mainly focuses on skeletal muscle tissue in which deep ulcers initiate. It is hypothesised that sustained deformation of cells is the main trigger for the development of pressure ulcers. To verify this hypothesis, a hierarchical approach is adopted, incorporating studies ranging from the level of individual cells to tissues, animals, and humans (Bouten et al., 2003a,b). Studying the properties of individual muscle cells in culture is an essential part of this programme.

A major advantage of studying the aetiology of pressure ulcers at the cellular level is that their response to compression can be studied independent of effects from neighbouring cells, extracellular matrix, three-dimensional tissue architecture, perfusion, and lymph flow (Bouten et al., 2003a,b).

To obtain insight into the aetiology of deep ulcers, it is important to know how externally applied loads to the skin are transferred to the local environment that the cell experiences within the tissue (Breuls et al., 2002). This can be achieved using multi-level models, which require the identification of the mechanical properties of the complete cell. Apart from the mechanical properties of single cells, it is important to relate sustained cell deformation with the onset of cell damage, either reversible or irreversible. Only then it is possible to test the hypothesis at the cellular level and relate this to the findings of studies at the tissue, animal, and human level. As a start, this requires the quantification of cell deformation. Therefore, in this thesis the mechanical response of single muscle cells to compression has been examined, *to elucidate how cells deform under compression and to estimate their elastic and viscoelastic mechanical properties.*

1.5.2 Laminopathies

Laminopathies are inherited diseases, which are related to mutations in the LMNA gene causing disorders of the nuclear lamina. These diseases include, for example, dilated cardiomyopathy, limb girdle dystrophy, partial lipodystrophy, Emery-Dreifuss muscular dystrophy (Bonne et al., 1999), and Hutchinson-Gilford progeria (Eriksson et al., 2003; Mounkes et al., 2003). A review of laminopathies can be found in Burke and Stewart (2002), Genschel and Schmidt (2000), and Worman and Courvalin (2002).

The LMNA gene encodes A-type lamins (lamin A, lamin A Δ 10, and lamin C). As previously described in section 1.2, the nuclear lamins are members of the family of IF's and form a sheet-like network underlying the inner nuclear membrane of virtually all cells (Stuurman et al., 1998). The A-type lamins are mainly expressed in cells with a high degree of differentiation and/or absence of proliferation. The nuclear lamina is associated with the inner nuclear membrane via lamina-associated proteins, and is also directly or indirectly connected to chromatin and nuclear pore complexes (figure 1.2) (Gruenbaum et al., 2000). Nuclear pore complexes mediate and regulate transport between the cell nucleus and the cytoplasm (Görlich and Kutay, 1999). Furthermore, interaction of lamins with nesprins has been recently reported (Zhang et al., 2001). Nesprins are large proteins localised near the nuclear envelope, in the nucleus and the cytoplasm where they bind directly to actin (Zhang et al., 2002). The nuclear lamina

is required for normal cell cycle regulation, chromatin organisation, DNA replication, cell differentiation, apoptosis, maintaining nuclear shape, and spacing nuclear pore complexes (Gruenbaum et al., 2000; Cohen et al., 2001).

To explain the development of these inherited diseases, two major hypotheses are currently under discussion. In the first hypothesis, lamins A and C are considered to be essential for the correct tissue-specific expression of certain genes. Therefore, a pathogenic mechanism for these diseases might be a disorder in gene regulation caused by mutations in lamins A and C (Worman and Courvalin, 2002). This disorder can result in dedifferentiation and increased proliferation of certain subsets of cells. The second hypothesis suggests that patients with laminopathies experience mechanical weakness in cells, caused by a disturbed nuclear architecture. This *mechanical stress* hypothesis could explain the loss of muscle tissues at the onset of adulthood in affected patients as seen in the group of muscle failure-related diseases.

In this thesis, this last hypothesis is tested using wild-type and LMNA knockout mouse fibroblasts. The objectives of this study are to:

- reveal nuclear fragility in LMNA knockout cells as reflected by differences in the mechanical properties of these cells compared to their normal, healthy counterparts, and
- observe differences in the deformation behaviour and the associated damage of the nuclei in these cells when subjected to relatively high mechanical stresses.

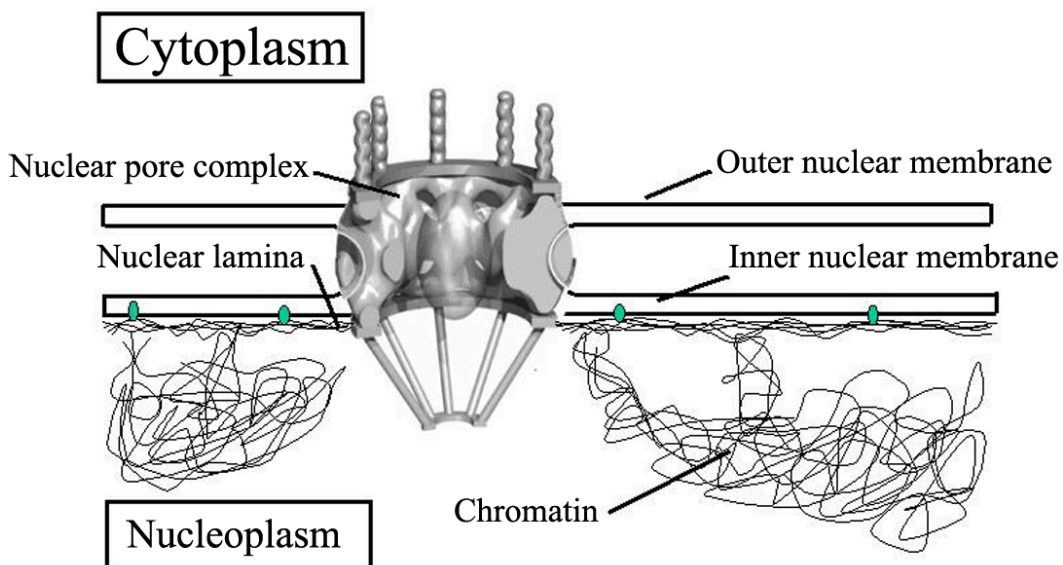


Figure 1.2: Schematic representation of the nuclear lamina and its connections with other nuclear components.

1.6 Outline

Chapters 2, 3, 4, and 5 are largely directed towards pressure ulcers, although the methods and techniques can be relevant to many other applications in the field of cell biomechanics. In these chapters, the biomechanical response of C2C12 mouse myoblasts is examined.

In chapter 2, a new loading device to compress single attached cells is presented. The characteristics, performance, and possible applications of this device are detailed.

The anisotropic, three-dimensional deformation of attached cells under compression is described in chapter 3. Deformation is characterised in both quantitative and qualitative terms, based on confocal images and three-dimensional image reconstruction. A shape factor is introduced, which describes the roundness of the cell and quantifies the anisotropic deformation as observed during compression of these cells.

The load-bearing properties of attached cells under compression are determined in chapter 4. The mechanical resistance of cells to compression is given by measuring the force versus axial strain relationships. Furthermore, damage of the cells during compression experiments is characterised in terms of the bursting strength at cell rupture and the accompanying axial deformation.

Chapter 5 describes the viscoelastic behaviour of single muscle cells under compression. Dynamic experiments are performed over two frequency decades (0.1-10 Hz) and at different axial strains ($\sim 10 - 40\%$). Viscoelastic behaviour is quantified using a non-linear viscoelastic model. The model is composed of a single spring in parallel with a Maxwell element, consisting of a non-linear spring in series with a dashpot.

Chapter 6 is directed towards the second clinical application, namely the laminopathies. The *mechanical stress* hypothesis is tested by performing compression experiments on wild-type and LMNA knockout mouse fibroblast. The latter cell type lacks an important structural protein, believed to maintain nuclear integrity: A-type lamins. The load-bearing properties of the two cell types are determined and confocal imaging is used to compare the deformation behaviour and damage characteristics of their nuclei.

Finally, chapter 7 discusses the overall results from the thesis and suggests recommendations for future work, with a focus on the developed technique and cell mechanics in general and specifically on pressure ulcers and laminopathies.

Chapter 2

A new loading device for compression of single attached cells

The contents of this chapter are based on Peeters et al. (2003), "*Monitoring the biomechanical response of individual cells under compression: a new compression device*", *Medical and Biological Engineering and Computing*, **41**, pp. 498-503.

2.1 Introduction

Studies investigating soft tissue damage in animals, have shown that skeletal muscle tissue is highly susceptible to sustained compression (Nola and Vistnes, 1980; Caplan et al., 1988). Depending on its magnitude and duration, the applied load causes tissue breakdown in the form of pressure ulcers (Barbenel, 1991). This breakdown starts at the cellular level and is characterised by damage to the cell membrane and nucleus, followed by inflammatory reactions (Bouten et al., 1999). Previous studies have mainly focused on the biochemical environment of the cells (Daniel et al., 1981; Krouskop, 1983). These studies state that occlusion of lymph and blood vessels within the tissue impairs transport of nutrients and waste products from and to the cell. Although these factors contribute to cell damage, Bouten et al. (2001) showed that sustained cell deformation plays a significant role in the breakdown of muscle tissue, regardless of the nutrient and oxygen supply. However, the mechanisms whereby cell compression causes cell damage remain unclear. To better understand this process, a method has to be developed to compress individual muscle cells and monitor their biomechanical response.

The biomechanical response can be subdivided into structural, mechanical and biochemical changes (Davies and Tripathi, 1993). For example, mechanical forces can induce cytoskeletal remodelling, thereby changing the internal structure and organisation of the cell (Elson, 1988; Galbraith et al., 1998). On the other hand, the structure and organisation of the cell and its environment influence the mechanical properties of the cell (Chen and Ingber, 1999). Obvious evidence for this fact is the stiffening effect during spreading of cells and the relatively high contribution to the cell stiffness from certain structures like the nucleus (Thoumine and Ott, 1999; Caille et al., 2002). Furthermore, mechanical forces not only deform cells, but also induce biological responses, thereby altering their function (Ingber, 1997). For example, mechanical forces influence growth, gene expression and protein synthesis (Komuro et al., 1991; Vandeburgh, 1992).

To understand the biomechanical effects of cell deformation, several experimental devices have been developed. These include micromanipulation techniques, micropipette aspiration, atomic force microscopes, magnetic bead manipulation techniques, and cell pokers (Petersen et al., 1982; Sato et al., 1990; Zhang et al., 1991; Dong and Skalak, 1992; Frangos, 1993; Wang et al., 1993; Moore, 1994; Haga et al., 2000). These devices and techniques increased the understanding of how mechanical forces influence cell function. Of course, the design of these devices depends on the research applications and the *in vivo* loading situation they mimic (Brown, 2000). However, none of the devices is able to monitor the biomechanical response of whole cells during long-term, unconfined compression.

The goal of the present study was to develop a device, which is suitable to monitor the biomechanical response of skeletal muscle cells to sustained cell deformation. The developed device is able to measure the mechanical properties of cells and visualise the cell during compression. Design features include the potential for dynamic testing by using a nanopositioning system based on piezo-actuators. For long-term experiments,

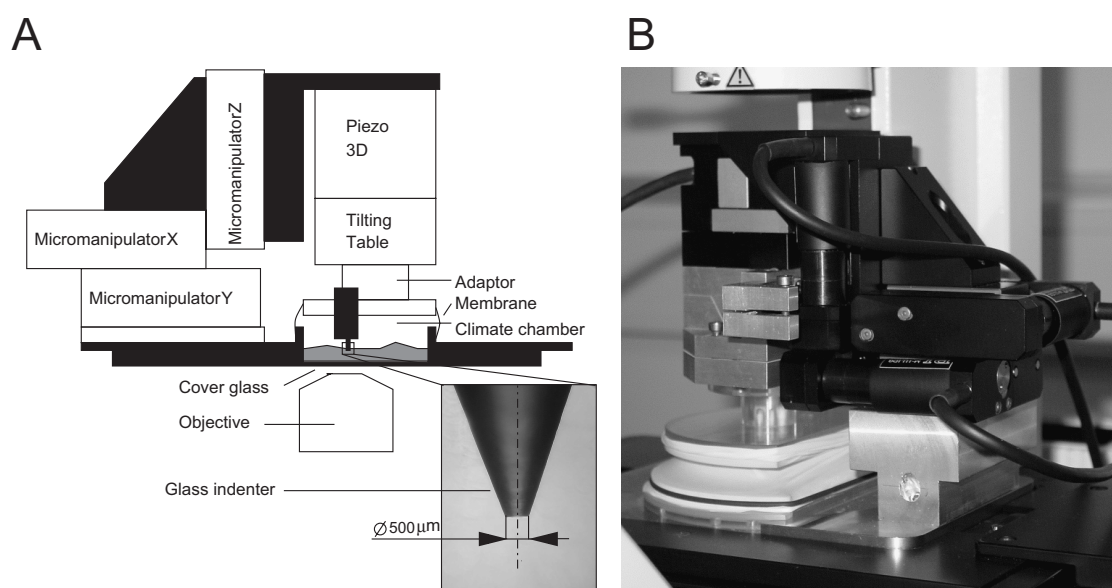


Figure 2.1: A: Schematic representation of the loading device. The insert shows a close-up of the glass probe.

B: Actual realisation of the loading device. The device is located on the motorised stage of an inverted microscope, allowing visualisation of the cell during compression.

the loading device is equipped for control of temperature and CO₂. In this paper, the device is evaluated and results of preliminary compression experiments are reported.

2.2 Materials and methods

2.2.1 Experimental equipment

The device for unconfined compression of individual cells is shown in figure 2.1. It consists of a stainless steel frame resting on a motorised stage of an inverted microscope (Axiovert 100M, Zeiss, Germany) with a confocal laser scanning unit (LSM 510, Zeiss). Normal cover glasses (25 mm in diameter) can be inserted in a polycarbonate chamber (3 mm deep and 25 mm in diameter) of the stainless steel frame. Cells on the cover glass are compressed using a glass indenter (20 mm long and 5 mm in diameter), which has a flat polished surface with a diameter of 500 μm (see insert in figure 2.1 A). The indenter is connected to a tilting table via a polycarbonate adaptor. The tilting table can twist the adaptor plate around two axes in the horizontal plane at a maximum of 2 degrees. This ensures that the glass indenter is parallel with respect to the cover glass.

For fine positioning of the indenter, the tilting table is attached to a closed-loop nanopositioning system (Nanocube P-611.3S, Physik Instrumente, Germany) with a range of 100 μm and a resolution of 5 nm. It consists of three piezo-actuators and three strain-gage position feedback sensors, integrated in a flexure guiding package. To displace the indenter over a wider range, the nanopositioning system can be moved using three micro-translation stages (M-111.DG, Physik Instrumente), which incorporate closed-loop DC motors (range: 15 mm, minimum incremental motion: 50 nm).

The system also incorporates a climate chamber designed to create an optimal environment for the cells, comparable to that of a CO_2 incubator. For example, a water canal surrounding the cover glass keeps the temperature of the culture medium inside the polycarbonate chamber at 37 °C. The water is heated in a reservoir and pumped through the canal by a roller pump. Furthermore, a membrane spanning the gap between the chamber and the adaptor isolates the chamber from the environment. A Zeiss CTI-controller (Zeiss, Germany) with humidifier supplies the chamber with heated, humidified air containing 5 % CO_2 .

For mechanical characterisation, the adaptor is replaced by a force transducer (model 406A, Aurora Scientific Inc., Canada) with a full-scale range of 500 μN and a resolution of 10 nN. Specifications of the total system are summarised in table 2.1.

Table 2.1: Specifications of the single cell loading device.

Maximum displacement	15 mm
Minimum displacement	5 nm
Maximum force	500 μN
Minimum force	10 nN
Compliance force transducer	10 nm/ μN
Frequency range	0-25 Hz
Thermal stability culture chamber	± 0.5 °C

2.2.2 Data acquisition

An overview of the data-acquisition system is shown in figure 2.2. The compression device is controlled by a personal computer with two 16-bit data-acquisition boards (PCI-6052E, National Instruments, USA) and a motor controller PC board (C-842, Physik Instrumente, Germany). The latter, in combination with a keyboard or joystick, is used to control the position of the three micro-translation stages.

The input voltage for each piezo-actuator of the nanopositioning system is supplied by a low-voltage piezo amplifier module (E- 503.00, Physik Instrumente) and is controlled by applying an analogue signal from the data-acquisition board to the input of the amplifier. A displacement sensor module (E-509, Physik Instrumente) with an integrated

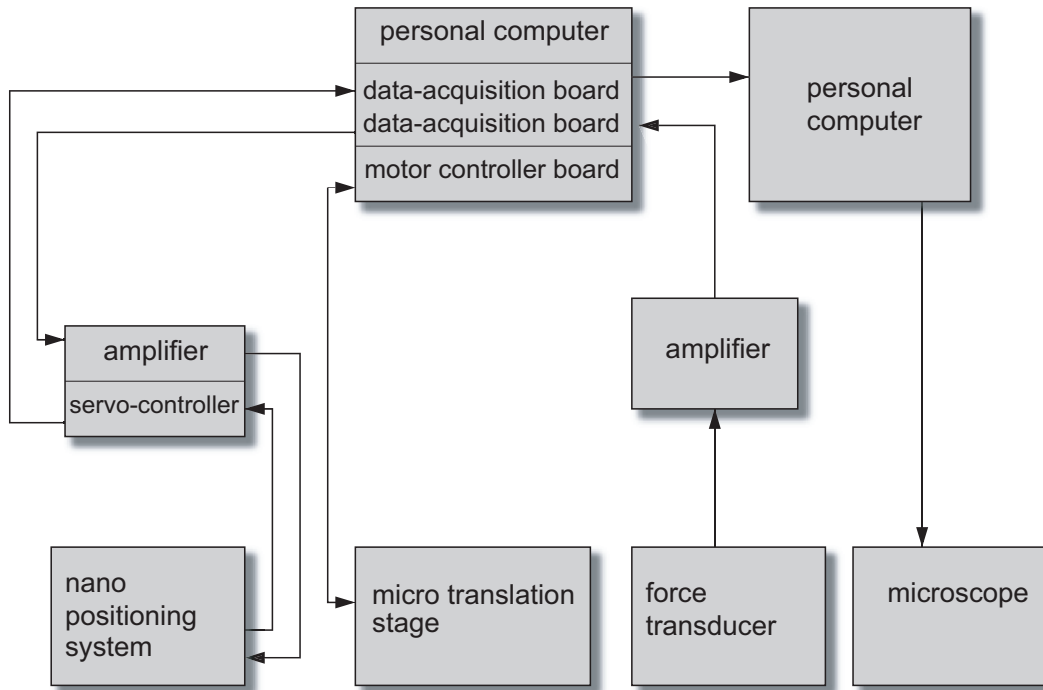


Figure 2.2: Schematic diagram of the acquisition system. The total experimental setup is controlled by two personal computers. Custom software written in LabVIEW allows the user to control the setup, and record data from the piezo-actuators, micro-translation stages and force transducer.

position servo controller compensates for hysteresis and drift of the piezo-actuators in the nanopositioning system. The actual position of the piezo-actuators can be read from the output signal of the servo controller and is sent to the data-acquisition board. The data-acquisition board also records the output signal from the amplifier of the force-transducer. A second personal computer controls the inverted microscope. Images of the cell are recorded, if the data-acquisition card of the other computer supplies an analogue trigger signal. Custom software written in the graphical programming language LabVIEW (National Instruments, USA) controls the whole setup and samples the signals from the force transducer and servo controller with a sample time between 0.001 and 0.01 seconds.

2.2.3 Experimental procedure

In this study, the established C2C12 mouse skeletal myoblast line (ECACC, UK) is used for compression experiments. Cells are seeded at low densities (20,000 cells/cm²) on cover glasses and cultured following a standard culturing protocol (McMahon et al., 1994). After one day in culture, the cells are stained for 25 minutes with 7.5 μ M Cell Tracker

Green (Molecular Probes, Leiden, the Netherlands) and a cover glass with cells is inserted into the polycarbonate chamber of the compression device. Fresh growth medium is added and, after attachment of the membrane, the device is placed on the microscope stage and connected to the CTI-controller. Using the three micromanipulators, the glass indenter is positioned just above a single myoblast and a three-dimensional scan is made of the undeformed cell. Then the glass indenter is moved to the top of the cell by the piezo-actuators. During the actual compression experiment, the glass indenter is lowered in steps of 2 μm by the piezo-actuators until the cell bursts. After each step a complete stack of confocal images is recorded to visualise cell deformation.

For confocal imaging, the cells are visualised using a 20x, 0.5 numerical aperture objective (Plan Neofluar, Zeiss, Germany). The stain is excited using an Argon ion laser with an excitation of 1 % at 488 nm and a tube current of 6 A. Emission is recorded above 510 nm. Three-dimensional images of the cell are recorded at a sampling distance (x, y, z) of 0.22x0.22x0.75 μm . The value of the eight-bit digitised signal is kept below a grey level value of 250 to avoid electronic saturation of the photomultipliers. A full width half maximum (FWHM) threshold defines the boundary of the cell. With the aid of a custom software program in Matlab (Mathworks, USA), a three-dimensional rendered image is produced and the width, volume, and surface area of the cell are calculated before and after compression.

2.3 Results

2.3.1 Performance

As a skeletal muscle cell is relatively thin compared to its length, any angular twist of the indenter will result in an unequal compression of the cell. Non-parallelism of the indenter is caused by bending of the different components of the device, such as the micromanipulators and piezo-actuators. Determination of the twist angles α and β of the indenter is achieved using the confocal microscope in reflection mode (see figure 2.3). Typical values for both angles vary between 0 and 1 degrees, resulting in a maximum Δz of 8 μm . Before conducting any experiment, the twist angles were returned to zero using the tilting table.

For dynamic experiments, it is important that the nanopositioning system is capable of generating an accurate sine wave and step-like signal. Therefore, a pulse generator is used to generate a sine wave and a square wave, both with an amplitude of 5 μm , an offset of 5 μm and frequency of 5 Hz. The response of the nanopositioning system as a result of the two input signals is shown in figure 2.4. The time delay between the input signal of the pulse generator and the output signal of the servo controller was approximately 0.03 s. The maximum difference between these signals was approximately 0.03 V, corresponding to 300 nm. Noise levels of the servo controller corresponded with the specifications of the data-acquisition board, which has a relative accuracy of 1145 μV (~ 11.5 nm) at a measurable range of -10 to +10 Volt. This implies that any noise is

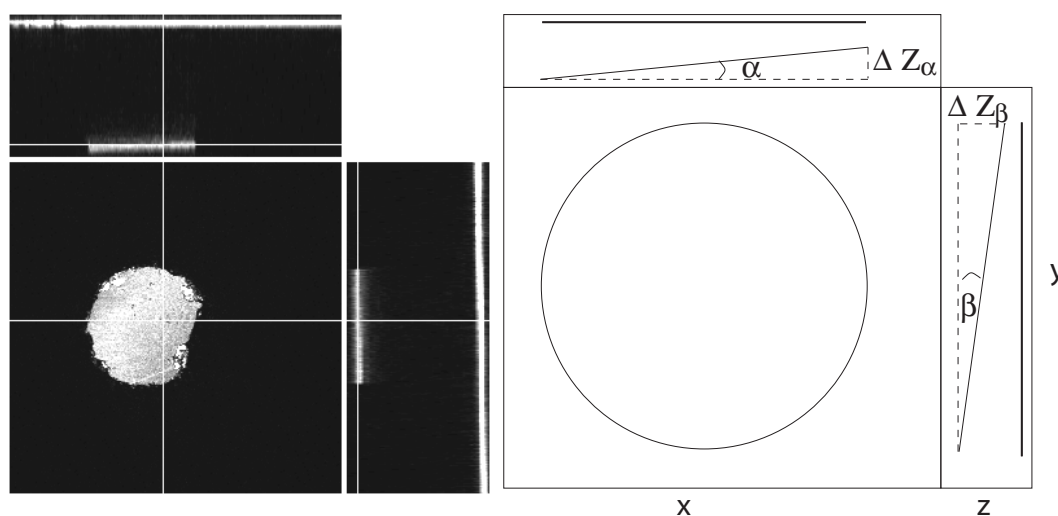


Figure 2.3: Orthogonal projection of the glass indenter and the cover glass (left) obtained using the confocal microscope in reflection mode. Angles α and β (right) can be calculated from this projection. At the start of every compression experiment, these angles were reduced to zero using the tilting table of the loading device.

mainly caused by the board and not by the sensors.

The design of the force transducer is based on two variable displacement capacitors one of which is attached to the force sensing output tube of the transducer. The other one is used to compensate for thermal fluctuations and mechanical vibrations. The capacitor plates are formed by vacuum metallisation on the surface of cantilevered fused silica beams. When a force is applied, the beam bends and the value of the capacitor changes. As the loading device is designed to be used for extended periods, the characteristics of both force transducers were monitored over 124 hours. During this procedure both transducers were located on an anti-vibration table with no applied load. The result in figure 2.5 indicates that there is a poor correlation between the room temperature and the output of the two force transducers.

To investigate whether gain or offset of the transducers changed during a 24 hour period, the glass indenter was inserted and the force, resulting from the weight of the indenter, was recorded every hour. At the start of every measurement, the amplifier output signal was set to zero by changing its offset. The mean force appeared to be $50 \pm 0.05 \mu\text{N}$, suggesting that the previous described fluctuations (figure 2.5) are a consequence of an offset change rather than a gain change. Noise levels of the transducer are about 10 nN, which corresponds with the manufacturer's specifications.

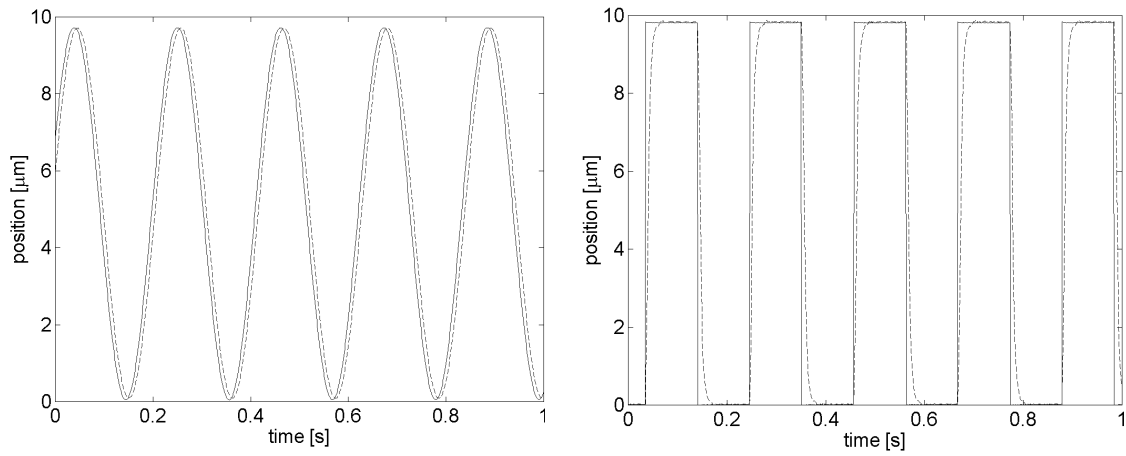


Figure 2.4: Response of the nanopositioning system on a sine (left) and square wave (right), generated with a pulse generator. Both figures show the input signal for the piezo amplifier generated by the pulse generator (solid) and the output signal of the servo controller (dashed) indicating the true position of the nanopositioning system.

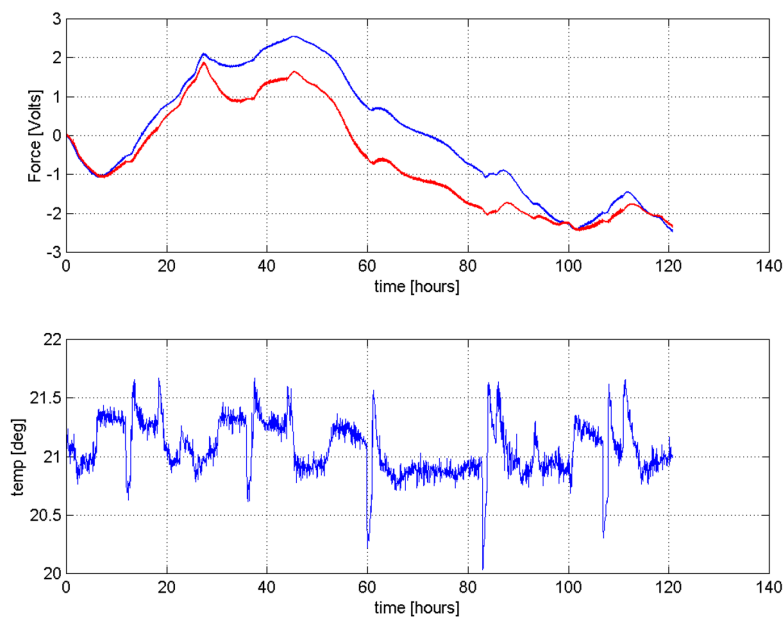


Figure 2.5: Force (top) and temperature (bottom) measured during a period of 120 hours. No loads were applied to both force transducers, which were located on an anti-vibration table. 1 Volt equals $5 \mu\text{N}$.

2.3.2 Deformation experiment

An example of a compression experiment conducted using the loading device is shown in figure 2.6. An individual myoblast was compressed until it burst. From the orthogonal projections of the confocal images, there is clear evidence of bulges at the membrane. The width of the cell is measured using the FWHM threshold (figure 2.7). From this figure, it appears that changes in the cell width mainly occur during the final compression stage, corresponding to steps C-E. The three-dimensional rendered images (figure 2.8) show the shape changes that the cell undergoes as a result of compression. Volume and surface area of the cell are calculated for three steps and presented in table 2.2. The volume of the cell remains fairly constant, whereas its surface area increases. The latter is probably the result of a stretched cell membrane.

Table 2.2: Volume and Surface Area values of a cell, calculated from the confocal images.

Axial displacement indenter (μm)	Volume (μm^3)	Surface Area (μm^2)
0	1050	900
6	1100	1000
10	1100	1300

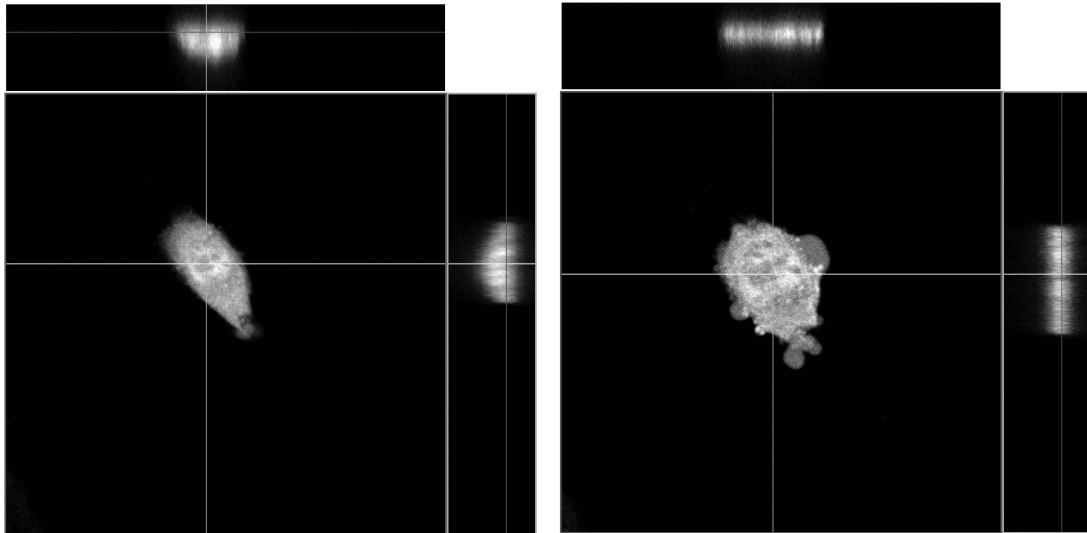


Figure 2.6: Orthogonal projections of a myoblast after 0 and 10 μm axial displacement of the glass indenter.

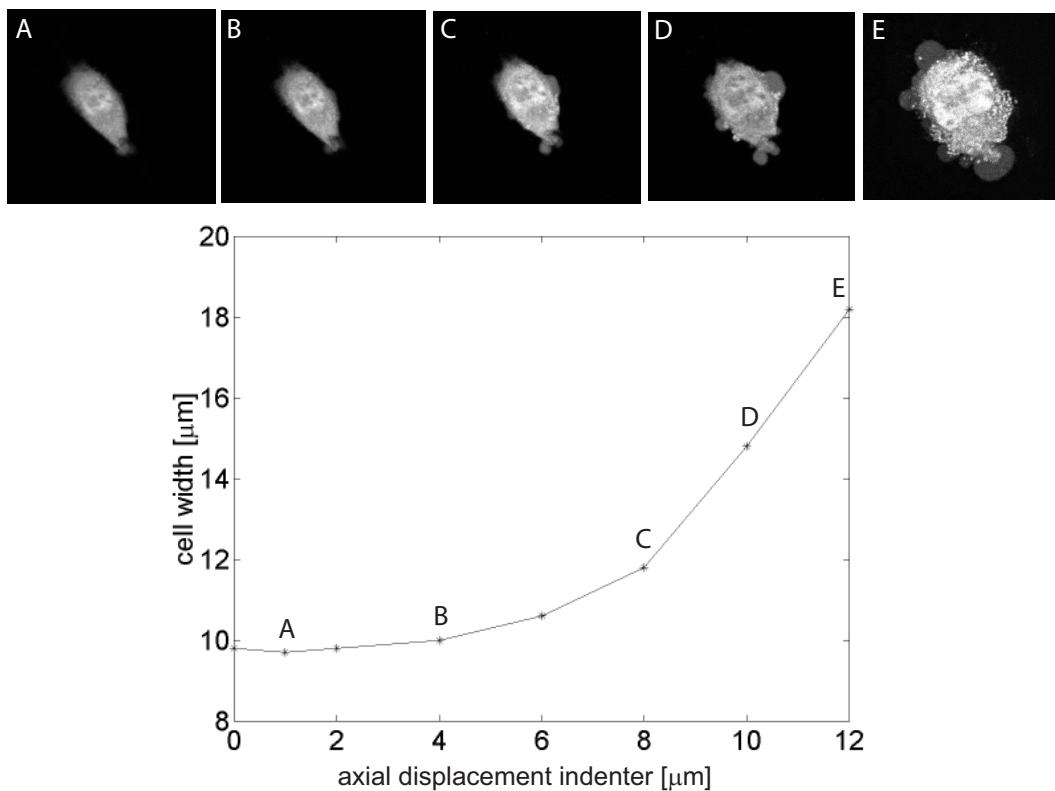


Figure 2.7: Cell width as a function of axial displacement of the glass indenter. The cell border is defined using a FWHM threshold. Horizontal confocal sections show the centre of the cell at 1, 4, 8, 10 and 12 μm axial displacement of the glass indenter.

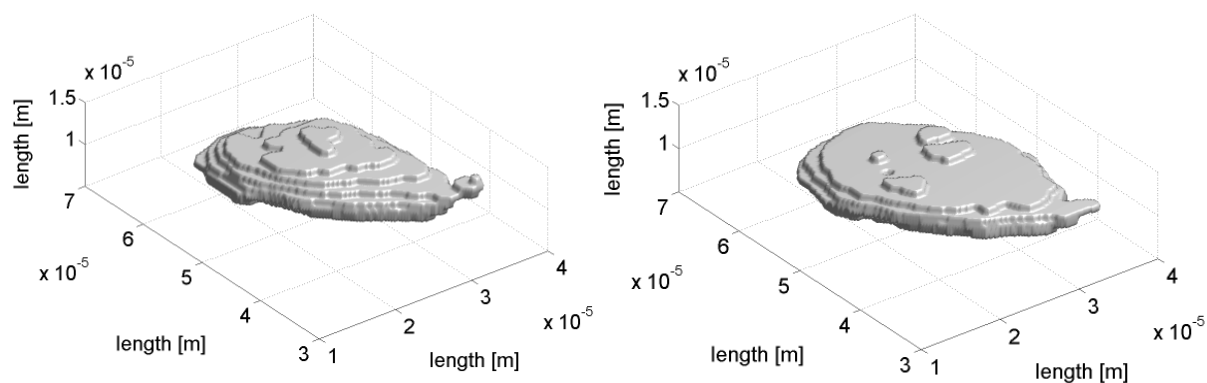


Figure 2.8: Three-dimensional rendered images of a myoblast after 0 and 10 μm axial displacement of the glass indenter.

2.4 Discussion

The single cell loading device presented in this paper can be used to monitor the biomechanical response of skeletal muscle cells under compression. This response can be reflected by changes in the morphology and mechanical properties of the cell. The morphology of the cell during compression was monitored using confocal laser scanning microscopy and analysed using custom image analysis software. Other micromanipulation techniques provided side views of the cell using conventional transmitted light microscopy (Zhang et al., 1991; Thoumine and Ott, 1999). Therefore, geometric assumptions such as axisymmetry are necessary to calculate three-dimensional quantities, such as volume and surface area. However, spread myoblasts and many other cells do not have an axisymmetric shape. Confocal microscopy provides three-dimensional images of the cell, and thus no assumptions regarding the geometry of the cell have to be made.

The micromanipulators allowed displacement of the indenter over a wider range. Therefore, multiple cells can be deformed on the same cover glass, avoiding fluctuations due to varying experimental procedures. The combination of a sensitive force transducer and a nanopositioning system creates the opportunity to perform sensitive mechanical experiments. In contrast to micromanipulators, piezo-actuators do not experience backlash, which makes them suitable for use in dynamic experiments. Evaluation of the nanopositioning system showed good dynamic characteristics. The three strain-gage position sensors and the position servo controller compensate for hysteresis and drift of the piezo-actuators in the nanopositioning system.

Evaluation of the force transducer revealed temporal instability in a similar manner to that reported by Bluhm et al. (1995). It appeared that there was a poor correlation between the room temperature and the output of the two force transducers. Probably other effects, such as humidity and air pressure, cause this variation. Specifications regarding this drift were not provided by the manufacturer of the transducer. Zhang et al. (1991) showed that several micronewtons are needed to compress animal cells and therefore the magnitude of the measured drift can be considered to be relatively large (up to 15 μN). Despite these apparent shortcomings, repeated weight measurements of the glass indenter indicated that it was the offset, which changed in time as opposed to the gain of the transducer. If cells are mechanically characterised during long-term compression experiments, the force transducer will be set to zero and a tare load will be superimposed on the already existing load. Although absolute values of reaction forces cannot be measured, changes in the mechanical properties during long-term compression can be revealed.

The position of the indenter and the resulting forces during cell compression are recorded electronically. This technique contrasts with other studies, involving micropipette aspiration and microplates (Dong et al., 1988; Thoumine and Ott, 1999), employing video images, which can lower the temporal and spatial resolution of the method. Taken together, the use of the force transducer, the nanopositioning system and the electronic data recording allow us to perform dynamic compression tests on cells.

An added advantage of the loading device is the arrangement made to create optimal culture conditions during compression. To our knowledge, the device presented here is the first one to provide environmental conditions similar to a CO₂ incubator during compression. Similar micromanipulation techniques in other studies only heated the culture medium because no long-term experiments have been conducted (Petersen et al., 1982; Zhang et al., 1991; Thoumine and Ott, 1999). The optimised culture conditions of this experimental setup make it possible to monitor morphological and mechanical changes of the cell over time.

Our initial results showed global compression of an individual myoblast. The custom image analysis software provided values of several cell geometric quantities, such as width, surface area and volume. The ability to insert any indenter in the loading device with diameters up to 500 μm , which equals the diameter of the output tube of the force transducer, makes the loading device suitable for global compression of almost every cell type and even groups of cells. Other micromanipulation techniques were designed for smaller cell types (Zhang et al., 1991; Thoumine and Ott, 1999) or local compression of cells (Petersen et al., 1982; Yoshikawa et al., 1999). Furthermore, the device can be used to support other studies, which examine the mechanics of cell spreading and cell attachment (Ra et al., 1999; Thoumine and Ott, 1999). The latter can be achieved if the glass indenter or cover glass is coated with special attachment regulating molecules, and stretching tests are performed with the device. Another advantage of the present design is the use of normal cover glasses, allowing mechanical characterisation of cells cultured on glass, which is chemically treated or micropatterned (Folch and Toner, 2000). Due to the rapid development of Green Fluorescent Protein (GFP) transfected cell lines (Cubitt et al., 1995), other applications become a possibility. These include the real time monitoring of remodelling cytoskeleton or the upregulation of other proteins due to mechanical loading. On the other hand, several protein disrupting agents can be used to remove cytoskeletal filaments and the resulting mechanical effects could be studied with the loading device (Guilak, 1995; Galbraith et al., 1998).

Future studies using the device are directed towards the viscoelastic properties of skeletal muscle cells and the deformation behaviour during compression. Furthermore, viability studies have to reveal how the magnitude and duration of deformation affect compression-induced damage or adaptation, thereby establishing thresholds for cell damage (Breuls et al., 2003b).

In summary, the device provides a useful way to monitor the biomechanical response of skeletal muscle cells under compression. The system complements other cell loading systems, due to the use of environmental conditioning for long-term experiments, piezo-actuators for dynamic mechanical characterisation, and confocal imaging for observation of three-dimensional deformation. It will therefore contribute to the knowledge concerning strain-induced cell damage as seen in pressure ulcers and other mechanically induced clinical conditions.

Chapter 3

Anisotropic, three-dimensional deformation of single attached cells under compression

3.1 Introduction

Many cells in mammalian organisms are permanently exposed to deformation. Cells are deformed by mechanical forces exerted by the external environment of the cell or generated by the internal cellular environment; a process that involves the conversion of chemical energy into mechanical energy.

The degree of cell deformation largely depends on the integrated internal structure of the cell and the connection of the cell to the external environment (Ingber, 1993; Maniotis et al., 1997). The internal structure, including the cell nucleus, cytoplasm, cytoskeleton, membranes, and organelles, provides resistance to deformation. Alterations of one of those structures can lead to an increased or decreased resistance to deformation. Disruption of one of the cytoskeletal filaments, like actin, reduces this resistance (Petersen et al., 1982), while an increase in density of the same filament causes an increase in this resistance (Sato et al., 2000). Likewise, cell-cell and cell-matrix interactions also affect cell deformability (Wang and Ingber, 1994). For example, spreading of specific cell types causes an increased mechanical resistance to deformation, presumably due to structural reorganisation of the cytoskeleton during this process (Coughlin and Stamenović, 1998; Thoumine and Carodoso, 1999).

Deformation of cells is believed to influence their biochemistry, function, and structure (Watson, 1991). Illustrative examples are deformation induced alterations in calcium signalling (Banes et al., 1994; Guilak et al., 1994), gene expression (Komuro et al., 1991; Banes, 1993), and cytoskeletal organisation (Karlon et al., 1999).

Excessive deformation, either in terms of magnitude or duration, may even lead to irreversible damage of cells such as seen in pressure ulcers (Bouten et al., 2001, 2003b), during freezing of cells (Takamatsu and Kumagae, 2002), and in bioreactors (Zhang et al., 1991).

To study the effects of cell deformation, several experimental techniques are available, applying deformations to either specific parts of the cell (local deformation) or to the cell as a whole (global deformation). Local deformation experiments include partial micropipette aspiration (Sato et al., 1990), cell poking (Daily and Elson, 1984), atomic force microscopy (Alcaraz et al., 2003), and magnetic bead cytometry (Wang et al., 1993). Global deformation experiments include the use of microplates (Thoumine et al., 1999), micromanipulation (Zhang et al., 1991), and complete micropipette aspiration (Needham and Hochmuth, 1990).

The majority of these studies assume the shape of the cell to be spherical, axisymmetric or just consider a two-dimensional cross-section of the cell. Consequently, cell deformation is assumed to be isotropic and quantified from alterations in cell volume, surface area or shape factors, such as the ratio of cell diameters (Guilak et al., 1995; Knight et al., 1996). Although these assumptions are valid for non-adherent cells, they are not appropriate for attached cells that are dependent on anchorage for normal functioning (Bhadriraju and Hansen, 2002). For example, many cell types that are allowed to spread, undergo growth and differentiation, whereas if they were constrained in a spherical form in culture, they would undergo either apoptosis or dedifferentiation

(Mooney et al., 1992; Chen et al., 1997). In vivo and in vitro most cells are spread, attaching to either the extracellular matrix or the culture substrate. Therefore, it is physiologically relevant to study the deformation of attached cells. Because these cells show a more irregular shape than cells in suspension, it is desirable to obtain three-dimensional images of the cell during deformation experiments.

Confocal laser scanning microscopy provides a way to obtain three-dimensional images of living cells by making optical sections through the depth of the cell (Wilson, 1989; Errington et al., 1997). This technique has been successfully applied to study the deformation of chondrocytes and nuclei in articular cartilage explants (Guilak, 1995). However, the deformation of attached cells has never been investigated in three dimensions.

The present study aimed at quantifying the three-dimensional deformation of single cells in an attached configuration. Single cells attached to a culture substrate, were deformed using a specially designed loading device for unconfined compression under optimal environmental conditions, comparable to those of a regular CO₂ incubator. The width, height, cross-sectional area, surface area, and volume of the cell during compression were estimated by means of combining confocal laser scanning microscopy with custom developed processing software. To quantify cell shape, a shape factor was introduced, which describes the ratio of the two major principal axes of the attached cell.

3.2 Materials and methods

3.2.1 Cell culture

The cells investigated in this study are C2C12 mouse skeletal myoblasts (ECACC, Porton Down, UK). Cells were cultured in growth medium consisting of Dulbecco's modified Eagle medium supplemented with 15 % fetal calf serum, 1 % nonessential amino acid solution, 20 mM HEPES and 0.5 % gentamicine (all from Biochrom AG, Berlin, Germany). Cells were used at passages 10 to 14.

3.2.2 Loading device

The device for unconfined compression of single attached cells is shown in figure 3.1 and described in detail elsewhere (Peeters et al., 2003). To review briefly, it consists of a stainless steel frame resting on a motorised stage of an inverted microscope (Axiovert 100M, Zeiss, Göttingen, Germany) with a confocal laser scanning unit (LSM 510, Zeiss, Göttingen, Germany). Cells are grown on cover glasses, which can be inserted in the cell chamber (3 mm deep and 25 mm in diameter) of the stainless steel frame. The cell chamber provides environmental conditions with control of temperature (37 °C) and CO₂ (5 %).

Cells can be compressed with a glass indenter (0.48 mm in diameter) having a flat surface with a diameter of 60 μm (figure 3.1, insert). The indenter was inserted

in the hollow output tube of a force transducer (model 406A, Aurora Scientific Inc., Ontario, Canada), which has a full scale range of $500 \mu\text{N}$ and a resolution of 10 nN . Forces imposed on the cell were measured and sampled, after a 10 fold amplification, by a data-acquisition board (PCI-6052E, National Instruments, Austin, TX). The force transducer was attached to a tilting table, allowing to twist the force transducer around two axes in the horizontal plane at a maximum of 2 degrees. This ensures that the surface of the glass indenter is parallel with respect to the cover glass. The indenter can be moved using three wide range (15 mm), low accuracy (100 nm) micromanipulators (M-111.DG, Physik Instrumente, Karlsruhe, Germany) and a small range ($100 \mu\text{m}$), high accuracy (5 nm) nanopositioning system with three piezo-actuators (Nanocube P-611, Physik Instrumente, Karlsruhe, Germany). The position of the micromanipulators and the piezo-actuators were controlled and recorded using a motor controller PC board (C-842, Physik Instrumente, Karlsruhe, Germany) and the data-acquisition board in a personal computer. Calibration of the piezo-actuators was carefully performed by the manufacturer and resulted in a displacement sensor sensitivity of $10 \mu\text{m}/\text{V}$. Calibration of the force transducer was carried out by applying known weights to the hollow output tube of the transducer, resulting in a sensitivity of $5 \mu\text{N}/\text{V}$. Compliance of the transducer was determined by compressing the indenter on a hard surface while simultaneously recording the position of the piezo-actuator and the force. This resulted in a compliance of $15 \mu\text{m}/\text{mN}$.

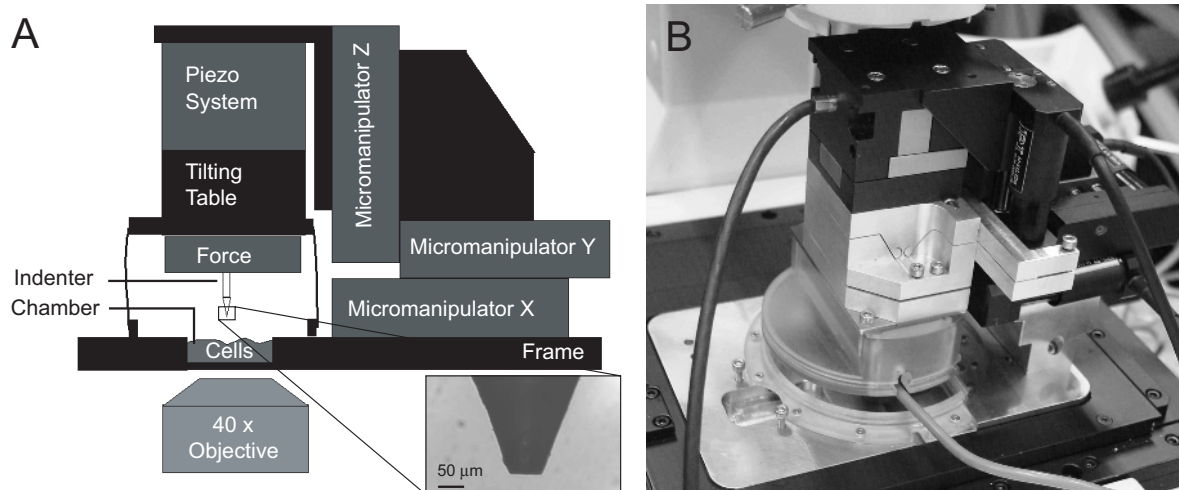


Figure 3.1: Schematic representation (A) and actual realisation (B) of the single cell loading device. The insert shows a close-up of the glass indenter.

3.2.3 Experimental procedure

Cells were seeded at subconfluent densities ($20,000 \text{ cells/cm}^2$) on the cover glass within the stainless steel frame of the loading device. Cells were allowed to attach for at least 16 hours and then stained with $7.5 \mu\text{M}$ Cell Tracker Green (CTG, Molecular Probes, Leiden, the Netherlands), which stains the cytoplasm of the cells. The frame was then placed onto the motorised stage of the confocal microscope. After attachment of the other components of the loading device, the indenter was lowered into the growth medium using the micromanipulators. Using the confocal microscope in reflection mode, the glass indenter was moved to a position of $20 \mu\text{m}$ above the cover glass. Then, a cell was selected for compression and a complete stack of confocal images of the undeformed cell was recorded. The height of the cell was estimated using the imaging software of the microscope and the indenter was subsequently moved to the top of the cell. During the compression experiment, the indenter was lowered by $0.5 \mu\text{m}$ increments of axial displacement, followed by the recording of a stack of confocal images to visualise the complete deformed cell (figure 3.2). The position of the piezo-actuators and the force were recorded continuously. The experiment was ended, when the output of the force transducer reached its maximal value of $50 \mu\text{N}$. In total, 14 cells were subjected to the compression test protocols.

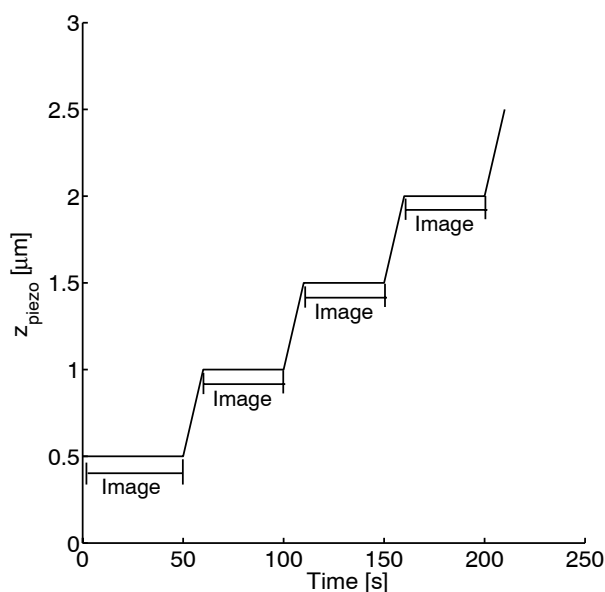


Figure 3.2: Schematic of the loading protocol in which individual cells were compressed using compression increments of $0.5 \mu\text{N}$. A complete stack of confocal images of the cell was recorded between two compression increments.

For confocal imaging, the cell was visualised using a 40x, air, 0.95 numerical aperture objective (Plan- Apochromat, Zeiss, Göttingen, Germany). To excite the CTG stain, the

Argon ion laser excitation was set at 1 % of a tube current of 6 A at 488 nm, with emission recorded above 515 nm. To compensate for geometric distortion due to a mismatch in refractive index of the immersion medium (growth medium) and the objective medium (air), a linear z-correction factor of 1.33 was introduced (Visser et al., 1992; Hell et al., 1993; Bucher et al., 2000). Images were recorded with a pixel size of $0.22 \times 0.22 \mu\text{m}^2$ and a slice thickness of $0.4 \mu\text{m}$. For each separate cell the gain of the photomultiplier was chosen in such a way that the maximum value of the eight-bit digitised signal was kept just below a grey level value of 250 to avoid electronic saturation of the photomultipliers and to ensure a maximum signal to noise ratio. After the experiment, the confocal images were deconvolved using the Huygens System image restoration software (Scientific Volume Imaging BV, Hilversum, the Netherlands). A theoretical point spread function was calculated using electromagnetic diffraction theory, while deconvolution was carried out by a maximum likelihood based algorithm (Kempen et al., 1997).

3.2.4 Data analysis

Each stack of confocal images was analysed with the aid of a custom software program in Matlab (The Mathworks, Natick, MA, USA). All images were smoothed by a 2-D median filter. To define the cell boundary, the images were thresholded using a full width half maximum threshold as adopted in previous studies (Knight et al., 1996; Lee et al., 2000; Bouten et al., 2001). The binary images were then morphologically opened and any cavities were filled using the majority and fill algorithm in Matlab. A volume set was created by storing all binary images of each stack into a three-dimensional matrix. To avoid steps in three-dimensional reconstructions as a result of the higher axial sampling distance compared to the lateral sampling distance, a box filter with a size of $3 \times 3 \times 3$ was applied to the volume data set. The cell volume (V) was calculated by summing up all relevant voxels and multiplying them by the voxel size. Relevant voxels are defined as those with a value of 1 and thus are considered to be part of the cell. A three-dimensional reconstruction of the cell was created using the iso-surface method as implemented in Matlab. This routine forms a triangulation of the volume set and represents the object as a series of linked triangles. The surface area of the cell (SA) was then calculated by summing the areas of all triangles. The height of the cell (H) was calculated as an average of the height in a user defined area at the top of the cell. For each point in this area, all voxels in the axial plane were summed and multiplied with the axial sampling distance. Assuming the density of the cell to be constant, the centre of mass of the cell was determined by averaging the x, y, and z coordinates of all relevant voxels. The mass moments of inertia matrix of the cell (I_m) at each compression step were determined with respect to a translated cartesian coordinate system with its origin located in the centre of mass of the cell:

$$I_m = \begin{pmatrix} I_{xx} & I_{xy} & I_{xz} \\ I_{yx} & I_{yy} & I_{yz} \\ I_{zx} & I_{zy} & I_{zz} \end{pmatrix} = \begin{pmatrix} \sum_i m_i (y_i^2 + z_i^2) & \sum_i m_i x_i y_i & \sum_i m_i x_i z_i \\ \sum_i m_i x_i y_i & \sum_i m_i (x_i^2 + z_i^2) & \sum_i m_i y_i z_i \\ \sum_i m_i x_i z_i & \sum_i m_i y_i z_i & \sum_i m_i (x_i^2 + y_i^2) \end{pmatrix}, \quad (3.1)$$

where x_i , y_i , and z_i are the coordinates of the voxels according to the translated coordinate system and m_i is the mass of an individual voxel. The value of m_i was considered to be constant and equals the volume multiplied by the density of the voxel. Solving an eigenvalue problem, the orientation of the three principal axes of inertia was determined. These axes represent the three axes of an ellipsoid, which best matches the shape of the cell. The magnitude of each axis of the ellipse is given by:

$$I_i = \frac{1}{\sqrt{\lambda_i}}, \quad (3.2)$$

in which λ_i is the eigenvalue of the eigenvector representing the corresponding principal axis. Now, a shape factor κ_{21} is defined as being the ratio between the magnitudes of the two major principal axes:

$$\kappa_{21} = \frac{I_2}{I_1}. \quad (3.3)$$

This shape factor is a unitless ratio that equals unity for a circle and diverges from unity for any other shape. It provides a measure of the efficiency with which a perimeter encloses an area, and thus indicates the degree of deviation of a shape from circular (figure 3.3).

The width (W) of the cell was determined along the second principal axis of the cell. The cross-sectional area (A) of a slice through the centre of mass of the cell was calculated by summing all relevant pixels and then multiplying this value by the pixel area. All geometric parameters obtained for each cell are summarised in figure 3.4.

To assess the accuracy of the method, the analysis was performed on two mathematically defined shapes and on images obtained from measurements on fluorescent beads with known diameter. The measured geometric parameters appeared to deviate less than 7 % from their theoretically determined values (Appendix A).

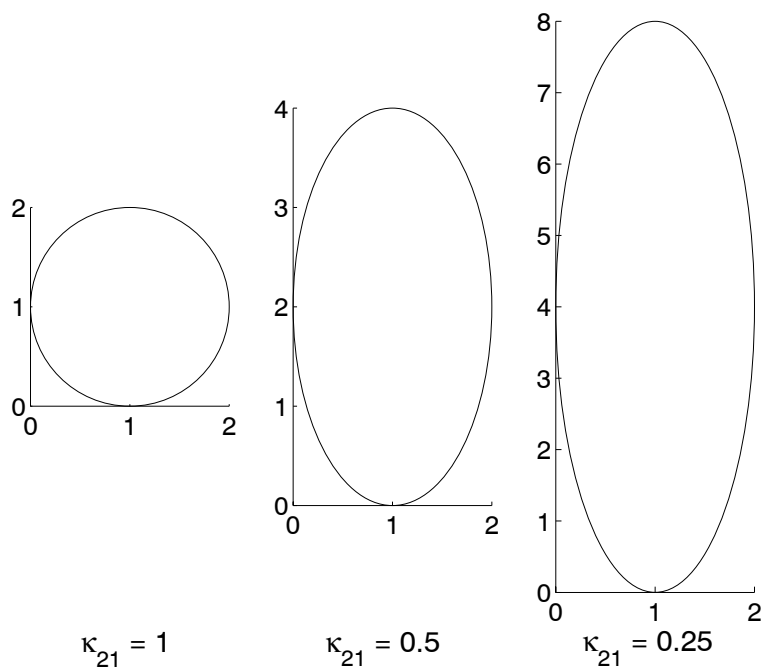


Figure 3.3: Shape factor κ_{21} describes the ratio between the magnitude of the first and the second principal axis. The values for κ_{21} are shown for three basic shapes.

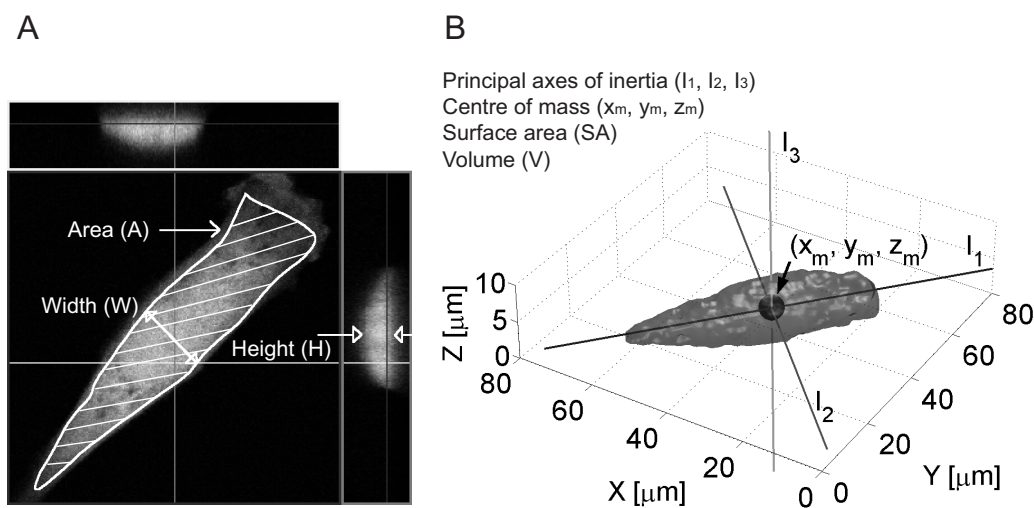


Figure 3.4: Overview of the geometric parameters obtained for each cell. An orthogonal projection of the cell (A) as well as a three-dimensional reconstruction (B) of the same cell are shown.

3.3 Results

Orthogonal projections of a cell as recorded with confocal microscopy at six compression increments are shown in figure 3.5. From these typical images, flattening of the cell due to compression can be observed. The final image (figure 3.5 F) shows the cell when the cell membrane has been totally ruptured and a thin layer of cell debris was left over. From these images two major phenomena can be observed. First, it can be seen that the cell deforms more in the direction of the second principal axis (I_2) than the first principal axis (I_1). This phenomenon was observed in all compression experiments.

In addition, the nucleus of the cell also deforms more in the direction of the second principal axis than of the first principal axis. In figure 3.5 A the nucleus has an elliptical shape, whereas in figure 3.5 E the nucleus adopts a more circular shape. This phenomenon was observed in all compression experiments when the nucleus was visible. The nucleus was visible in 70 % of the experiments.

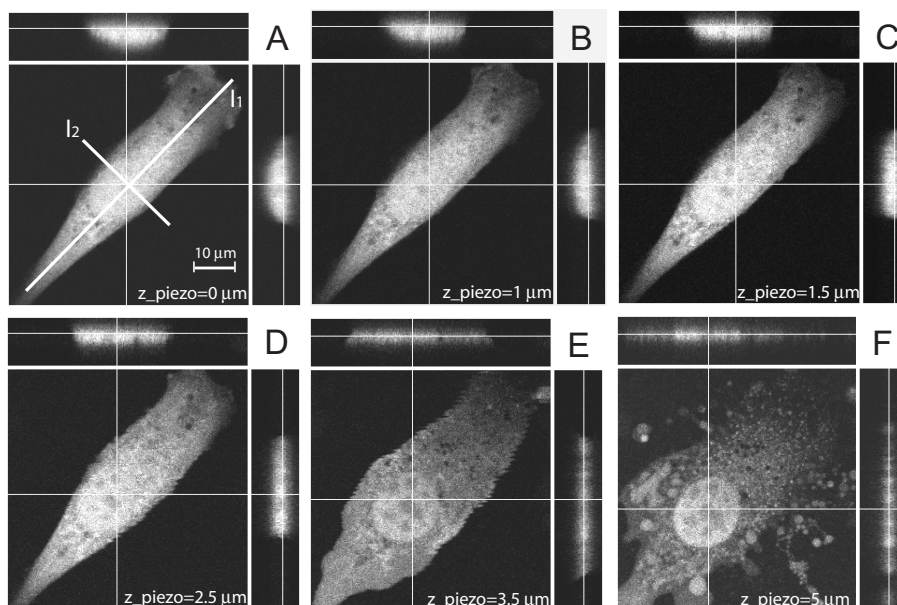


Figure 3.5: Orthogonal projections of a cell at 6 different compression increments obtained by confocal microscopy. Panel A shows the two major principal axes of the cell: I_1 and I_2 . Panel F shows the cell when the maximum measurable force of the transducer was reached and only a thin layer of cell debris was left over. The ruptured membrane can be clearly seen.

Deconvolution was applied to all confocal images. The effect of deconvolution is especially significant in the axial plane (XZ and YZ plane) of the images, which is shown in figure 3.6.

The initial values of the measured geometric parameters of all 14 cells in the undeformed situation are given in table 3.1. In order to summarise the compression data,

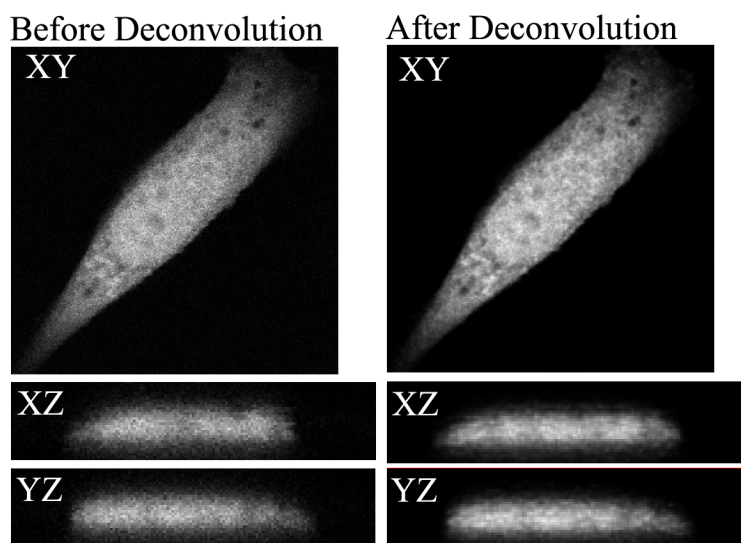


Figure 3.6: XY, XZ, and YZ plane of a stack of confocal images, before and after deconvolution.

the changes as a percentage of the initial values for all geometric parameters and the shape factor were averaged for all cells and plotted against axial compression intervals of 10 %. Only the data up to 50 % axial deformation were taken into account, for at larger axial deformations the cells showed structural damage. The results of original and deconvolved images of compression experiments performed on the 14 cells are shown in figures 3.7 and 3.8. At each compression interval of 10 %, statistical difference from zero deformation for all geometric parameters and the shape factor was tested using a Student's *t*-test with a 0.05 level of significance. Cell width, area, and surface area all increased as a result of compression. There was also a slight increase in volume observed, although the volume increase was only statistically different from zero for the original images at the axial deformation of 45 % (figure 3.7 D). After deconvolution, however, the volume increase was not statistically different from zero. The shape factor κ_{21} increased as a result of compression, implying that the cells deformed anisotropically from an elliptical to a more circular shape. The percentage change of κ_{21} was statistically significant from zero for each 10 % increase in deformation up to 45 % (figure 3.8 B).

Table 3.1: Initial values of width, height, area, surface area, and volume of 14 cells before a compression experiment (mean \pm SD).

Width (μm)	Height (μm)	Area (μm^2)	Surface Area (μm^2)	Volume (μm^3)
15.7 ± 2.0	6.7 ± 1.1	511 ± 140	1470 ± 380	2505 ± 710

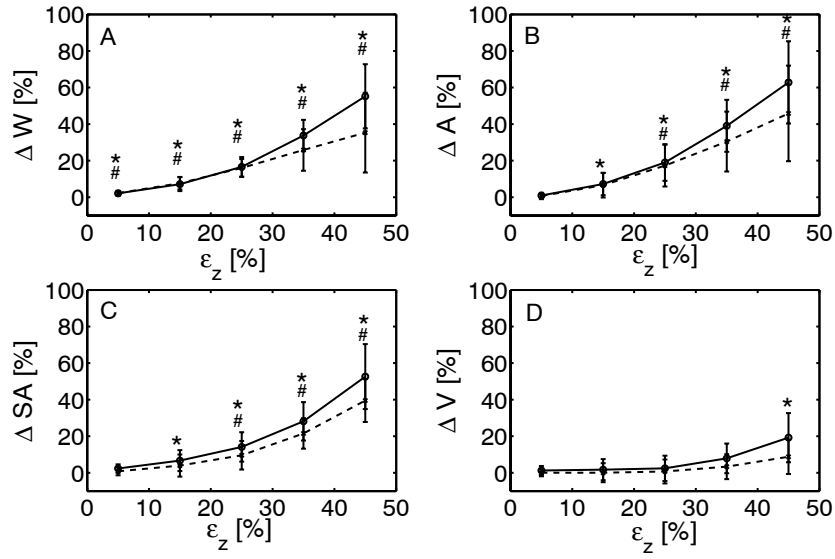


Figure 3.7: Average percentage changes of cell width (A), area (B), surface area (C), and volume (D) as a function of the axial deformation for 14 cells (mean \pm SD) before (solid) and after (dashed) deconvolution. *: Parameter differs significantly from zero, before deconvolution ($p < 0.05$). #: Parameter differs significantly from zero, after deconvolution ($p < 0.05$).

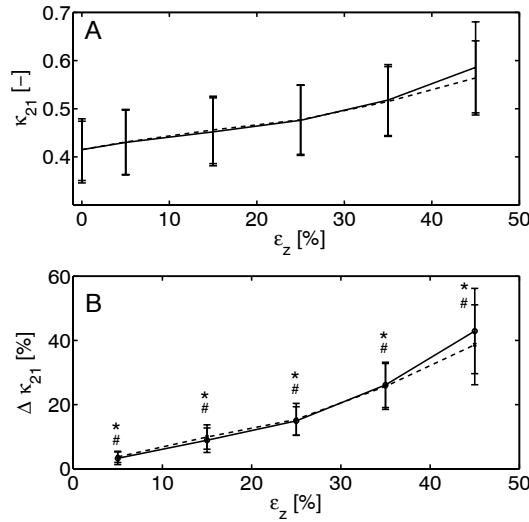


Figure 3.8: Average value (A) and percentage change of shape factor κ_{21} (B) as a function of the axial deformation for 14 cells (mean \pm SD) before (solid) and after (dashed) deconvolution. *: Parameter differs significantly from zero, before deconvolution ($p < 0.05$). #: Parameter differs significantly from zero, after deconvolution ($p < 0.05$).

3.4 Discussion

This study for the first time examined and quantified the three-dimensional deformation of attached cells under compression. Deformation was described using the width, area, surface area, and volume of the cell. In order to quantify cell shape and possible anisotropic deformations, a shape factor was calculated, describing the ratio between the two major principal axes of the cell.

The use of confocal imaging and associated software allowed the three-dimensional quantification of cell deformation. Such a procedure obviated the need to make assumptions regarding the geometry of the cell.

Cells were allowed to attach and spread for at least 16 hours. In contrast, other studies examining cell deformation using confocal microscopy investigated non-attached C2C12 myoblasts and chondrocytes, which have a more or less spherical morphology (Lee et al., 2000; Bouten et al., 2001). The large diameter of the indenter permitted the compression of the entire cell and not a part of the cell as in the case with other indentation techniques, such as atomic force microscopy (Vesenka et al., 1995; You et al., 2000) or cell poking (McConnaughey and Petersen, 1980; Petersen et al., 1982). Micropipette aspiration experiments also allow the deformation of the entire cell but are often only applied to suspended cells (Evans and Yeung, 1989; Needham and Hochmuth, 1990). Cells can be deformed entirely using microplate manipulation (Thoumine et al., 1999), but this technique allows the cell to attach for a maximum of 4 hours, which is insufficient for C2C12 myoblasts to fully spread. Indeed, extended incubation times for cell attachment caused migration of the cell towards the edge of the microplate (Gaille et al., 2002).

Cell width, area, and surface area increased during compression (figure 3.7). The increase of surface area is an apparent increase in the overall surface area, as the folds and ruffles in the cell membrane cannot be observed with confocal microscopy (Lee et al., 2000). Furthermore, it should be noted that local membrane strains can be much larger than the overall measured membrane strain because the cells were able to deform mainly between the glass indenter and the cover glass.

At 45 % strain, a significant increase in cell volume was observed based on the non-deconvolved images. This increase might be the result of osmotic swelling due to malfunctioning pumps within the cell membrane. More likely, the volume increase can be attributed to the limited axial resolution of the confocal microscope (Sheppard, 1989; Visser et al., 1992). The axial resolution is proportional to the square of the numerical aperture, and is approximately $1.4 \mu\text{m}$ for the 40x objective with a numerical aperture of 0.95 used in this study. The lateral resolution is approximately $0.3 \mu\text{m}$. The limited axial resolution mainly affects the measurements of cell height and volume and will result in an overestimation of the two parameters, which was also observed in the measurements of the fluorescent beads (Appendix A). Of course this effect will become more pronounced at large axial deformations. The use of deconvolution compensates to a certain extent for this limited axial resolution (Kano et al., 1996; Kempen et al., 1997), thereby reducing the overestimated height and volume of the cell. This can be observed

in figure 3.7 in which the difference between the deconvolved and non-deconvolved data increased with axial deformation. Moreover, the volume increase based on the deconvolved images was never significantly different from zero.

The shape factor used in this study describes the shape of an ellipse, which best matches the shape of the cell. Although the use of the shape factor is comparable to the deformation index used in other studies (Guilak, 1995; Knight et al., 1996; Bouten et al., 2001) and to the shape factor used to describe cell reshaping in epithelia (Brodland and Veldhuis, 2002), it has considerable advantages over those previously reported. First, the derivation of the shape factor through calculation of the principal axes of inertia is a relatively straightforward automatic method and thus free of operator error. A deformation index will be difficult to define for attached cells with their irregular shapes. Secondly, the shape factor describes the overall shape of the cell, which makes this method suitable to describe shape changes on a global cell level and to compare the deformation behaviour of several cells (Brodland and Veldhuis, 2002). In addition, the shape factor is based on the two major principal axes of the cell and independent of the orientation of the cell on the cover glass.

The shape factor κ_{21} increased with axial compression, which was caused by a relative increase of I_2 (along the second principal axis) compared to I_1 (along the first principal axis). This can also be seen in figure 3.5, showing that the cell deforms more in the direction of the second principal axis than the first principal axis. Thus, the cell deforms in an anisotropic way.

This anisotropic deformation may be attributed to actin stress fibres that form connections between the focal adhesion points at the substrate and the remainder of the cell body. Actin fibres largely contribute to the resistance against deformation of cells and disruption results in a decreased mechanical stiffness (Petersen et al., 1982; Sato et al., 1990). Visualisation of actin fibres in fixed C2C12 cells stained with FITC-phalloidin revealed that they are predominantly orientated along the first principal axis of the cell (figure 3.9 A). Due to the higher stiffness along the first principal axis as a result of the actin fibres, the cell deforms less in this direction (figure 3.9 B, C). If a cell does not have a preferred orientation of actin filaments, the deformation will probably be more or less isotropic. All cells examined in this study have a more or less elliptical shape and thus an orientated actin cytoskeleton. Notwithstanding these considerations, the importance of the actin cytoskeleton in determining anisotropic behaviour could be further examined by compressing cells with and without actin stress fibres. At the same time, actin should be visualised during deformation of live cells using for example GFP-labelled (green fluorescent protein) actin.

It appears that this structural restriction to deformation is also applicable for the cell nucleus. Results suggest that the nucleus deformed more in the direction of the second principal axis than the first principal axis. This anisotropic deformation can be explained when considering a direct connection of the cytoskeleton to the nucleus (figure 3.9 B, C). Without this connection, the nucleus would deform isotropically as can be concluded from the nuclear structure, which shows no preferred fibre orientation (Stuurman et al., 1998). Deformation of the nucleus during cell deformation has

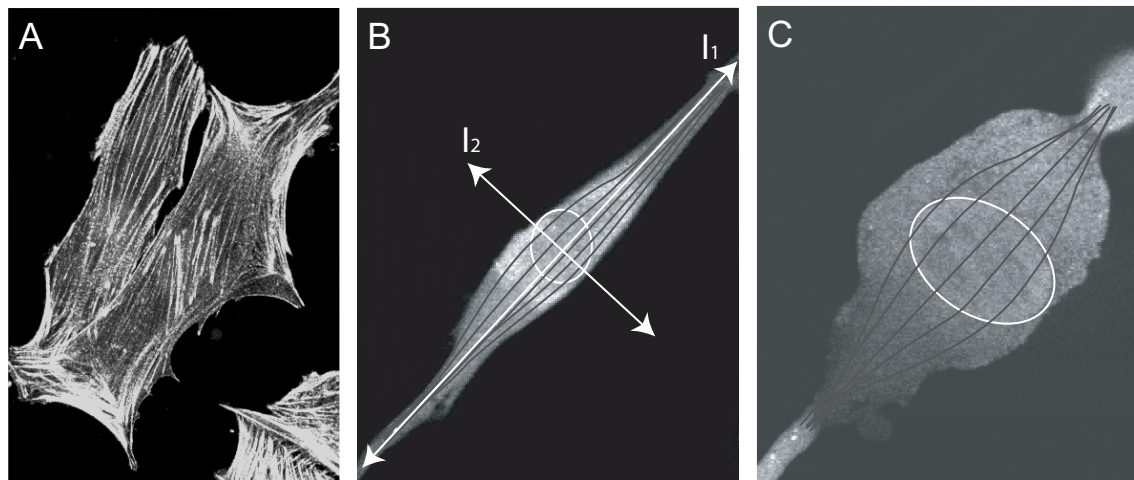


Figure 3.9: A: Actin fibres in two C2C12 cells.

B,C: C2C12 cell with a schematic representation of the actin cytoskeleton, which is predominantly orientated along the first principal axis of the cell. As a result of the actin fibres, deformation of the cell and its nucleus is restricted in this direction.

also been reported in chondrocytes in articular cartilage explants (Guilak, 1995) and tenocytes in tendons (Arnoczky et al., 2002). Guilak (1995) showed that the actin cytoskeleton plays an important role in the link between compression of the extracellular matrix and deformation of the chondrocyte nuclei. Furthermore, other studies report direct connections of the cell membrane to the nucleus via the cytoskeleton and address mechanical signalling to a cytoskeletal mediated deformation of the nucleus (Ben-Ze'ev, 1991; Wang et al., 1993; Banes et al., 1995; Janmey, 1998).

In summary, the deformation of attached myoblasts from a mouse cell line under compression was characterised both qualitatively and quantitatively using a single cell loading device in conjunction with confocal microscopy. A significant increase in surface area was found as a result of cell compression. No significant change in volume was found. It was shown that the cell and the nucleus deformed perpendicular to the direction of the actin filaments that run predominantly along the long axis of the cell. This strongly suggests that this anisotropic deformation can be attributed to the preferred orientation of actin filaments. A shape factor was used to quantify the global shape of attached cells. The increase of this factor during compression reflected the anisotropic deformation of the cell.

In future studies, the developed technique and loading device can be used to examine the relationship between cellular deformations and their biomechanical response, reflected by mechanical, structural, and functional changes. Furthermore, the methodology and results described here will be valuable to study strain induced cell damage as seen in mechanically induced clinical conditions, such as pressure ulcers or repetitive strain injuries.

3.5 Appendix A, Image analysis validation

To validate the image analysis method, the analysis was performed on mathematically defined shapes (cube and sphere) and images obtained from measurements on fluorescent beads with known diameter (FocalCheck, Molecular probes, the Netherlands) (figure 3.10). The mathematically defined cube had an edge length of 81 pixels and the sphere a diameter of 79 pixels. The fluorescent beads contain a green stain throughout and a red stain in a surface layer with a surface of less than $1 \mu\text{m}$ according to manufacturer specifications. For evaluation of the method, only the green stain of the bead was excited. To minimise refraction at the bead surface and thus prevent the relatively large bead acting as a lens, the beads were measured in immersion oil, which has almost the same refractive index as the fluorescent beads (1.52 compared to 1.56). A linear correction factor of 1.52 and a sampling density of $0.12 \times 0.12 \times 0.5 \mu\text{m}^3$ was used. The values of the geometric parameters of 10 beads and model geometric solids estimated by the above mentioned method are listed in table 3.2 and 3.3. Furthermore, the percentage deviations of the measured values with the theoretical values are listed. The deviations for the fluorescent beads were calculated for each individual bead and subsequently averaged. The geometric parameters of the mathematical shapes were estimated within 4 % deviation from the theoretical value, compared to 7 % of the beads. An overestimation of approximately 6 % of the height, volume, and surface area of the beads was observed. The estimates for the width and area of the beads were more accurate, resulting in an average percentage deviation of 2 %. Using a Student's *t*-test with a 0.05 level of significance, it appeared that the mean values of the geometric parameters of the beads were never significantly different from the theoretically determined values.

Table 3.2: Estimated (e) and theoretical (t) values of the width (W in μm), height (H in μm), and cross-sectional area (A in μm^2) of the model geometric solids and fluorescent beads (n=10) (mean \pm SD).

Object	W_e	W_t	%	H_e	H_t	%	A_e	A_t	%
Cube	81	81	0	81	81	0	6561	6561	0
Sphere	79	79	0	79	79	0	4984	5026	-0.8
Bead	13.7 ± 0.2	14	-2 ± 1	14.6 ± 0.3	14	4.2 ± 2.3	151 ± 3	154	-1.8 ± 1.8

Table 3.3: Estimated (e) and theoretical (t) values of the surface area (SA in μm^2) and volume (V in μm^3) of the model geometric solids and fluorescent beads ($n=10$) (mean \pm SD).

Object	SA_e	SA_t	%	V_e	V_t	%
Cube	38025	39366	-3.4	531441	531441	0
Sphere	19874	19607	1.4	264712	258150	2.5
Bead	656 ± 28	616	6.4 ± 4.6	1528 ± 59	1437	6.3 ± 4.1

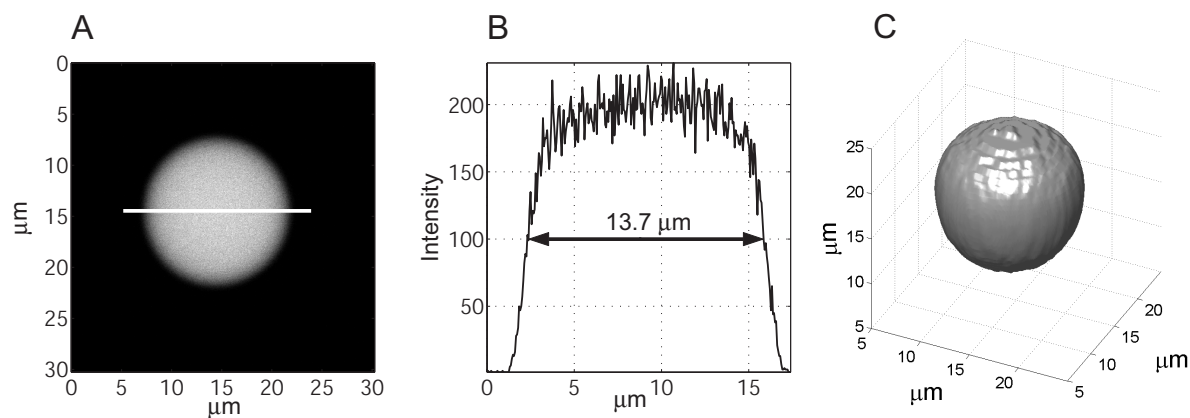


Figure 3.10: Confocal slice at the centre of a fluorescent bead (A), the image intensity profile (B) obtained across the line in panel A and a three-dimensional reconstruction of the bead from all confocal slices (C). The full width half maximum threshold resulted in a measured width of 13.7 μm .

Chapter 4

Load-bearing properties of attached cells under compression

4.1 Introduction

Under normal physiological conditions, cells are continuously subjected to mechanical forces that deform the cells and directly or indirectly influence cellular functioning. Biological effects of mechanical forces include signal transduction, gene expression, growth, differentiation, and survival (Watson, 1991; Chen and Ingber, 1999). Although the effects on certain cells are relatively well described, the underlying physiological mechanisms involved in these phenomena still remain unclear (Stoltz and Wang, 2002). These so-called mechanotransduction mechanisms are believed to involve the activation of G-proteins (Gudi et al., 1998), stretch activated ion channels (Guharay and Sachs, 1984; Sokabe et al., 1991), and direct signalling to the cell nucleus via cytoskeletal filaments (Wang et al., 1993; Maniotis et al., 1997).

Cell deformation largely depends on the mechanical properties of the cell, which are determined by its intracellular components (cytoskeleton, nucleus, cytoplasm, and several other organelles) and the interactions of the cell with its environment. In particular adherent cells rely more on the cytoskeleton and the interactions between the cell and its environment than cells in suspension (Coughlin and Stamenović, 1998; Thoumine and Carodoso, 1999). Because many cells attach to the extracellular matrix *in vivo* or a substrate *in vitro*, it is physiologically more relevant to study the mechanical properties of attached cells rather than cells in suspension.

Although necessary for cellular functioning, excessive deformation results in cell damage or death, such as seen in pressure ulcers (Bouten et al., 2001, 2003b), during freezing of cells (Takamatsu and Kumagae, 2002), and in bioreactors (Zhang et al., 1991). Measurements of the mechanical properties of cells are required to understand how mechanical forces influence cell deformation, cellular functioning, and deformation induced damage or death. In addition, these properties provide means to quantify the effects of mechanical stimuli, chemical stimuli, drugs (Petersen et al., 1982; Sato et al., 1990) and specific diseases on cells (Thoumine and Ott, 1997a; Wu et al., 2000).

The mechanical properties can be characterised by measuring the force versus strain relationship and the maximum force at breakdown of cells (Zhang et al., 1992), collectively called the load-bearing properties of cells. This requires global loading of single cells by applying large deformations while measuring the associated forces. Zhang et al. (1991) defined the maximum force at breakdown as the force at bursting of the cell during compression, and quantified it for single mammalian cells in suspension, using a novel micromanipulation technique. However, the bursting force of single attached cells remains to be elucidated. Furthermore, more insight should be provided in terms of cell structure during loading to explain the mechanisms associated with cell bursting.

The aim of the present study was to obtain the load-bearing properties of cells in their attached configuration. Therefore, the force versus axial strain relationship and the bursting force of attached cells were measured by compression experiments using a recently developed single cell loading device (Peeters et al., 2003). Experimental data were interpreted using finite element simulations, which provided an estimate of the Young's modulus of the cell. Confocal microscopy was used to visualise the cells and to

gain more insight into the bursting mechanism of cells under compression.

4.2 Materials and methods

4.2.1 Cell culture and loading device

In this study, attached C2C12 mouse myoblasts were compressed using a single cell loading device. For a description of the culture protocol and the loading device the reader is referred to sections 3.2.1 and 3.2.2.

4.2.2 Experimental procedure

Cells were seeded at subconfluent densities (20,000 cells/cm²) on the cover glass within the stainless steel frame of the loading device. Cells were allowed to attach for 24 hours and then stained with 7.5 μ M Cell Tracker Green (CTG) and 7.5 μ M Propidium Iodide (PI) (Molecular Probes, Leiden, the Netherlands), which stain the cytoplasm of living cells and the nucleus of dead cells respectively (Breuls et al., 2003a). The frame was then placed onto the motorised stage of the confocal microscope. After attachment of the other components of the loading device, the indenter was lowered into the growth medium using the micromanipulators. Using the confocal microscope in reflection mode, the glass indenter was moved to a position of 20 μ m above the cover glass. An individual cell was then selected for compression and a complete stack of confocal images of the undeformed cell was recorded, using the same settings as described in section 3.2.3. The height of the cell was estimated using the imaging software of the microscope and the indenter was subsequently moved to the cell. During the actual compression experiment, the indenter was moved with a constant velocity (figure 4.1) to compress the cell completely within 15 seconds. Force and position of the piezo-actuators were recorded continuously with a sampling frequency of 100 Hz. During the experiment, a time series of two-dimensional confocal images of the cell was made in the lateral plane with a sampling size of 0.22x0.22 μ m² and a sampling time of 1.7 s per image. Only two-dimensional images were made, because the scanning time for a complete stack of images was too large (approximately 50 seconds). The CTG stain was excited using the Argon ion laser at 1 % of a tube current of 6 A at 488 nm, with emission recorded between 515 and 560 nm. PI was excited using a Helium-Neon laser with an excitation of 2 % at 543 nm, with emission recorded above 580 nm. In total, 12 cells were subjected to the compression experiment.

At the end of the above procedure, there was a component left of the dead cell, referred to as the cell debris layer. A separate experiment was performed to measure the height of this cell debris layer (H_{debris}) for 10 cells at a force of approximately 20 μ N. In this case a 63x, 1.4 numerical aperture, oil-immersion objective (Plan-Apochromat, Zeiss, Göttingen, Germany) was used. The estimated height of this layer will be used to calculate the axial strain of the cell from the position of the piezo-actuator.

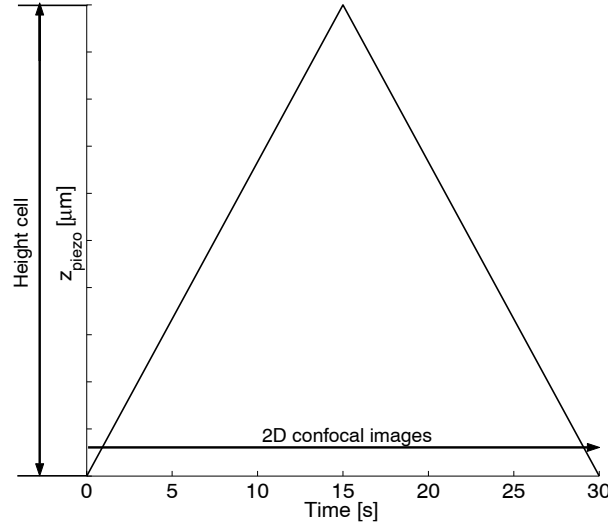


Figure 4.1: Schematic description of the loading protocol in which cells are compressed using a constant velocity of the indenter. During the experiment a time series of two-dimensional images was made.

4.2.3 Data analysis

From the three-dimensional confocal images, the initial values for the height, width, area, surface area, and volume of the cells were calculated as described in section 3.2.4. The recorded signals of the piezo system (z_{piezo}) and the force transducer (U) were filtered using a low pass filter with a cut-off frequency of 10 Hz. The actual position of the indenter was calculated by:

$$z_{indenter} = z_{piezo} - CK(U - U_0), \quad (4.1)$$

where z_{piezo} is the position of the piezo in the axial direction, U_0 the baseline voltage of the force transducer at the start of the experiment, K the sensitivity, and C the compliance of the force transducer. As the contact point between the indenter and the top of the cell is not exactly known, the axial strain of the cell was calculated indirectly in the following way:

$$\epsilon_z = 1 - (z_{debris} - z_{indenter} + H_{debris})/H_0, \quad (4.2)$$

where H_0 is the initial height of the cell and H_{debris} the height of the layer of cell debris at position z_{debris} . It should be noted that ϵ_z is positive in the direction of compression. z_{debris} is defined as the position of the indenter at a force of 20 μN . At this given force, only a thin layer of cell debris was left of the cell.

4.3 Finite element model

4.3.1 Assumptions and mesh generation

To obtain the material properties of the complete cell, the cell was considered to consist of a single material, which was assumed to be homogeneous, isotropic, and incompressible. The cell was represented as an axisymmetric half-sphere with height H_0 and radius R at the base of the cell. The radius was chosen such that the base area represented by the circle with radius R was equal to the base area of the cell as estimated from the three-dimensional confocal images of the undeformed cell. For each cell a separate finite element mesh was built. The boundary nodes of the mesh, which were initially in contact with the cover glass were fixed. All other nodes were allowed to contact with the indenter but did not adhere to it. The nodes actually contacting the indenter were allowed to move freely along the indenter. The indenter was represented as a horizontal plate, which was much stiffer than the cell.

4.3.2 Constitutive equations

The cell was modelled as an incompressible, Neo-Hookean material:

$$\boldsymbol{\sigma} = -p\mathbf{I} + \boldsymbol{\tau}, \quad (4.3)$$

where $\boldsymbol{\sigma}$ represent the Cauchy stress tensor, p the hydrostatic pressure, and $\boldsymbol{\tau}$ an extra stress tensor. For a Neo-Hookean material, $\boldsymbol{\tau}$ is linearly related to the right Cauchy-Green tensor \mathbf{B} according to

$$\boldsymbol{\tau} = G(\mathbf{B} - \mathbf{I}), \quad (4.4)$$

where G denotes the shear modulus, and \mathbf{B} is related to the deformation tensor $\mathbf{F} = (\vec{\nabla}_0 \vec{x})^T$, according to $\mathbf{B} = \mathbf{F} \cdot \mathbf{F}^T$. The shear modulus may be expressed in terms of the Young's modulus E and Poisson's ratio ν via

$$G = \frac{E}{2(1 + \nu)}. \quad (4.5)$$

For an incompressible material the Poisson's ratio equals 0.5 and the conservation of mass reduces to the incompressibility constraint

$$\det(\mathbf{F}) - 1 = 0. \quad (4.6)$$

The finite element method was used to solve the balance of momentum equations using the above given constitutive model. An updated Lagrange formulation was adopted, and spatial discretisation was performed using a quadrilateral Crouzeix-Raviart element that satisfied the inf-sup condition (Bathe, 1996).

4.3.3 Estimation of Young's modulus

For each cell a finite element simulation was performed to account for its specific geometrical features. The finite element simulations provided the reaction force F_{FEM} as a function of the applied axial strain. As the cell was assumed to behave linearly elastic, the shear modulus of the cell could directly be estimated from F_{FEM} and the experimentally obtained reaction force F_{exp} . The experimental shear modulus G_{exp} was related to the finite element shear modulus G_{FEM} by

$$G_{exp} = \alpha G_{FEM}. \quad (4.7)$$

Coefficient α was determined by a least-squares fit, according to

$$\alpha = \frac{\sum_{i=1}^M (F_{FEM}^i F_{exp}^i)}{\sum_{i=1}^M (F_{FEM}^i)^2}, \quad (4.8)$$

with M referring to the number of measured force data points (i) up to an axial strain of 60 %. This level of strain was chosen, because the cell membrane burst at higher axial strains. The Young's modulus of the cell was calculated according to equation 4.5.

4.4 Results

Initial values for the width, height, area, surface area, and volume are reported in table 4.1. The value of H_{debris} appeared to be $1.0 \pm 0.1 \mu\text{m}$ (figure 4.2).

The force versus axial strain curve and the accompanying confocal images at eight time points (*a* to *h*) of a typical compression experiment on a single attached cell are shown in figure 4.3. The undeformed cell is shown in image *a*. With applied axial strain, the force increased and small bulges appeared at the cell membrane surface (image *c*, arrows). The number of bulges increased as well as the size of the bulges, which is shown in image *d* (arrows). The cell membrane ruptured between image *d* and *e*, which was reflected by a decrease in the force. Then the remains of the cell, the cell debris layer, were compressed until the debris layer became so tight that it could not be compressed any further (image *f*). The maximum force of the transducer was reached

Table 4.1: Initial values of width (W), height (H), area (A), surface area (SA), and volume (V) of 12 cells before a compression test (mean \pm SD).

W (μm)	H (μm)	A (μm^2)	SA (μm^2)	V (μm^3)
16.7 ± 3.2	5.8 ± 0.9	572 ± 97	1570 ± 213	2519 ± 580

and the indenter was moved upwards again (image g). A negative peak in the force could be observed, because the cell stuck to the indenter. Immediately after removal of the compressive load, the PI stain entered the cell and the nucleus appeared red (bright nucleus in image h). Finally, the indenter returned to its initial position.

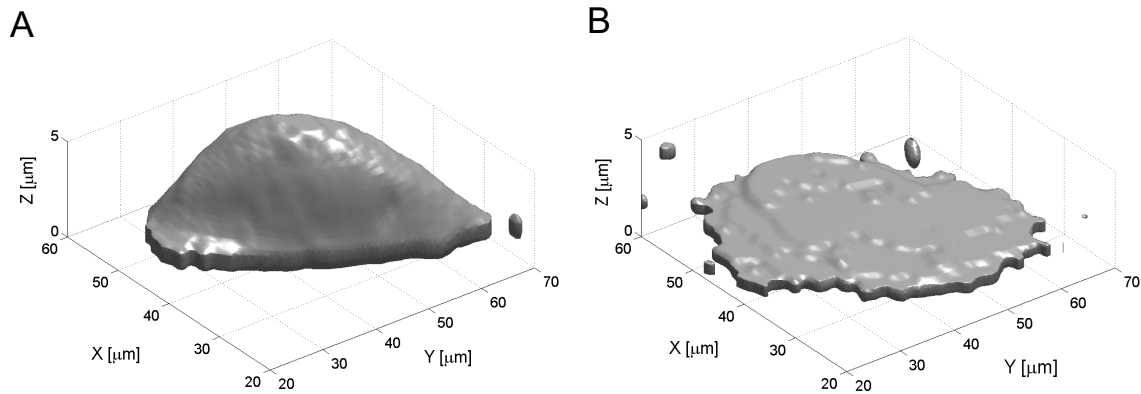


Figure 4.2: Three-dimensional reconstructions of an undeformed cell (A) and the thin layer of cell debris at a compressive force of $20 \mu\text{N}$ (B). The average height of the debris layer was $1.0 \pm 0.1 \mu\text{m}$.

Besides the appearance of bulges at the cell membrane at large axial strains ($> 50\%$), all cells and their nuclei deformed predominantly in the direction of the second principal axis (figure 4.3, see also section 3.3).

The typical reduction in force, related to cell bursting, was observed in 10 cells. The mean bursting force was $8.7 \pm 2.5 \mu\text{N}$ at an axial strain of $72 \pm 4\%$. The experimental force versus axial strain and the mean force versus axial strain curves of all 12 cells are shown in figure 4.4. Mean forces were calculated at deformation increments of 5% . From figures 4.4 A and B, it is evident that the force increased non-linearly with the imposed axial strain. The force versus axial strain curves obtained by the finite element simulations agreed well with the experimentally obtained curves up to an axial strain of 60% , resulting in a correlation coefficient of 0.98 (figure 4.4 A). The estimated Young's modulus was $1.14 \pm 0.32 \text{ kPa}$ (mean \pm SD). Illustrations of deformed finite element meshes at different axial strains are shown in figure 4.5.

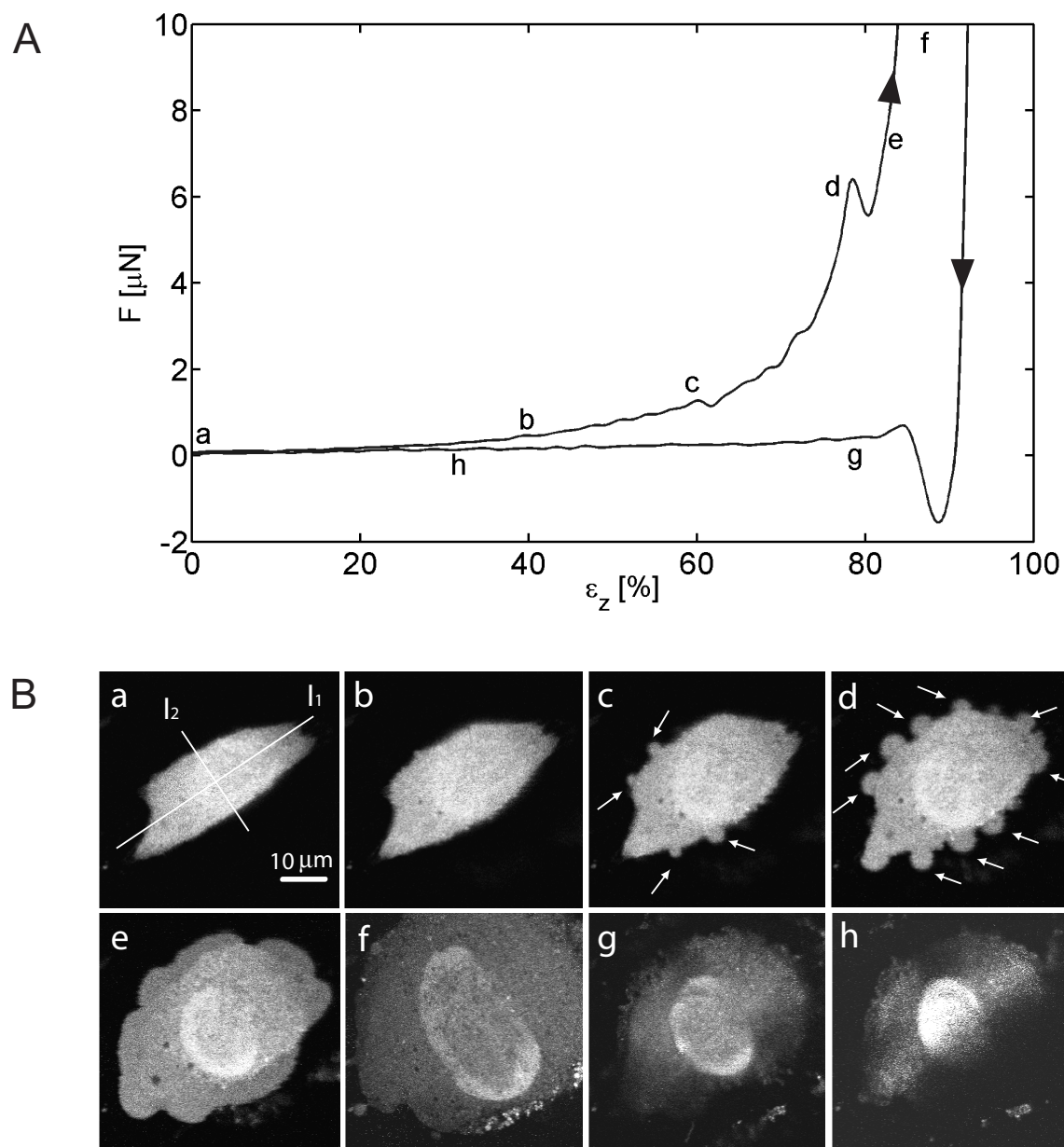


Figure 4.3: A: Force as a function of the applied axial strain obtained by a compression experiment on a single cell.

B: Two-dimensional confocal images of the same cell during downward (images *a-f*) and upward (images *g* and *h*) movement of the indenter. Image *a* shows the undeformed cell and the first (I_1) and second principal axis (I_2) of this cell. Bulges can be observed at the cell membrane in images *c* and *d* (arrows). Cell bursting occurred between image *d* and *e*. The nucleus of the cell appears very bright in image *h*, because the PI stain entered the cell.

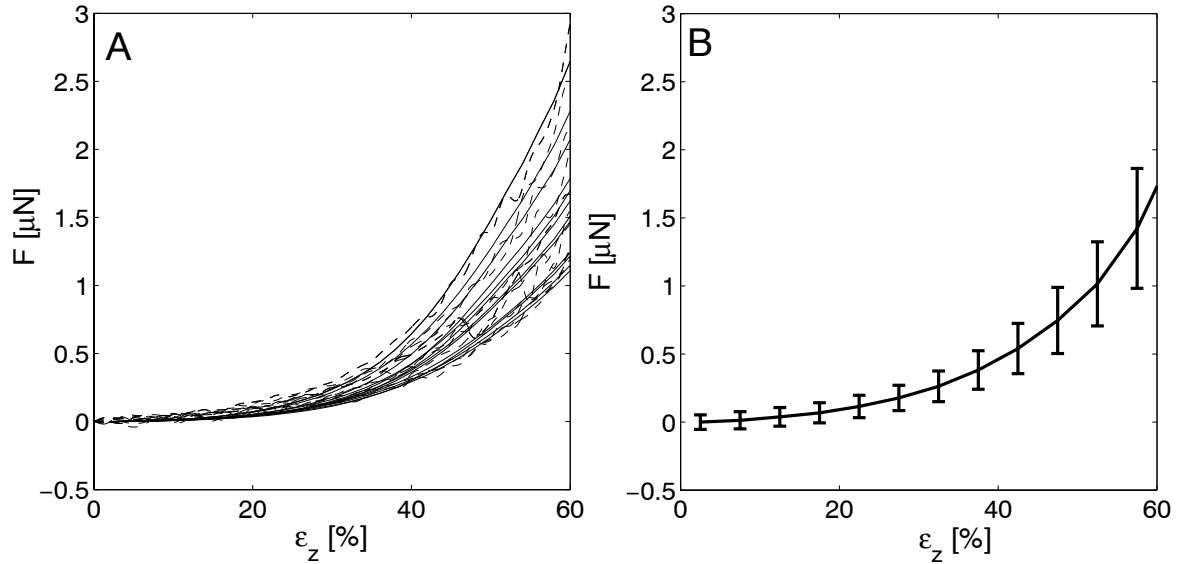


Figure 4.4: A: Force versus axial strain curves obtained from the experiments (dashed) and the finite element simulations (solid).
 B: Mean force versus axial strain curve (mean \pm SD) calculated at 5 % compression intervals.

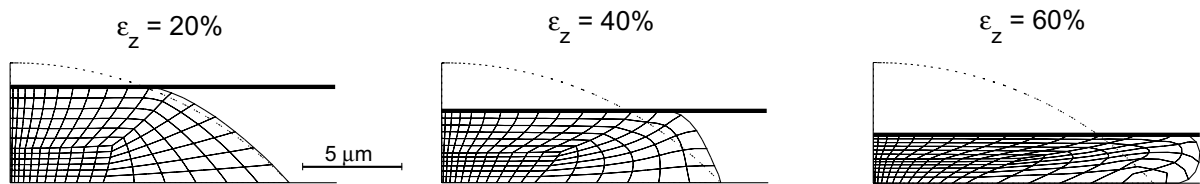


Figure 4.5: Deformed finite element meshes and contour of the undeformed mesh at axial strains of 20 %, 40 %, and 60 %.

4.5 Discussion

In this study, the load-bearing properties of single attached cells were measured using a recently developed loading device (Peeters et al., 2003). Confocal microscopy was used to visualise the cell during compression.

With the loading device, large deformations could be imposed on the entire cell while simultaneously measuring the associated forces. This assures that the properties of the entire cell were examined, as opposed to the local properties of the cell.

The force needed to deform the cell increased non-linearly with the axial strain, which has also been reported in other studies using various cell types and loading devices (Petersen et al., 1982; Daily and Elson, 1984; Zhang et al., 1992; Caille et al., 2002). Using an axisymmetric approximation of the cell geometry, and a Neo-Hookean constitutive model, excellent agreement between predicted and measured force-axial strain curves was obtained, yielding a correlation coefficient of 0.98. The average Young's modulus of the attached cells was estimated at 1.14 ± 0.32 kPa, which was of the same order of magnitude as the modulus obtained by micropipette aspiration (Jones et al., 1999; Bader et al., 2002) or cytoindentation (Koay et al., 2003) for chondrocytes, atomic force microscopy (Mathur et al., 2001) or micropipette aspiration (Theret et al., 1988) for endothelial cells, and atomic force microscopy for fibroblasts (Ricci et al., 1997). Using atomic force microscopy, the Young's modulus of C2C12 cells was estimated at 11.5 kPa (Collinsworth et al., 2002), which is higher than the value reported in this study. This difference might be caused by the fact that the mechanical properties of the cell membrane and the underlying cytoskeleton are probed with atomic force microscopy. These structures may be stiffer than the complete cell. No correlation could be found between the magnitude of the Young's modulus and any of the calculated geometric parameters of the cell (data not shown).

In 80 % of the cell compression experiments, a reduction in the force was observed when the cell burst. It remained unclear why this reduction was not found in all compression experiments. However, this percentage could be increased by increasing the compression speed of the indenter (Shiu et al., 1999). In our study, the compression speed was $0.4 \mu\text{m/s}$ for a cell with a height of $6 \mu\text{m}$, compared to $6 \mu\text{m/s}$ in the study of Shiu et al. (1999). It should, however, be noted that higher compression speeds can result in higher forces and probably higher bursting forces due to the viscoelastic nature of cells. The typical reduction in the force could be discriminated in the force curves, owing to the fast acquisition rate of the force recordings. Cell bursting force was defined as the magnitude of the force at cell bursting. Mean bursting forces were calculated as $8.7 \pm 2.5 \mu\text{N}$ at an axial strain of 72 ± 4 %. Zhang et al. (1991) reported bursting forces of approximately $3 \mu\text{N}$ in similar experiments of non-attached hybridoma cells. These discrepancies might be attributed to the different cell types examined and/or the cell attachment employed in the present study with increased resistance to deformation associated with the structural organisation of the cytoskeleton (Wang and Ingber, 1994; Thoumine and Carodoso, 1999). They also reported a positive correlation between the diameter of the cell and the bursting force. In the present study, no statistically

significant correlation was found between the bursting force and any of the calculated geometric parameters of the cell (data not shown). The axial strain at bursting appeared to be similar for human cancer cells under compression (Takamatsu and Rubinski, 1999; Takamatsu and Kumagae, 2002).

It was impossible to determine the moment of initial contact of the indenter with the cell from the force versus z_{piezo} curves. Therefore, the axial deformation of the cell was calculated indirectly using the height of the undeformed cell and the cell debris layer. The debris layer was measured in a separate experiment with a 63x, 1.4 numerical aperture, oil immersion objective, which has a theoretical resolution of $0.7 \mu\text{m}$. The objective was therefore found to be appropriate to measure the layer of cell debris, which was calculated as $1.0 \pm 0.1 \mu\text{m}$.

Confocal images of the cell during compression revealed that the cell membrane showed bulges at large axial strains, e.g. in excess of 50 %. These bulges were also reported in studies involving micropipette aspiration and amphiphile induced shape alterations in erythrocytes (Artemann et al., 1997; Hägerstrand et al., 2000). In these studies, erythrocytes changed from a normal, discocytic shape to a spiculated, echinocytic shape. On a local level, bulges were observed on the membrane surface of erythrocytes, in a process called membrane microvesiculation (Kralj-Iglic et al., 2000). This phenomenon might be attributed to a local increase of the area difference between the inner and outer lipid layer (Iglic and Hägerstrand, 1999). In a similar manner to the present study, the erythrocytes in the micropipette aspiration experiments were compressed, leading to an increased lateral tension in the membrane (Artemann et al., 1997). This would induce a membrane phospholipid translocation from the inner to the outer lipid layer, thereby increasing the local area difference of the inner and outer lipid layer. Furthermore, high membrane tensions could induce the formation of membrane pores and partial detachment of the lipid bilayer from the underlying cytoskeleton, which further accelerates the lipid translocation (Liu et al., 1989; Hägerstrand et al., 1999, 2000). Further compression of a cell with bulges resulted in an increase of the size of the bulges followed by rupturing of the membrane. Rupturing of the membrane was found to correspond with the typical reduction in force (figure 4.3).

Although the cell membrane clearly ruptured, the nucleus recovered from complete compression without any visible damage. The PI stain clearly demonstrated that the contents of the nucleus remained inside the nuclear membrane during compression. This suggests that the nucleus can withstand very large deformations. In almost all experiments, nuclear deformation could be observed as a result of cell compression. The cells and nuclei deformed predominantly in the direction of the second principal axis of the cell. This phenomenon may be attributed to the actin filaments, which are mainly orientated along the first principal axis of the cell and directly or indirectly connected to the nucleus (see section 3.4).

In summary, for the first time the load-bearing properties of attached cells were quantified, yielding the mean force versus axial strain relationship and the mean bursting force of these cells. Finite element simulations provided an estimate for the Young's modulus. Cell visualisation using confocal microscopy revealed that cell bursting was

preceded by the formation of bulges, which eventually lead to rupturing of the cell membrane.

Chapter 5

Viscoelastic properties of single attached C2C12 myoblasts

5.1 Introduction

The viscoelastic properties of cells determine the degree of cell deformation as a result of mechanical forces and consequently affect cellular structure and function (Elson, 1988). Measurements of these properties also provide means to quantify the effects of drugs, mutations, or diseases on cells. In addition, computational models describing the mechanical environment around the cell within living tissues, thrive on these properties as model input (Wu and Herzog, 2000; Breuls et al., 2002). Such models are used to understand how the mechanical environment of the cell influences cell behaviour *in vivo*. For these models, it is important to reveal the global properties rather than the local properties of the cell. Local mechanical properties vary depending on the position of the cell due to the inhomogeneous nature of the cell interior, whereas global properties attempt to describe the mechanical behaviour of the cell as a whole.

However, the viscoelastic properties of living cells are not easily determined. It requires the quantification of force versus strain relationships of cells under physiological conditions. In addition, the properties of attached cells are important to study, as most cells in living tissue are anchorage dependent and attach to their surrounding extracellular matrix. Therefore, specific loading techniques are needed that maintain the attached and spread morphology of the cells.

So far, cell mechanical properties have been studied using a range of experimental techniques which can roughly be divided into two distinct groups: (i) techniques for global loading of individual cells, like microplate manipulation (Thoumine and Ott, 1997b; Thoumine et al., 1999), micromanipulation (Zhang et al., 1991), or whole cell micropipette aspiration (Evans and Yeung, 1989; Needham and Hochmuth, 1990) and (ii) techniques aiming at local loading of cells, e.g. atomic force microscopy (Mathur et al., 2001; Alcaraz et al., 2003), cell poking (Petersen et al., 1982), bead micromanipulation (Bausch et al., 1998; Laurent et al., 2002) or partial cell aspiration with micropipettes (Sato et al., 1990; Wu et al., 2000). Many of these techniques have revealed the viscoelastic nature of cells. However, none of these techniques has described the viscoelastic behaviour of cells over a wide range of applied deformations or forces, but only consider a small range or do not vary the applied forces or deformations at all. Furthermore, the deformations are generally small, as to ensure that the mechanical behaviour of the cell is linear. For example, atomic force measurements only apply very small deformations (10-100 nm) and micropipette aspiration studies often only use a constant ratio of cell diameter to micropipette diameter (Guilak et al., 2000). The combination of global loading and investigation of attached cells is rarely applied. To the best of our knowledge, the study by Thoumine and Ott (1997b) is the only study in which the global viscoelastic properties of attached cells are studied. However, due to the limited temporal resolution of their force recordings, the applied frequencies were low (minimum period time of 4 seconds) and small relaxation times are thus unable to be resolved.

In the majority of studies examining cellular viscoelasticity, experiments have been performed at room temperature. Exceptions are studies performed by Petersen et al.

(1982) using a cell poker, and A-Hassan et al. (1998) using an atomic force microscope. Their results demonstrate that temperature significantly influences the relaxation time of cells, which cast some doubts on reported viscoelastic properties measured at room temperature.

The present study aims at the quantification of the global viscoelastic properties of attached C2C12 myoblasts under physiological conditions over a wide range of deformations. These properties will be used in studies on compression-induced muscle damage, such as seen in pressure ulcers (Bouten et al., 2003b). In pressure ulcers, muscle tissue is damaged when compressed for prolonged periods of time (> 2 hours) at relatively large deformations (> 20 %). C2C12 muscle cells were chosen because they are commonly used for in vitro muscle studies and have also been successfully applied for studying compression-induced cell damage (Bouten et al., 2001; Breuls et al., 2003b). To determine the viscoelastic properties of C2C12 mouse myoblasts, dynamic experiments were performed using a recently developed loading device for unconfined compression of single cells (Peeters et al., 2003). In conjunction with the ability to compress attached cells, the device allows the experiments to be performed under optimal environmental conditions, comparable to those of a regular CO₂ incubator. The indenter of the device used to compress the cell has similar dimensions as the cell and therefore examines the global mechanical properties. The experiments cover a wide range of frequencies (0.1 to 10 Hz) and axial strains (10 to 40 %). Cells were visualised using confocal laser scanning microscopy. A non-linear viscoelastic model was developed to describe the experiments performed on a single cell with a single set of material parameters.

5.2 Materials and methods

5.2.1 Cell culture and loading device

In this study, attached C2C12 mouse myoblasts were compressed using a single cell loading device. For a description of the culture protocol and the loading device the reader is referred to sections 3.2.1 and 3.2.2.

5.2.2 Dynamic experiments

On the day prior to the experiments, cells were detached from tissue culture flasks by a 2 minutes treatment with 0.05 % trypsin, resuspended in growth medium and then plated on the cover glass within the culture chamber at subconfluent densities (20,000 cells/cm²). After allowing attachment overnight, the cells were stained with 7.5 μM Cell Tracker Green (CTG) and 7.5 μM Propidium Iodide (PI, Molecular Probes, Leiden, the Netherlands), which stain the cytoplasm of living cells and the nucleus of dead cells, respectively (Breuls et al., 2003a). The loading device was then placed on the stage of the confocal microscope and a cell was selected for compression. Using the confocal microscope in reflection mode, the indenter was moved using the micromanipulators to a

position of 20 μm above the cell. Then a stack of confocal images of the undeformed cell was taken using a 40x, 0.95 Numerical Aperture, air objective (Plan-Apochromat, Zeiss, Germany). A 25 mW Argon ion laser at 488 nm was used to excite CTG, whereas PI was excited at 543 nm with a 1 mW Helium-Neon laser. To avoid dye saturation, excitation power was set to 1 % (488 nm) and 2 % (543 nm) of maximum laser power. Images were taken at a sampling density (x,y,z) of $0.3 \times 0.3 \times 0.3 \mu\text{m}^3$. A linear z-correction factor of 1.33 was used to compensate for geometric distortion due to a mismatch in refractive index of the growth medium and air. The height of the cell was estimated using the image software of the microscope. The indenter was then lowered using the piezo-actuator to load the cell with a small initial axial strain of approximately 10 % and a second stack of images was taken. Then, a series of dynamic experiments was performed.

For the dynamic series, sinusoidal input signals (10 cycles) with a dynamic amplitude of 0.25 μm and an offset of 0.25 μm at frequencies of successively 10^{-1} , $10^{-0.5}$, 10^0 , $10^{0.5}$, and 10^1 Hz were applied to the piezo-actuator. These values for the amplitude and offset resulted in a maximum displacement of 0.50 μm of the piezo-actuator. After each experiment, the amplitude and offset were increased by 0.25 μm and a new dynamic experiment was conducted. This procedure was repeated until the cell burst. During each experiment, a time series of confocal images was taken with a lateral sampling size (x,y) of $0.3 \times 0.3 \mu\text{m}^2$ and a sampling time of 1 s per image. In total, 11 individual cells were subjected to a series of dynamic experiments. On average, each cell was subjected to 25 dynamic experiments (5 amplitudes at 5 frequencies), which took approximately 15 minutes.

Force and position of the piezo-actuator were recorded with a sampling frequency of 1000 Hz.

5.2.3 Data analysis

The recorded signals of the piezo-actuator $z_{piezo}(t)$ and the force transducer $U(t)$ were filtered using a band-pass filter with a frequency bandwidth between 0.5 x and 5 x the applied frequency. Then the data of the last 8 cycles were averaged. The actual position of the indenter was calculated by:

$$z_{indenter}(t) = z_{piezo}(t) - CK(U(t) - U(t_0)), \quad (5.1)$$

where $U(t_0)$ is the baseline voltage of the force transducer at the start of the experiment, K the sensitivity, and C the compliance of the force transducer. The axial strain of the cell was calculated by adding the initial strain $\epsilon_z(t_0)$ to the extra strain $\Delta\epsilon_z(t)$ imposed during the dynamic experiment:

$$\epsilon_z(t) = \epsilon_z(t_0) + \Delta\epsilon_z(t) = \epsilon_z(t_0) + \frac{z_{indenter}(t) - z_{indenter}(t_0)}{H}, \quad (5.2)$$

where H is the height of the undeformed cell and $z_{indenter}(t_0)$ denotes the position of the indenter at the start of the experiment. The initial strain $\epsilon_z(t_0)$ was based on the height of the undeformed cell H and the height of the cell at the start of the experiment $H(t_0)$. The height of the cell at these two different points in time was calculated with a custom-made software program in Matlab (The Mathworks, Natick, MA) by applying a full width half maximum threshold to the stack of confocal images of the cell. Furthermore, the area at the base of the undeformed cell A_b , the surface area, the volume, and the width of the undeformed cell was calculated by the same program. See section 3.2.4 for a more extensive description of the calculation of these parameters.

5.2.4 Viscoelastic model

A non-linear viscoelastic model was used to estimate the material parameters of a single cell. The model, derived from the standard linear solid model, consists of a Maxwell element in parallel with a spring with spring constant k_1 (figure 5.1 B). The Maxwell element consists of a dashpot with relaxation time τ_r and a non-linear spring with spring constant $k_2(\epsilon_z)$:

$$k_2(\epsilon_z) = k_{20}e^{\alpha\epsilon_z^2}, \quad (5.3)$$

where k_{20} is a spring constant and α represents a non-linear coefficient. If α is zero, the model equals the standard linear solid model.

The following differential equation can be derived for this model:

$$\sigma + \tau_r \frac{d\sigma}{dt} = \tau_r [k_1 + k_2(\epsilon_z)] \frac{d\epsilon_z}{dt} + [k_1 + \tau_r \frac{dk_2(\epsilon_z)}{dt}] \epsilon_z \quad (5.4)$$

To compute the force, the stress has to be divided by the contact area between the cell and the indenter. This contact area obviously increases with increasing indentation depth of the glass indenter. Therefore, the cell was represented by a half ellipsoid with height H and base area A_b (figure 5.1 A). The contact area A_c of the cell and the indenter can be described as a function of ϵ_z :

$$A_c = A_b(1 - (1 - \epsilon_z)^2). \quad (5.5)$$

Now the time derivative of σ can be calculated:

$$\frac{d\sigma}{dt} = \frac{d(F/A_c)}{dt} = \frac{1}{A_c} \frac{dF}{dt} - \frac{F}{A_c^2} \frac{dA_c}{dt}, \quad (5.6)$$

with

$$\frac{dA_c}{dt} = 2A_b(1 - \epsilon_z) \frac{d\epsilon_z}{dt}. \quad (5.7)$$

Finally, the time derivative of $k_2(\epsilon_z)$ is given by:

$$\frac{dk_2(\epsilon_z)}{dt} = \frac{dk_2(\epsilon_z)}{d\epsilon_z} \frac{d\epsilon_z}{dt} = 2\alpha\epsilon_z k_{20} e^{\alpha\epsilon_z^2} \frac{d\epsilon_z}{dt}. \quad (5.8)$$

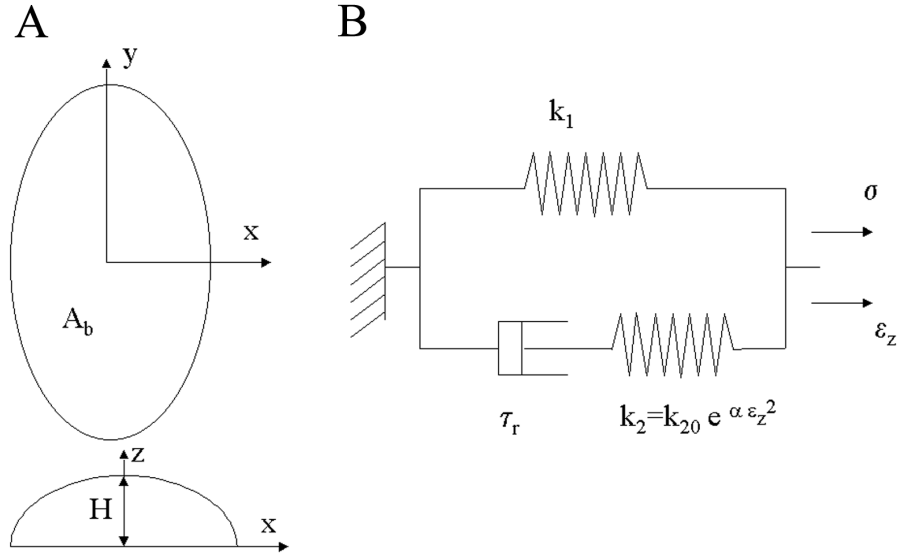


Figure 5.1: A: Geometric representation of the undeformed cell with height H and area at the base A_b .

B: Non-linear viscoelastic model used to describe the dynamic experiments with spring constants k_1 , $k_2(\epsilon_z)$ and relaxation time τ_r .

Equations 5.3, 5.5, 5.6, 5.7, and 5.8 can then be substituted into differential equation 5.4. To obtain the relationship between F and ϵ_z , the differential equation was solved numerically using an implicit solution method. The model was fitted on all experimental data for each cell using a least-squares algorithm. The algorithm searches for the best combination of parameters k_1 , k_{20} , α , and τ_r by minimising the squared deviation of the experimental F versus ϵ_z relationship and the one predicted by the non-linear viscoelastic model. In this way, the series of dynamic experiments performed on one cell were described by a single set of material parameters. The material parameters of all cells were presented as mean \pm standard deviation.

5.3 Results

In total, 11 cells were subjected to a series of dynamic experiments. The values of the width, height, area, surface area, and volume of each cell before a dynamic series of experiments was conducted, are summarised in table 5.1. The initial axial strain $\epsilon_z(t_0)$ applied to the cells prior to the experiments was $8.0 \pm 3\%$. The forces resulting from dynamic experiments with low amplitudes, e.g. $\Delta\epsilon_z(t) < 10\%$, could not be measured reliably as the accuracy of the force transducer was approximately 30 nN. The results from dynamic experiments with very high amplitudes, e.g. $\Delta\epsilon_z(t) > 40\%$, were also

Table 5.1: Initial values of width, height, area, surface area, and volume of all cells before a dynamic experiment was conducted (mean \pm SD).

Width (μm)	Height (μm)	Area (μm^2)	Surface Area (μm^2)	Volume (μm^3)
16.5 ± 3.0	6.0 ± 0.8	564 ± 180	1447 ± 403	2454 ± 883

not taken into account when the confocal images of the cell showed the entry of the stain PI into the cell, indicating cell death. The typical response of an individual cell to a sinusoidal input signal with an amplitude and an offset of $0.5 \mu\text{m}$ at 1 Hz is shown in figure 5.2. It also shows the effect of the band-pass filter, which was applied to the recorded signals of the piezo-actuator and the force transducer.

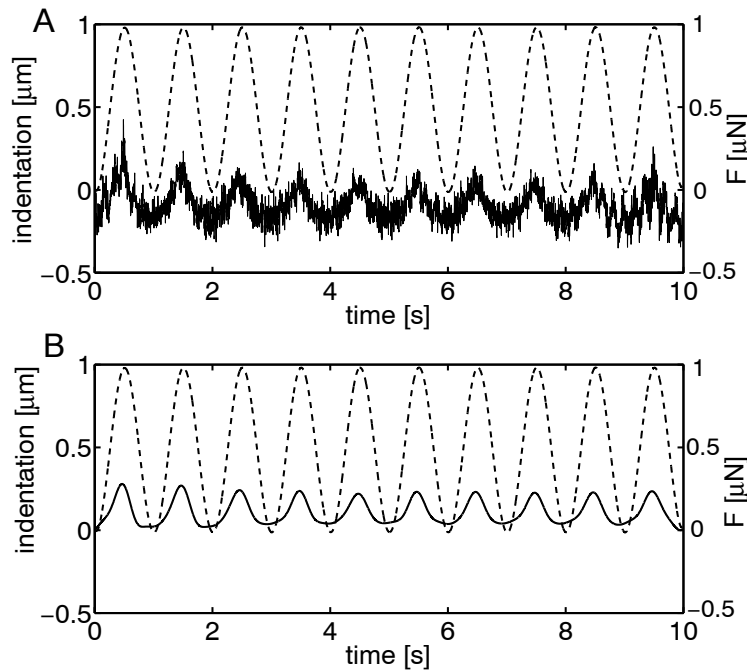


Figure 5.2: Force (solid curves) and indentation depth (dashed curves) as a function of time before (A) and after (B) filtering obtained from a dynamic experiment.

As mentioned in section 5.2.3, the force of the previous 8 cycles was averaged. The results of dynamic experiments in which 10 cycles with an amplitude and offset of $0.5 \mu\text{m}$ at 1 Hz was applied 3 times to the same cell are shown in figure 5.3. The time between the experiments was approximately 2 minutes. It shows the mean force and the standard deviation of the previous 8 cycles for each experiment separately. The average standard deviation of these experiments is $0.012 \mu\text{N}$, which is 6.5 % of the maximum force. These data indicate that there is only small variability between experiments.

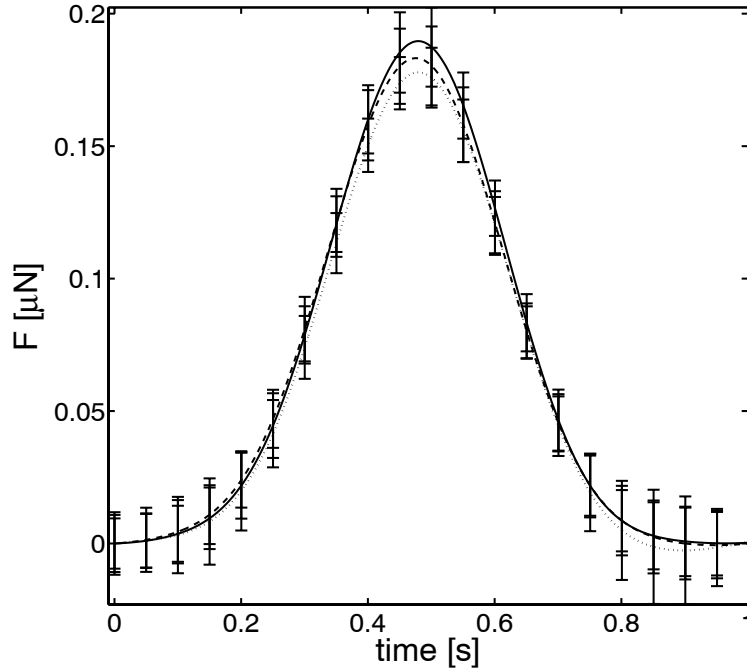


Figure 5.3: Force as a function of time obtained from three dynamic experiments performed on one cell. In each dynamic experiment the cell was subjected to 10 cycles with an amplitude and offset of $0.5 \mu\text{m}$ at 1 Hz. For each experiment, the forces of the previous 8 cycles were averaged. The error bars represent the standard deviation of each experiment.

The typical force as a function of the axial strain relationship for one cell at 5 different frequencies and 3 different axial strains is shown in figure 5.4. Hysteresis is clearly evident from these curves, indicating the viscoelastic behaviour of the cell subjected to unconfined compression. The maximum force increased with frequency, again emphasising the viscoelastic behaviour. Furthermore, the non-linear behaviour became more pronounced at higher axial strains and frequencies. The fit obtained by the non-linear viscoelastic model is also shown in figure 5.4. All the dynamic experiments could be described by a single set of material parameters.

The parameters for the non-linear viscoelastic model are summarised in table 5.2. Although the model is generally within the envelope of the experimental data, the standard deviations of the material parameters were relatively large. For example, the standard deviation of parameter k_{20} was almost 70 % of the mean value.

Confocal images of a cell in the undeformed state, with a small initial strain $\epsilon_z(t_0)$, and during a series of dynamic experiments are shown in figure 5.5. In panel D, bulges originating from the cell membrane can be observed. In all experiments bulges appeared on the cell membrane at axial strains larger than 40 %. Initially, these bulges disappeared within a few seconds after load removal. However, when the axial strain was increased,

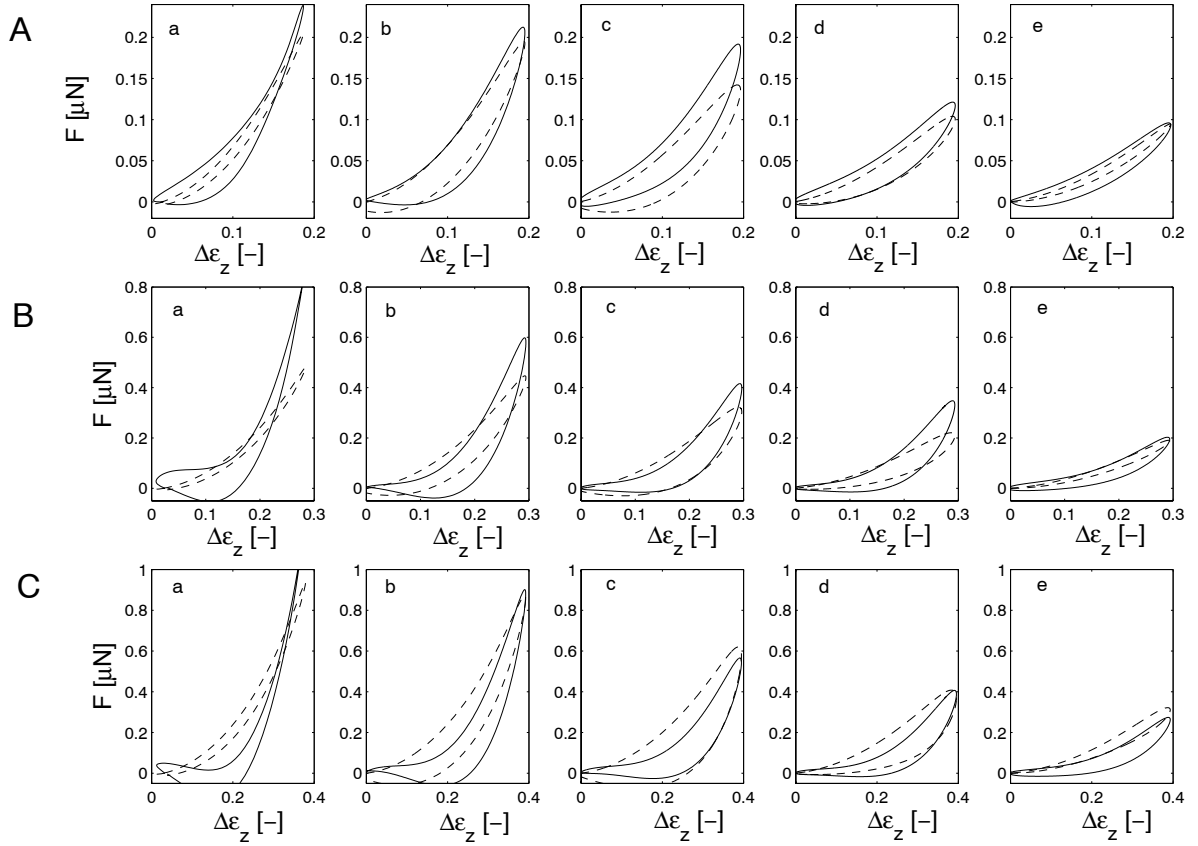


Figure 5.4: Force as a function of axial strain (solid curves) obtained from dynamic experiments on one cell at different applied frequencies (10^1 (a), $10^{0.5}$ (b), 10^0 (c), $10^{-0.5}$ (d), and 10^{-1} (e) Hz) and amplitudes of indentation (0.5 (A), 0.75 (B), and 1 μm (C)). The fit obtained by the non-linear viscoelastic model is also shown (dashed curves).

the size of the bulges increased and the cell membrane ruptured. This led to the entry of the stain PI into the cell, as observed from the red cell nucleus. Cell membrane rupture occurred at a mean axial strain of 54 ± 6 %. Furthermore, cells tended to burst at high frequencies. Eight cells burst at a frequency higher than 1 Hz and only three cells at a frequency lower than 1 Hz.

Table 5.2: Summary of the parameters of the non-linear viscoelastic model obtained from dynamic experiments performed on 11 cells: k_1 , k_{20} =spring constants, α =non-linear coefficient, τ_r =relaxation time.

k_1 (Pa)	k_{20} (Pa)	α (-)	τ_r (s)
2120 ± 900	1960 ± 1350	14.0 ± 4.3	0.30 ± 0.12

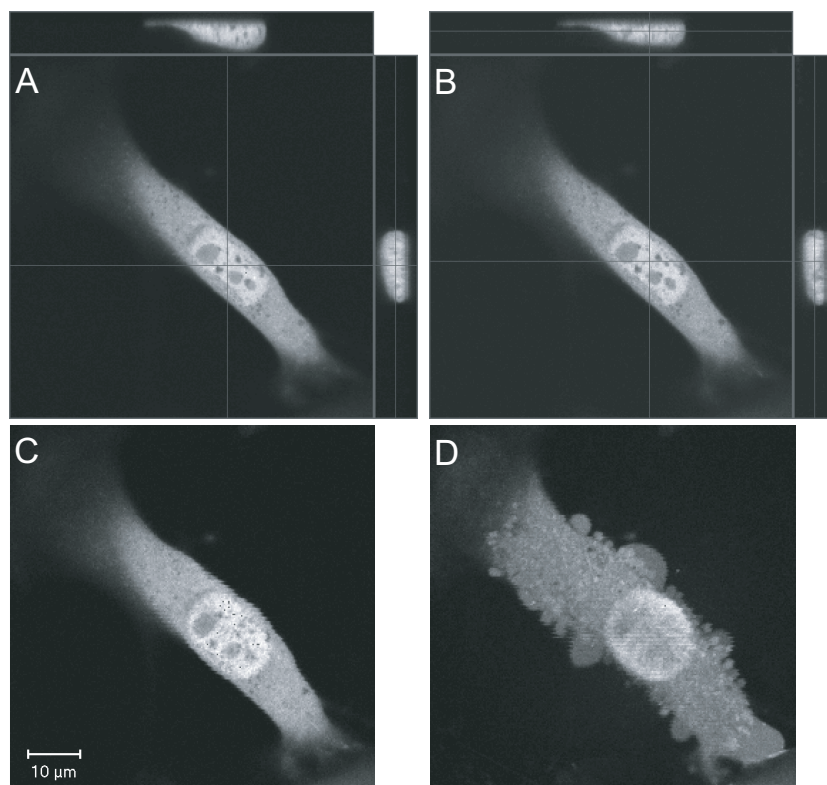


Figure 5.5: Orthogonal projections of an undeformed cell (A) and a compressed cell with initial strain $\epsilon_z(t_0) = 12\%$ (B). Panels C and D show images of the same cell during dynamic experiments at axial strains of $\epsilon_z(t) = 30\%$ and 55% , respectively. The cell in panel D shows the ruptured membrane of the cell.

5.4 Discussion

The aim of the current study was to quantify the global viscoelastic properties of single attached C2C12 myoblasts under compression. The viscoelastic properties were examined by performing a series of dynamic experiments over two frequency decades (0.1-10 Hz) and at a range of axial strains ($\sim 10 - 40\%$). Each series of experiments was described by a single set of material parameters of a non-linear viscoelastic model. The force versus axial strain curves obtained by the dynamic experiments revealed several characteristic phenomena.

First, hysteresis appeared to be present at all measured frequencies and axial strains (figure 5.4). The hysteresis was small at the smallest applied frequency (0.1 Hz), increased with frequency of approximately 1 Hz and decreased again at the highest applied frequency (10 Hz). This finding implies that the component of cell stiffness attributable to energy dissipation and friction ($G''(f)$) shows a maximum at a certain

characteristic frequency. Thoumine and Ott (1997b) showed similar behaviour, whereas studies using atomic force microscopy (AFM) reported an increase of hysteresis with increasing frequency (Mathur et al., 2001; Alcaraz et al., 2003). Magnetic twisting cytometry (MTC) on epithelial cells (Puig-De-Morales et al., 2001) and smooth muscle cells (Maksym et al., 2000) yielded respectively an increase or constant value of $G''(f)$ and a more or less constant phase angle with increasing frequency. Differences might be attributed to different loading conditions, e.g. the imposed forces in AFM and MTC studies reach a maximum of respectively 0.3 nN and 4 Pa compared to at least 40 nN or 100 Pa in the present study and microplate studies. Moreover, AFM and MTC studies reveal the viscoelastic properties of specific parts of the cell rather than the cell as a whole.

Second, the maximum force of the force versus axial strain curves exhibited a marked increase with frequency (figure 5.4). This finding was also reported in studies using AFM (Alcaraz et al., 2003), cell poking (Petersen et al., 1982) and microplate manipulation (Thoumine and Ott, 1997b). On the contrary, Mathur et al. (2001) observed increased indentation depths at higher probe velocities using force controlled measurements.

In addition, the force versus axial strain curves deviated considerably from an elliptical form. This strongly suggested non-linear characteristics of the cell. The non-linear behaviour became more pronounced at high axial strains ($> 20\%$) and high frequencies.

The non-linear viscoelastic model was based on the standard linear solid model, which is often used to describe dynamic, relaxation and creep experiments on cells (Elson, 1988). Ideally, such a model should be able to describe the whole range of experiments performed in this study using only a single set of material parameters. At low frequencies, the non-linear behaviour could be attributed to the increasing contact area between the cell and indenter rather than the non-linear material behaviour. Therefore, the spring with constant k_1 was considered to be linear. This was in agreement with the finite element simulations performed in chapter 4, which showed that the increasing contact area accounted for the non-linear force-axial strain curves.

Because the non-linear behaviour became more pronounced at high frequencies, the linear spring of the Maxwell element was replaced by a non-linear spring. The contribution of this spring is particularly relevant at high frequencies, when the dashpot is a rather stiff structure. At low frequencies, the contribution of the non-linear spring becomes smaller. The use of this non-linear spring allowed to describe the viscoelastic behaviour over a wide range of applied strains and frequencies using only a single set of material parameters. However, the model oversimplifies the cell structure, assuming it to be a homogeneous solid, although the cell is a non-homogeneous structure.

Certain structures like the nucleus and the cytoskeleton influence the mechanical properties of the cell (Kan et al., 1999; Yoshikawa et al., 1999; Yamada et al., 2000; Sato et al., 2000; Caille et al., 2002). Isolated nuclei from chondrocytes have been shown to be at least three times stiffer and nearly twice as viscous as the surrounding cytoplasm (Guilak et al., 2000). The oversimplification of the model could explain the large standard deviation of the estimated material parameters. More obvious however,

the large variability can be inherent to the behaviour of cells (Karcher et al., 2003). The present experimental technique is most unlikely to contribute to this, because three successive dynamic experiments on the same cell yielded almost identical results (figure 5.3). The standard deviations reported here are similar or smaller than those reported in studies using a standard linear solid model (Sato et al., 1990; Thoumine and Ott, 1997b; Guilak et al., 2000; Koay et al., 2003).

Although the non-linear viscoelastic model has not been applied in other studies, the magnitude of the parameters in the present study can best be compared with parameters of the standard linear solid model as determined in several studies (table 5.3). This table reveals the large variation of the parameters, which can be attributed to the different cell types, loading devices, loading protocols, operating conditions, and degree of cellular attachment.

Table 5.3: Parameters for the standard linear viscoelastic solid model as obtained for different cell types using several different experimental techniques and operating conditions.

cell type	device	F or P	T ($^{\circ}C$)	k_1 (Pa)	k_2 (Pa)	τ_r (s)
chondrocytes ¹	indentation	50 nN	25-37	1090	1140	1.32
chondrocytes ²	micropipette	100-500 Pa	21	200	300	10
hepatocytes ³	micropipette	300 Pa	24	87	33	0.18
fibroblasts ⁴	microplates	20-100 nN	23	960	840	13
endothelial cells ⁵	micropipette	200 Pa	23	100	200	39.5
neutrophils ⁶	micropipette	40 Pa	22	31	76	0.22
neutrophils ⁷	micropipette	20 Pa	22	28	74	0.18
myoblasts ⁸	compression	0.1-1 μ N	37	2120	1960	0.30

F = applied force, P = applied pressure, T = temperature.

References are 1: Koay et al. (2003), 2: Guilak et al. (2000), 3: Wu et al. (2000), 4: Thoumine and Ott (1997b), 5: Sato et al. (1990), 6: Chien and Sung (1984), 7: Schmid-Schönbein et al. (1981), 8: this study.

Micropipette studies generally report lower values for k_1 and k_2 than indentation studies. This might be attributed to the less organised cytoskeleton in the suspended cells used in the micropipette studies compared to attached cells in indentation studies (Coughlin and Stamenović, 1998; Thoumine and Carodoso, 1999). Furthermore, deformation of the entire cell or just a part of the cell will yield different results, mainly due to the involvement of the nucleus, which is stiffer than the cytoplasm of cells (Guilak et al., 2000; Lee et al., 2000). The values for k_1 and k_2 obtained in the present study are generally higher than those reported in other studies (table 5.3). This can be explained by the fact that the cells in this study are attached and the deformations applied to the cells are larger, namely between 10 and 40 % axial strain. Furthermore, differences can

be caused by the cell type. For example, skeletal muscle cells are stiffer than endothelial cells but less stiff than cardiac cells (Mathur et al., 2001).

The relaxation time found in the present study lies within the range of values reported by other studies (table 5.3). However, it should be noted that the relaxation time is strongly dependent on temperature. A-Hassan et al. (1998) reported time constants which are 1-3 orders of magnitude larger at 22 °C (~ several seconds) than at 37 °C (~ 0.8 seconds). Furthermore, Petersen et al. (1982) reported a more rapid recovery from sustained stress at 37 °C than at 25 °C. Almost all experiments of the studies reported in table 5.3 are performed at room temperature, which probably caused an overestimation of the relaxation time at 37 °C.

Simultaneous recordings of confocal images during the dynamic experiments allows examination of the relationship between applied axial strain and cellular breakdown, as shown by the entry of the PI stain into the cell. The magnitude of this strain was 54 ± 6 % which is considerably lower than the mean value of 72 ± 4 % reported in chapter 4. This difference can be attributed to the time the cells were exposed to deformation in the present study. Typically, a series of dynamic experiments on a single cell took 15 minutes, whereas the quasi-static experiments lasted 15 seconds (chapter 4). Furthermore, the indentation velocity and the number of repeated indentations may also contribute to this difference. As described in section 5.3, the cell membrane ruptured in most cases at high frequencies. The highest indentation velocity in the dynamic experiments was approximately 50 $\mu\text{m/s}$ (displacement of 2.5 μm in 0.05 seconds), whereas the indentation velocity in the experiments described in the former chapter is approximately 0.4 $\mu\text{m/s}$ (displacement of 6 μm in 15 seconds).

Another observation from the confocal images, was the development of bulges (figure 5.5) in a similar manner to that observed in the quasi-static experiments. Similar bulges were reported in erythrocytes deformed in micropipette aspiration experiments (Artmann et al., 1997). This phenomenon might be connected to a local increase of the area difference between the inner and outer lipid layer of the cell membrane (Iglic and Hägerstrand, 1999). The high membrane tension as a result of compression and even possibly the detachment of the actin cortex from the lipid bilayer, could cause translocation from the inner to the outer lipid layer, thereby increasing the local area difference (Liu et al., 1989). Initially, the bulges disappeared after removal of the load. However, with increasing strain the size of the bulges increased until the membrane ruptured.

In conclusion, it may be stated that the viscoelastic properties of single attached C2C12 myoblasts were quantified using a specially designed loading device and a non-linear viscoelastic model. The model was able to describe the experiments over a wide range of frequencies (0.1 - 10 Hz) and axial strains (~ 10 - 40 %) using only a single set of material parameters. To the authors' knowledge, it is the first time that the global viscoelastic properties of attached cells have been quantified over such a wide range of strains. Furthermore, the experiments were performed under optimal environmental conditions and the results are therefore believed to reflect the viscoelastic mechanical behaviour of cells, such as would be present *in vivo*.

Related to the present study on the aetiology of pressure ulcers, these viscoelastic properties could be used as input for a numerical model connecting global external loads on living tissue to the local internal loads that the cell actually experiences (Breuls et al., 2002). In future studies, it will be investigated how muscle damage evolves over time under the influence of a prolonged loading period. It might be predicted that a change of the internal structure of the cell would occur and that this would be reflected in the viscoelastic mechanical properties. This can either be a change of the elastic stiffness, the ratio between the viscous and elastic properties, or the time constants involved.

Chapter 6

Decreased mechanical resistance to deformation in cells lacking LMNA gene expression. Implications for the development of laminopathies

6.1 Introduction

Nuclear lamins are cytoskeletal proteins located at the inner nuclear membrane and belong to the group of intermediate filament proteins. Two main classes can be distinguished, i.e. A- and B-type lamins.

B-type lamins are either products of the LMNB1 gene, encoding lamin B1 (Lin and Worman, 1995), or the LMNB2 (LMN2) gene (Biamonit et al., 1992), encoding lamins B2 and B3 (Furukawa and Hotta, 1993).

Until now, at least three different proteins are known to arise from the A-type lamin gene (LMNA), (Lin and Worman, 1993), i.e. lamin A, lamin A Δ 10, and lamin C (Machiels et al., 1996). Unlike B-type lamins, which are mainly expressed in most eukaryotic cells, A-type lamins are differentially expressed. Expression of A-type lamins is reduced or absent in early embryonic cells, in cells of a low degree of differentiation, in cells of the cellular immune system, and in highly proliferating cells (Röber et al., 1989, 1990; Broers et al., 1997).

While some functional aspects of the nuclear lamins have been established, several other proposed functions remain to be confirmed. For B-type lamins it has become clear that absence of these proteins is not compatible with life. Using small, interfering RNA (siRNA) it is possible to inactivate mRNA, encoding for a specific protein, to prevent the production of this protein. Silencing of lamin B1 or lamin B2 by siRNA produces apoptotic features in both mammalian cells and in cells from *C. elegans* (Harborth et al., 2001; Cohen et al., 2002). Apparently, the presence of B-type lamins is critical for vital cellular processes, such as the DNA elongation phase during DNA synthesis (Moir et al., 2000). Since mutations in either LMNB1 or LMNB2 can cause cell death, this can explain why no mutations in these genes have been found in human heritable diseases.

In contrast to B-type lamins, the loss of A-type lamins leads to specific loss of functions. This can be seen in human heritable diseases and in mouse LMNA knockouts. However, the exact impact of the loss of LMNA expression on the functioning of cells is not yet well understood. Only in homozygotes the complete loss of A-type lamins leads eventually to the death of such an organism because of heart failure, as reported for both mice and humans (Sullivan et al., 1999; Muchir et al., 2003).

A variety of inherited diseases is associated with mutations in the LMNA gene. These diseases are collectively called laminopathies, and include Emery Dreifuss Muscle Dystrophy (EDMD) (Bonne et al., 1999), dilated cardiomyopathy type 1A (Fatkin et al., 1999), limb-girdle muscular dystrophy type 1B (Muchir et al., 2000), familial partial lipodystrophy (Cao and Hegele, 2000; Speckman et al., 2000), Charcot-Marie-Tooth disease type 2 (Sandre-Giovannoli et al., 2002), and a rare childhood syndrome of premature ageing, the Hutchinson-Gilford syndrome (Cao and Hegele, 2003; Eriksson et al., 2003; Sandre-Giovannoli et al., 2003). If A-type lamins would have only a single, well-defined function, it would be very difficult to explain the variety of symptoms seen in this relatively heterogeneous group of patients.

To explain this spectrum of diseases, two main working hypotheses are currently exploited. The first hypothesis states that patients with laminopathies experience

mechanical weakness in cells, caused by a disturbed nuclear architecture. This *mechanical stress* hypothesis could explain the loss of muscle tissues at the onset of adulthood in affected patients as seen in the group of muscle failure-related diseases. The second hypothesis explaining the development of symptoms could be the loss of gene regulatory functions caused by mutations in A-type lamins. Studies have suggested that A-type lamins could play a role in gene regulation by interaction with the Rb protein (Mancini et al., 1993; Ozaki et al., 1994), possibly mediated by LAP2alpha (Markiewicz et al., 2002) by the formation of transcriptional complexes with transcription factors such as SREB2 (Lloyd et al., 2002) and MOK2 (Dreuillet et al., 2002). However, direct evidence on the role of A-type lamins in gene regulation remains to be delivered.

In this chapter, the *mechanical stress* hypothesis was tested. Therefore, the role of A-type lamins was examined in providing structural support to the nucleus and to cells in general, by performing compression experiments on two populations of cells: fibroblasts containing normal expression of the LMNA gene (MEF⁺⁺ cells) and cells lacking expression of the LMNA gene (MEF⁻⁻ cells). Since the nucleus contributes for a large part to the mechanical properties of a cell (Guilak et al., 2000; Caille et al., 2002), a disturbance of the nuclear architecture should be reflected by a decreased mechanical resistance to deformation of these cells.

Unconfined compression experiments were performed on single cells using a recently developed loading device (Peeters et al., 2003). The device enables quantification of the mechanical resistance to deformation. Furthermore, during the experiments cell deformation and possible cell damage can be observed real-time using confocal microscopy. Using this device, a significantly reduced mechanical resistance to deformation could be measured in cells lacking expression of the LMNA gene. In contrast to nuclei of normal cells, the integrity of MEF⁻⁻ nuclei was lost after a compression experiment. Moreover, the preferred deformation direction as seen in the nuclei of MEF⁺⁺ cells, was not observed in MEF⁻⁻ nuclei. This observation could be related to the absence of a link between the nucleus and the cytoskeleton in MEF⁻⁻ cells, presumably the actin cytoskeleton, which was disturbed in cells lacking LMNA expression. It was also investigated whether transfection of MEF⁻⁻ cells with lamin A or lamin C could restore the characteristics of the MEF⁻⁻ cells.

6.2 Materials and methods

6.2.1 Cell culture

Wild-type mouse embryonic fibroblasts (MEF⁺⁺) as well as LMNA knockout mouse embryonic fibroblasts (MEF⁻⁻) were obtained as described previously (Sullivan et al., 1999). Cells were cultured in DMEM containing 10 % fetal bovine serum and 0.1 % gentamycin (all purchased from Biochrom, Berlin, Germany). Cells were passaged by splitting at a 1:3 to 1:5 ratio using 0.25 % trypsin-EDTA. MEF⁻⁻ cells were used at passages 7 to 9. MEF⁺⁺ cells were used at passages 5 to 15.

6.2.2 Transfection

In order to restore LMNA protein expression in LMNA null cells, MEF^{-/-} cells were transfected with cDNA encoding either lamin A-EGFP or lamin C-EGFP (Enhanced Green Fluorescent Protein). Both lamin A-EGFP and lamin C-EGFP were obtained by cloning the lamin A or lamin C cDNA fragment from the PS65T-C1 vector (Broers et al., 1999) into the EGFP-vector (Clontech). Alternatively, cells were cotransfected with lamin C (cDNA cloned into pcDNA3, FIRMA) and lamin A-EGFP. Transfections were performed using Genejammer (InvitroGen) according to the manufacturer's instructions. Typically, 10-20 % of the MEF^{-/-} cells were transfected with lamin A-EGFP (MEF^{-/-} rescue A) or lamin C-EGFP (MEF^{-/-} rescue C). MEF^{-/-} cells, which were subjected to the transfection procedure but did not show any A-type lamin expression, are referred to as MEF^{-/-} control cells. No stable transfectants could be generated from this cell line. Morphologic and mechanical properties of transfected cells were studied within two to three days after transfection.

6.2.3 Immunofluorescence studies

Cells were cultured on glass slides and fixed with 4 % formaldehyde in PBS for 15 minutes, followed by permeabilisation in 0.1 % Triton X-100 for 10 minutes at room temperature (RT). Primary antibodies were applied onto the cells for one hour. The following primary antibodies were used:

- Mouse monoclonal antibody (MoAb)133A2 (IgG3, 3 μ g/ml purified Immunoglobulin) (Hozak et al., 1995; Machiels et al., 1995) was a kind gift from Dr. Y. Raymond (Montréal, Canada). This antibody recognises lamin A and is reacting with the epitope consisting of amino acids 598 \pm 611.
- Affinity-purified rabbit polyclonal antiserum RaLC (1:50 dilution in IF and immunoblotting) (Venables et al., 2001) directed against the C-terminal sequence VSGSRR (position 567 \pm 572) of human lamin C, and exclusively reactive with lamin C and not lamin A.
- Mouse MoAb JOL2 (IgG1; dilution 1:100), reacting with an epitope (amino acids 464 \pm 572) in the C-terminal domain of lamin A, A Δ 10 and C (Dyer et al., 1997).
- Mouse MoAb to nucleoporin p62 (IgG2b, dilution 1:300; Transduction Laboratories, Lexington, KY, USA; (Carmo-Fonseca et al., 1991)).
- Mouse MoAb to emerin (IgG1, NCL-emerin; dilution 1:60; Novocastra, Newcastle upon Tyne, U.K).

After washing in PBS secondary antibodies were applied for 1 hour at RT. Secondary antibodies used are FITC-conjugated rabbit anti-mouse Ig (1:100, DAKO, Glostrup, DK), FITC-conjugated goat anti-rabbit Ig (1:50, SBA/ITK, Birmingham, AL, USA), Texas Red

conjugated rabbit anti-mouse Ig (SBA/ITK), and Texas Red conjugated goat anti-rabbit Ig (1:50, SBA/ITK).

After final washings in PBS, slides were mounted in 90 % glycerol, 0.02 M Tris-HCl, pH 8.0, 0.8 % NaN₃ and 2 % 1,4-di-azobicyclo-(2,2,2)-octane (DABCO; Merck, Darmstadt, Germany) containing 0.5 μ g/ml diamidino-2-phenylindole (DAPI, Sigma) or 1 μ g/ml Propidium Iodide (PI) and 0.1 mg/ml RNase for DNA staining.

6.2.4 Actin detection

Cells were cultured on cover slips, fixed and permeabilised as described above, and incubated for 45 minutes with Texas Red-conjugated phalloidin (dilution 1:50; Molecular Probes, Leiden, the Netherlands). To counterstain the nuclei, the cells were incubated for 15 minutes with Syto-13 (1 μ M; Molecular Probes), recognising nucleic acids.

6.2.5 Mechanical compression experiments

Cells were seeded on glass cover slips 18 hours prior to the compression studies at a density low enough to allow compression of a single cell (10,000 cells/cm²). Cellular viability was examined by the addition of 5 μ M PI (absorption 535 nm, emission 617 nm). In order to visualise cell deformation during the experiments, MEF⁺⁺ and MEF⁻⁻ cells were labelled with 7.5 μ M Cell Tracker Green (CTG, Molecular Probes, Leiden, The Netherlands). This green fluorescent dye (absorption 488, emission 520 nm) shows a diffuse staining in all cellular compartments, with often an increased intensity in the nuclei of cells. Alternatively, cells transfected with EGFP-labelled lamins were stained with 10 μ M Cell Tracker Orange (CTO, Molecular Probes, Leiden, The Netherlands). CTO has a maximum absorption at 541 nm and a maximum emission at 565 nm.

Cells were compressed using the loading device, which is described in detail in chapter 2 and section 3.2.2. The experimental procedure and data analysis performed after each compression experiment are described in section 4.2.2 and 4.2.3. In brief, prior to a compression experiment a complete stack of confocal images of the cell was recorded. The height of the cell was calculated as described in section 3.2.4. Then the cell was compressed completely within 15 seconds by moving the indenter with a constant speed (figure 4.1). Force and position of the piezo system were recorded continuously with a sampling frequency of 100 Hz. During the experiment a time series of two-dimensional confocal images of the cell was made.

After data analysis, the force versus axial strain relationship of the cell was obtained. In this way, the mechanical resistance to deformation was quantified. In total 31 MEF⁻⁻, 36 MEF⁺⁺, 17 MEF⁻⁻ control, 13 MEF⁻⁻ rescue A, and 11 MEF⁻⁻ rescue C cells were compressed. For each group, the mean force as a function of the axial strain at axial strain intervals of 5 % was calculated and will be presented as mean \pm standard deviation. A Student's *t*-test with a 0.05 level of significance was used to reveal any significant difference between the mean forces of two cell types at a given strain interval.

6.2.6 Confocal laser scanning microscopy

Immunofluorescence and actin studies

Fluorescent samples were imaged using a Bio-Rad MRC600 confocal microscope (Bio-Rad Laboratories Ltd., Hemel Hempstead, UK) equipped with an air-cooled Argon-Krypton mixed gas laser and mounted onto an Axiophote microscope (Zeiss, Göttingen, Germany), using oil-immersion objectives (40x, NA=1.3 or 63x, NA=1.4). The laser scanning microscope was used in the dual parameter setup, according to the manufacturer's specifications, using dual wavelength excitation at 488 nm and 568 nm. Emission spectra were separated by the standard sets of dichroic mirrors and barrier filters. Optical sections were recorded in the Kalman filtering mode using 4-8 scans for each picture. Z-series were generated by collecting a stack consisting of optical sections using a step size of 0.18 or 0.36 μm in the z-direction.

The Huygens System image restoration software (Scientific Volume Imaging B.V, Hilversum, The Netherlands) was used to improve the effective resolution of some of the confocal images and to reduce background noise.

Compression experiment

Cells within the culture chamber of the loading device were visualised on an inverted microscope (Axiovert 100M, Zeiss, Göttingen, Germany) with confocal laser scanning unit (LSM 510, Zeiss, Göttingen, Germany), using a 40x, NA=0.95, air objective (Plan-Apochromat, Zeiss, Germany). A 25 mW Argon ion laser at 488 nm was used to excite CTG and EGFP, whereas PI and CTO were excited at 543 nm with a 1 mW Helium-Neon laser. To avoid dye saturation, excitation power was set to 1 % (488 nm) and 3 % (543 nm) of maximum laser power. Emission spectra were separated by the standard sets of dichroic mirrors and barrier filters. Prior to a compression experiment a z-series of the cell was collected with a lateral sampling size of $0.3 \times 0.3 \mu\text{m}^2$ and a slice thickness of 0.4 μm . During the compression experiment a time series of two-dimensional confocal images of the cell was made with a lateral sampling size of $0.3 \times 0.3 \mu\text{m}^2$ and a sampling time of 1.7 s per image.

6.3 Results

Decreased mechanical resistance to deformation in LMNA null cells

In total, 36 MEF⁺⁺ cells and 31 MEF⁻⁻ cells were subjected to compression experiments. Confocal recordings of two representative cells from a MEF⁺⁺ (A) and a MEF⁻⁻ (B) cell culture during compression are shown in figure 6.1. From the mean force versus axial strain curves (figure 6.1 C) it is clear that the forces needed to compress the cell were larger for MEF⁺⁺ cells, compared to MEF⁻⁻ cells. This difference was

statistically significant from an axial strain of 27.5 % up to 77.5 % (Student's *t*-test, $p < 0.05$).

In 50 % of the cells a typical decrease in the force during compression could be observed, caused by rupture of the cell membrane. The maximum force at cell membrane bursting is referred to as the bursting force. Two typical curves of both cell types showing this characteristic decrease in the force are shown in figure 6.1 D. After cell membrane rupture, the remaining layer of cell debris was compressed until no further compression was possible. This resulted in a rapid increase of the force. The mean bursting force for MEF⁺⁺ cells ($8.7 \pm 3.0 \mu\text{N}$) was significantly higher (Student's *t*-test, $p < 0.05$) than for MEF⁻⁻ cells ($2.9 \pm 1.9 \mu\text{N}$). The accompanying axial strain at cell membrane rupture was $68.8 \pm 7.5 \%$ for MEF⁺⁺ cells and $62.0 \pm 5.8 \%$ for MEF⁻⁻ cells. Again, this difference was statistically significant (Student's *t*-test, $p < 0.05$).

A-type lamin rescue does not restore mechanical resistance to deformation

In order to investigate whether lamin A or lamin C (-EGFP) was capable of rescuing the MEF⁻⁻ phenotype, MEF⁻⁻ cells were transfected with lamin A or lamin C. To examine whether a correct nuclear structure was restored, other nuclear markers next to lamins were studied.

The localisation of emerin was examined, which is known to be largely dependent on the presence of lamin A and/or lamin C (Sullivan et al., 1999; Gruenbaum et al., 2000). In unaffected MEF⁺⁺ cells, emerin was mainly localised at the nuclear membrane (figure 6.2 A), while in MEF⁻⁻ cells emerin was merely distributed throughout the endoplasmic reticulum (ER) with only a minor portion of emerin present in the nucleus (figure 6.2 B).

Another marker for verification of a correct nuclear membrane organisation is the nuclear pore complex protein nucleoporin p62 (p62). In normal cells, nuclear pores and p62 are evenly distributed at the nuclear membrane surface. In cells without LMNA expression, p62 can be absent from large areas of the nuclear membrane, as seen in figure 6.2 C.

Transient restoration of lamin A or lamin C expression or both could not fully restore the normal architecture of affected nuclei. The typical honeycomb appearance of lamins at the distal poles of the nuclei, as seen in many cases of mutated lamins, became apparent after cotransfection with lamin A-EGFP and lamin C (figure 6.2 D), with a relatively heavy decoration of lamin A and lamin C in these areas. These findings indicate that distorted MEF⁻⁻ nuclei did not revert to their normal phenotype after rescue. Indeed, emerin was still mainly redistributed to the endoplasmic reticulum in lamin A-EGFP rescued cells (figure 6.2 E), similar to cells lacking A-type lamins. Moreover, co-localisation studies of cells rescued with lamin A and stained for p62 expression showed that nuclei remained apparently truncated as a result of the absence of lamins and p62 in affected areas (figure 6.2 F).

The force versus axial strain relationship of MEF⁻⁻ cells transfected with A-type lamins did not show significant differences when compared with untransfected MEF⁻⁻

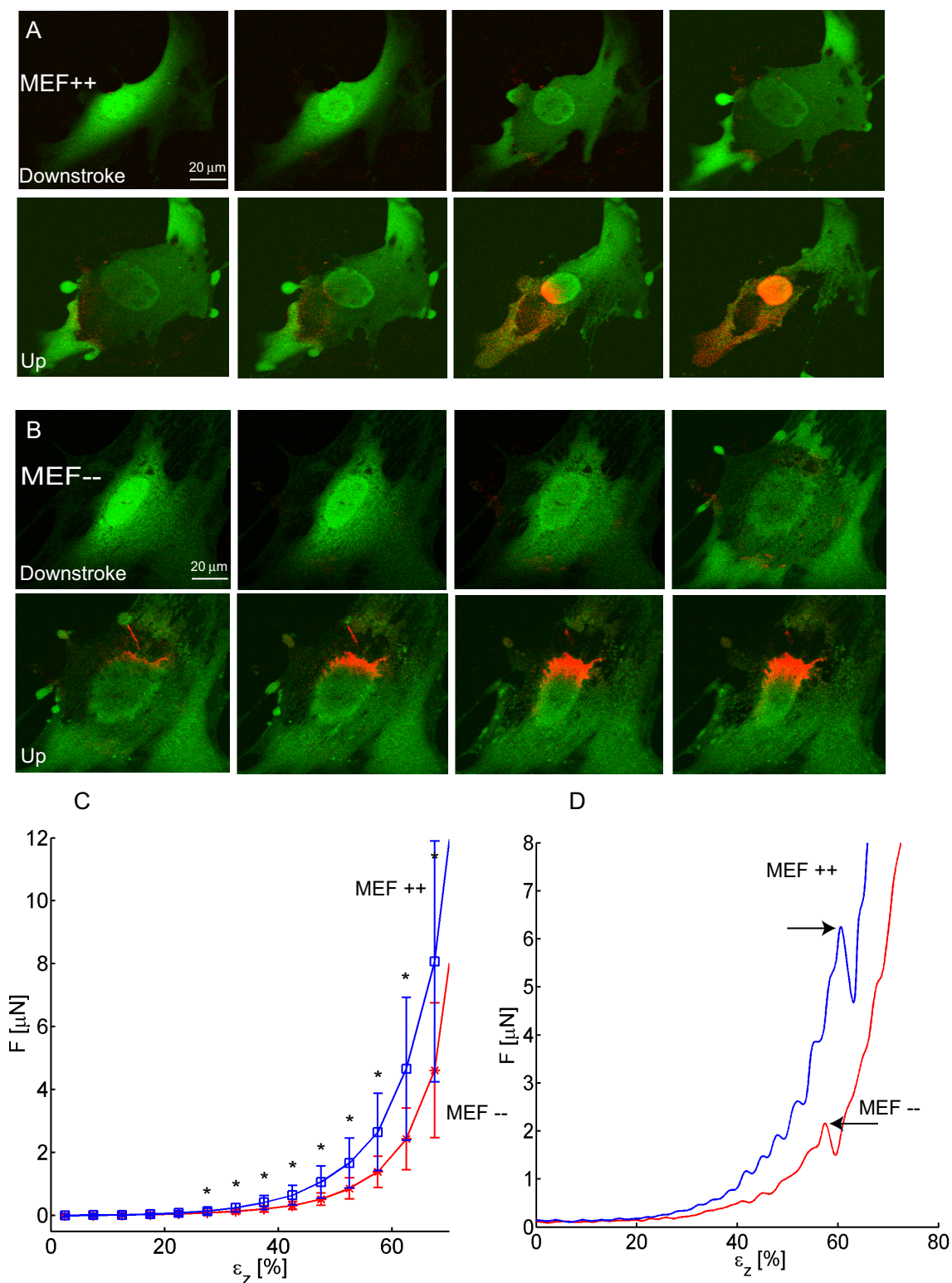


Figure 6.1: A: Confocal images of a characteristic MEF++ cell during increased compression (upper panel) and during relaxation after compression (lower panel). The nucleus of the cell is stained red by the entrance of PI into the cell.

B: Idem for a MEF-- cell.

C: Force versus axial strain curves of MEF++ and MEF-- cells. Asterisks indicate that statistically significant differences between cell populations are observed.

D: Force plots of individual cells showing the determination of bursting force (arrows).

cells (figure 6.2 G). Strikingly, no significant differences in force were observed, when comparing rescued cells with morphologically normal nuclei to cells with aberrantly localised A-type lamins. Apparently, restoring A-type lamin expression was not sufficient to restore the mechanical resistance to deformation.

Differences in nuclear damage resulting from compression

Based upon abnormalities in nuclear morphology seen in MEF^{−−} cells (Sullivan et al., 1999), it was anticipated that local lamina and nuclear membrane aberrations, accompanied by local absence of other nuclear membrane proteins, would cause disruption of nuclei in affected cells. Indeed, most nuclei of MEF^{−−} cells could not endure the complete compression experiment without showing nuclear damage. Figure 6.3 shows the nuclear morphology of MEF⁺⁺ and MEF^{−−} cells after compression, and compares the number of affected nuclei in the two cell types (figure 6.3 I). While the majority of MEF⁺⁺ nuclei remained largely intact throughout the complete compression experiment (figure 6.3 A, B), most MEF^{−−} nuclei became severely damaged, resulting in chromatin protruding into the cytoplasm as seen by the propidium iodide (PI) staining (figure 6.3 C, D).

A-type lamin rescue does partially restore nuclear integrity

Rescue with either lamin A-EGFP or lamin C-EGFP had a positive impact on the integrity of the nucleus during compression. MEF^{−−} cells showing a morphologically intact lamina after transfection, generally remained largely intact after compression. Strikingly, in cells with an irregular lamina after rescue, nuclear areas with a relatively strong A-type lamin expression would not burst, while simultaneously, the nuclear areas with less A-type lamin expression were still weak and did burst upon indentation (figure 6.3 E-H). Comparison of nuclear damage among MEF^{−−}, MEF⁺⁺ and A-type lamin rescue cells shows that indeed nuclear coherence was increased after rescue, resulting in fewer cells with prominent nuclear damage after compression (figure 6.3 I). Note however, that the mechanical resistance to deformation was not restored in these cells (figure 6.2 G).

MEF⁺⁺ nuclei deform anisotropically, MEF^{−−} nuclei isotropically

To explain the apparent discrepancy between the restoration of nuclear coherence but simultaneous lack of restoration of mechanical resistance to deformation, the deformation behaviour of nuclei during deformation was more closely examined. In chapters 3 and 4 it was already shown that cultured cells, which grow stretched out into a specific direction, showed nuclear deformation mainly perpendicular to this growth direction.

This anisotropic deformation could be confirmed in nuclei of MEF⁺⁺ cells. Most nuclei in cells with a preferred orientation deformed anisotropically (figure 6.4 A). However, careful inspection of the deformation direction of MEF^{−−} nuclei did not

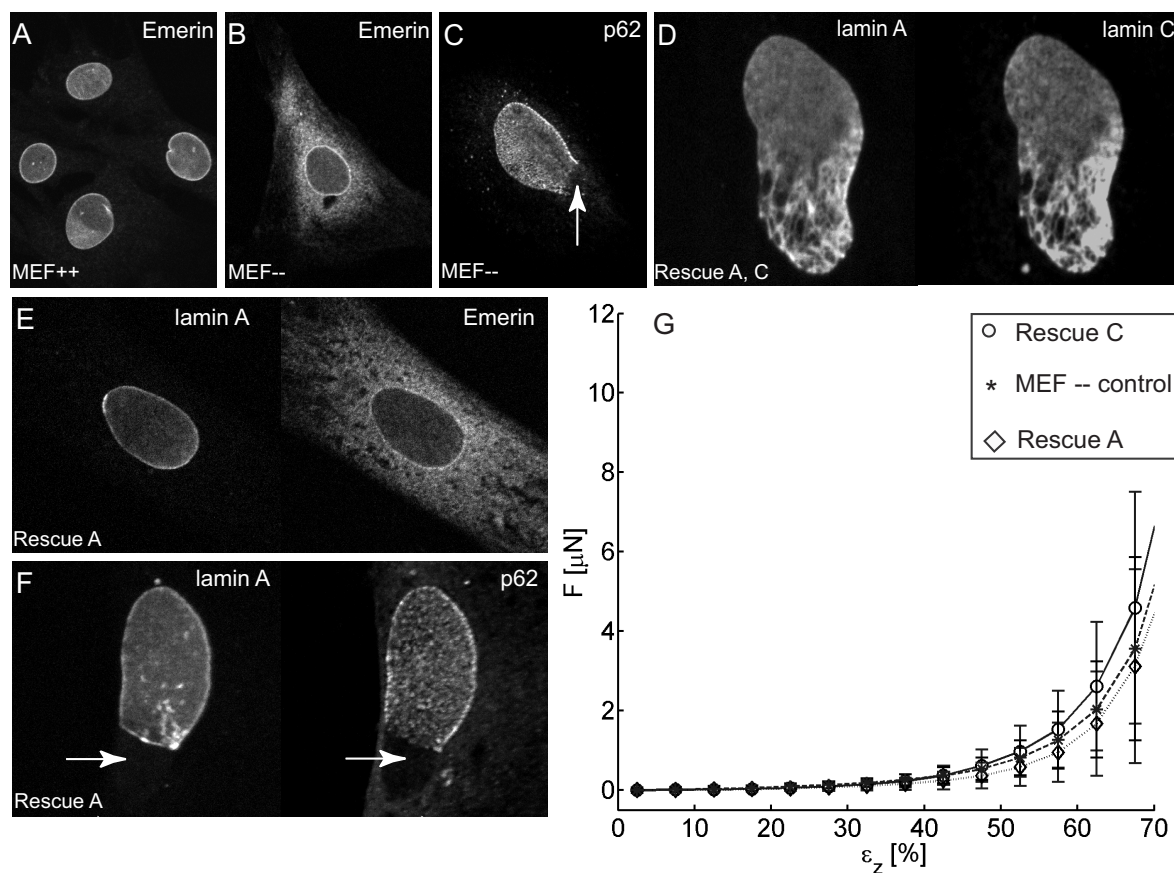


Figure 6.2: A-F: (Immuno-)fluorescence patterns of MEF++ cells (A), MEF-- cells (B,C), cells rescued with lamin A-EGFP and lamin C in pcDNA3 (D), or cells rescued with lamin A-EGFP (E,F).

A: Emerin immunoreactivity is localised in the nuclear membrane of MEF++ cells.

B: Emerin immunoreactivity is mainly localised in the ER of MEF-- cells.

C: p62 is unevenly distributed in MEF-- cells, being absent at the lower part of the nucleus (arrow).

D: Cell cotransfected with lamin A-EGFP (left) and lamin C cDNA (right, visualised with the lamin C antibody). Although a lamina is restored in the largest part of the nucleus, lamins are still disorganised in the lower part of the nucleus.

E: Cell transfected with lamin A-EGFP. While lamin A-EGFP is present throughout the nuclear membrane (left), emerlin is not restored to the nuclear membrane and distributed throughout the ER (right).

F: Cell, in which the nuclear lamina is partially restored with lamin A (left). Nuclear pore complexes (visualised by the p62 antibody) are still confined to the lamin-containing part of the nuclear membrane, and absent from areas devoid of lamin A (right, arrow).

G: Force versus axial strain curves of MEF-- cells and cells transfected with either lamin A or lamin C (-EGFP). No significant differences between different cell types are seen.

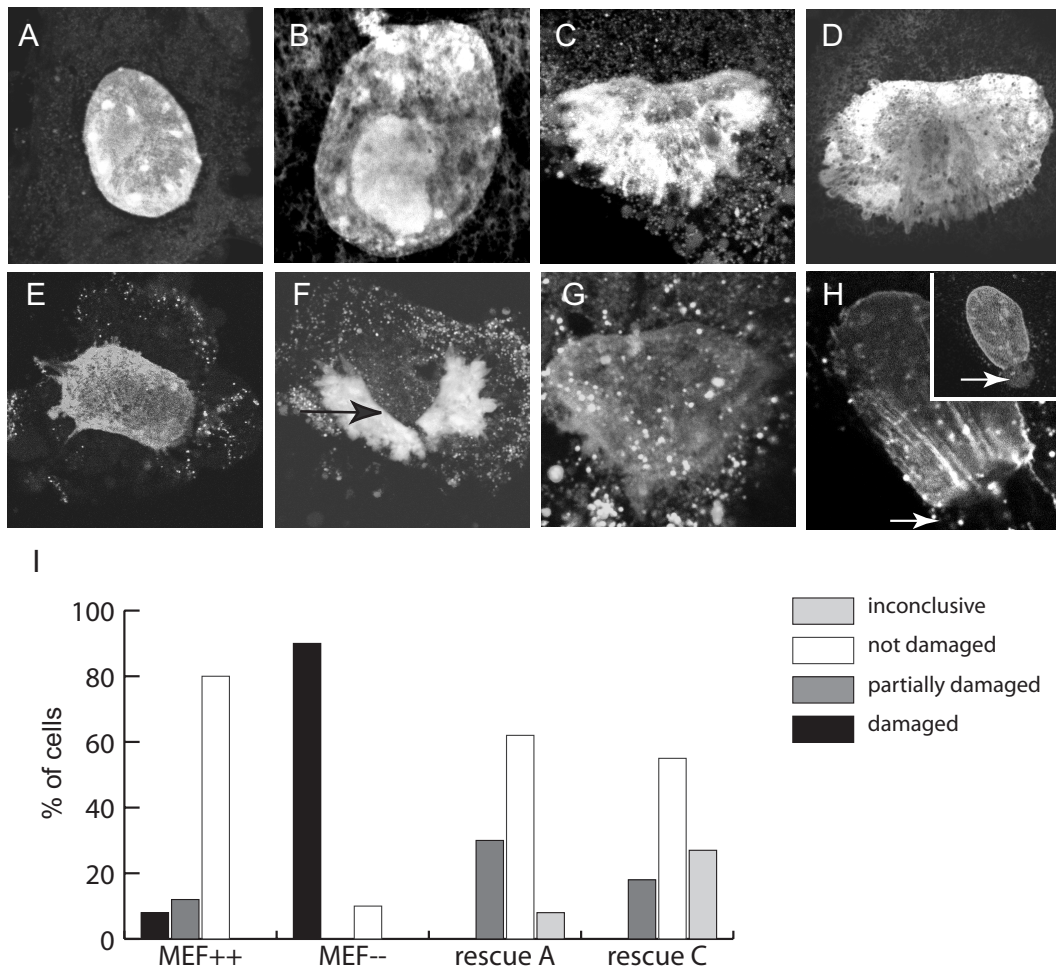


Figure 6.3: Nuclear damage during compression visualised with CTG and PI (A-D) or with CTO and PI (E-H). In all samples the prominent fluorescent signal in the central region of the cell results from PI fluorescence.

A,B: Damage seen in MEF++ cells. After compression, the nuclear shape of most nuclei remained intact, with chromatin still located in a sharply delineated nuclear compartment.

C,D: Most nuclei of MEF-- cells burst wide open after compression, with chromatin protruding into the cytoplasm as irregular lobules.

E,F: Depending on the amount and organisation of transfected lamins, rescued nuclei remained intact, or show only local disruption of the nucleus. Nuclei transfected with lamin A-EGFP showed no disruption in many nuclei, or partial disruption at areas with so-called honeycomb lamin patterns (E), and less disruption in areas with high levels of lamin A (F, arrow).

G,H: Similar observations were made for lamin C-EGFP rescued cells with a relatively good preservation of nuclear shape in areas with high levels of lamin C and disruption of areas lacking lamin C (H and insert, arrow). Inset in (H) shows lamin C fluorescence before compression.

I: Comparison of nuclear damage between MEF++ cells, MEF-- cells and A-type lamin rescued cells.

reveal this correlation (figure 6.4 B). During indentation, the nuclei of these cells often deformed equally in all directions (isotropic), without any correlation with the initial cell orientation. The same holds true for MEF^{-/-} cells, in which lamin A or lamin C was restored by transfection. These data are summarised in figure 6.4 C.

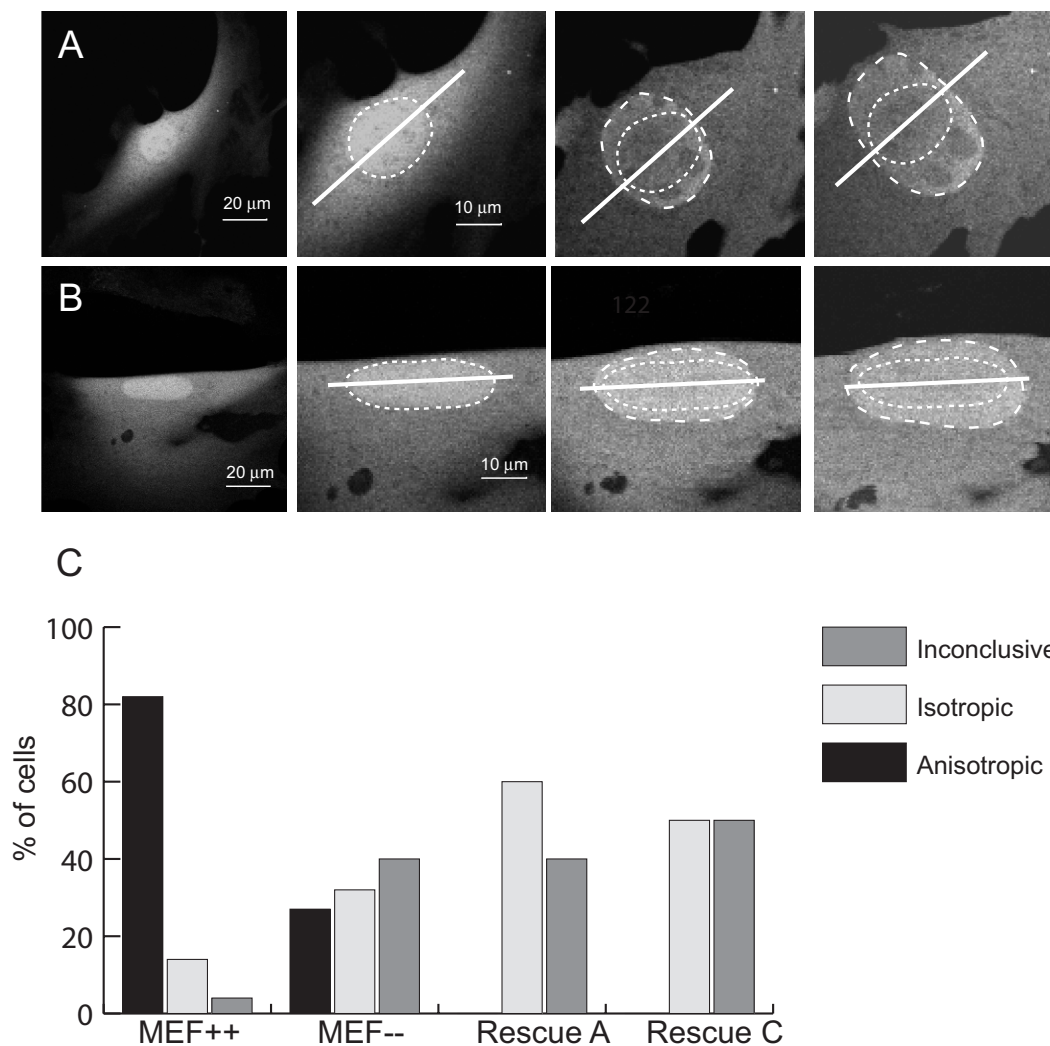


Figure 6.4: Determination of direction of deformation of nuclei during compression. A: MEF⁺⁺ cell showing anisotropic deformation (hatched ovals) compared to the long axis (straight line). B: MEF^{-/-} cell showing isotropic deformation. C: Comparison of cells with anisotropic deformation in MEF⁺⁺ cells, MEF^{-/-} cells, and A-type lamin rescued cells. MEF⁺⁺ cells have the highest amount of cells with anisotropic deformation, which is not restored by A-type lamin rescue.

Decreased mechanical resistance to deformation and lack of anisotropic nuclear deformation could be caused by abnormal actin organisation

Direction of nuclear deformation is most likely determined by extranuclear factors, involved in maintaining cellular shape and orientation. Since actin proteins are known to handle these aspects of the cell, the three-dimensional composition of actin filaments in MEF^{-/-} and MEF^{+/+} cells was examined. Representative cells from these populations are shown in figure 6.5. At the peripheral regions of these cells, no obvious difference in the organisation of stress fibres was seen. However, in areas close to the nucleus the actin stress fibres seemed to be disrupted in MEF^{-/-} cells and not in MEF^{+/+} cells (compare figures 6.5 A and B). In these areas, dots were observed consisting of either unpolymerised actin, or not correctly polymerised actin (figure 6.5 B, arrow).

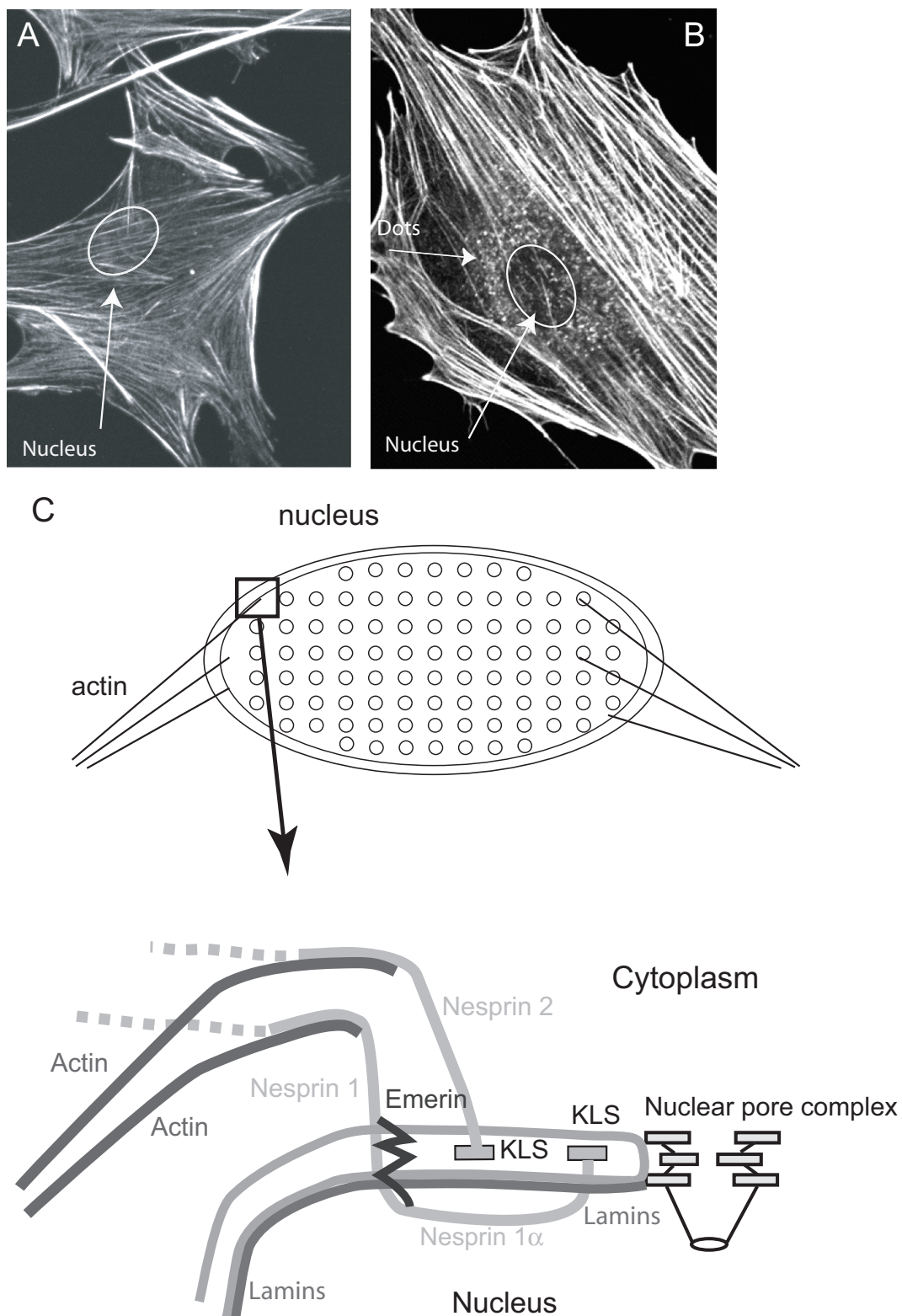


Figure 6.5: A, B: Actin filaments in a MEF++ (A) and a MEF-- cell (B). Note the truncated actin filaments in the regions surrounding the nucleus of a MEF-- cell, while an intact actin staining pattern is seen in the MEF++ cell. C: Model of key proteins, involved in maintaining mechanical and structural integrity in cells.

6.4 Discussion

The nature of several of the diseases, associated with A-type lamin mutations, points to a correlation between cellular and/or nuclear weakness, and the cellular loss in pressure-sensitive tissues, such as (heart) muscle. Emery Dreifuss muscle dystrophy, limb girdle dystrophy, and dilated cardiomyopathy are all characterised by the loss of muscle tissue, presumably caused by abnormally high levels of cellular death in these tissues. Next to stretching forces, muscle cell nuclei also encounter heavy local compression forces during muscle activity. Since muscle strength increases with age, it is not surprising that these diseases develop with age and with increasing muscle strength of the affected patients. In general, symptoms only develop after muscle cells have reached their full strength, i.e. starting at early adulthood.

B-type lamins are crucial for cellular survival, and cells depleted of B-type lamins will die via apoptosis (Harborth et al., 2001). Organisms lacking A-type lamin expression, including LMNA null mice (Sullivan et al., 1999) or humans expressing no functional lamins (Muchir et al., 2003), die shortly after birth. However, no correlation between lamin A-type mutations and increased apoptosis has been demonstrated. This would imply that these muscle cells are not prone to premature cell death but rather die as a result of a sudden cellular insult due to for instance heavy labour of muscle tissues. A possible explanation would be the loss of cellular stiffness due to A-type lamin mutations. Based on the localisation of the nuclear lamina it has already been postulated long ago that lamins play a prominent role in maintaining nuclear integrity. Cellular extraction studies in cell lines harbouring A-type lamin mutations indicate that cells with these mutations display increased nuclear fragility upon extraction. However, direct evidence of nuclear weakness as a result of A-type lamins abnormalities is still rather marginal.

Therefore, the mechanical resistance to deformation in normal fibroblasts and fibroblasts completely lacking LMNA gene expression was measured. Using a newly developed cell loading device (Peeters et al., 2003), a clear, statistically significant, higher resistance against indentation in MEF⁺⁺ cells was found, when compared to MEF⁻⁻ cells. Moreover, the force needed to cause cellular bursting was significantly higher in MEF⁺⁺ cells.

Simultaneous confocal imaging allowed to extend on these findings and to more closely examine the deformation of individual cells and their nuclei. The first aspect to note was the nuclear damage, resulting from compression. While normal nuclei morphologically still looked intact after compression, the LMNA null nuclei in most cases had burst completely, leaving after compression only a disturbed nuclear mass, spreading into the cytoplasm. This loss of nuclear integrity could be largely overcome by transient transfection of A-type lamins into these cells. However, it was not possible to fully restore the mechanical resistance to deformation in the affected cells. In order to find an explanation for this phenomenon, the protein composition of these rescued nuclei was more closely investigated. It became clear that only the presence of lamin proteins was restored but not the correct localisation of nucleoporin p62 and emerin.

In this way, although unsuccessful, this partial rescue pointed towards a very

intriguing aspect of nuclear and cellular stiffness, i.e. that cellular strength could result from an interplay of cytoskeletal and nucleoskeletal elements. This can only be achieved if all components are correctly assembled.

A strong indication that the partially rescued cells indeed lacked a correct connection between nuclear proteins and cytoskeletal structures came from the observations on the direction of deformation of compressed nuclei. As seen in chapter 3 and 4, normal nuclei exhibit anisotropic deformation during compression: if cells have a preferred direction of orientation, along its long axis, the nuclei will deform in a direction perpendicular to this axis. Indeed, most nuclei of normal cells showed this type of deformation during compression. However, both MEF^{−−} cells and A-type lamin rescued cells did not show this anisotropic deformation. Apparently, the interconnection between nuclear components such as lamins and the cytoskeleton, was still lacking in these cells. How this connection between nuclear proteins and cytoskeletal structures is maintained is not yet fully understood.

A key role is most likely reserved for the recently discovered giant proteins called nesprins. Of these, nesprin 1 α is localised in the intranuclear compartment and interacts with A-type lamins as well as emerin at the nuclear envelope (Mislow et al., 2002). Binding of nesprin 1 α to these molecules occurs at the most carboxy-terminal part of nesprin to A-type lamins and at their amino-terminal part to emerin. A more recent study indicates that nesprin 1 α is the carboxy-terminal part of a much larger protein, nesprin 1, which is not only present in the nucleus, but also spans large areas of the cytoplasm (Zhang et al., 2002). Interestingly, the amino-terminal part of this large protein binds prominently to actin (Zhang et al., 2002). A second member of the nesprin family, called NUANCE (Zhen et al., 2002) or nesprin-2 (Zhang et al., 2001, 2002), shows a similar topology, i.e. binding to actin in the amino-terminal region of the molecule and anchorage to the nuclear membrane via the common KLS motif (Zhang et al., 2002). A model of the connection between lamins, emerin, nesprins, and actin is shown in figure 6.5 C.

In cells lacking A-type lamin expression the proper binding of nesprin 1 α is disturbed. Relocalisation of nesprin 1 α from the nucleus to the cytoplasm occurs in human fibroblasts lacking expression of the LMNA gene. The correct localisation of this protein is restored if these cells are rescued with either lamin A or lamin C (Muchir et al., 2003), provided that the correct localisation of other nuclear proteins is restored as well. While it is not yet shown that nesprin contributes to mechanical stiffness, it is well known that actin is a major component in determining cellular stiffness (Petersen et al., 1982; Sato et al., 1990; Janmey et al., 1991).

Therefore, the three-dimensional organisation of actin in MEF⁺⁺ and MEF^{−−} cells was examined, using confocal microscopy and image restoration. Careful examination of actin architecture in affected cells did reveal abnormalities in actin filament formation, not seen in control cells. These abnormalities in actin filaments, especially present in perinuclear areas of affected cells, could explain why the absence or abnormality of a single group of nuclear proteins (A-type lamins) could cause total cellular weakness. This weakness could be mediated by the inability of actin to form correct stress fibres, if nesprins cannot bind to lamins and/or emerin. Clearly more research should solve

the exact (loss of) interaction between these cellular components. This hypothesis is supported by the finding that similar muscle dystrophic diseases are caused by inappropriate attachment of actin to the periphery of the cell. For instance limb girdle muscular dystrophy type 1A is associated with the actin-binding protein myotilin (Schroder et al., 2003), sporadic dilated cardiomyopathies can be associated with dystrophin gene mutations (Feng et al., 2002), and actinin mutations can be associated with congenital muscular dystrophy (North and Beggs, 1996).

In summary, it was demonstrated that fibroblast cells lacking A-type lamin expression have a significantly reduced mechanical resistance to deformation and reduced bursting force, when compared to normal fibroblasts. Next to these findings, aberrant nuclear deformation during compression was observed, pointing towards the lack of association of the nucleus with cytoskeletal proteins, including actin. Loss of lamin-actin interaction (via emerin and nesprins) can result in disorganisation of the actin network around the nucleus, and explain the arising of laminopathies associated with muscle diseases.

Chapter 7

General discussion

7.1 Introductory remarks

In this thesis, the biomechanics of single attached cells was examined with reference to two different clinical problems, in which mechanical factors and especially the biomechanics of cells play a major role; pressure ulcers and laminopathies.

With reference to pressure ulcers, a series of experiments was performed to examine how C2C12 myoblasts deform under compression. Furthermore, the load-bearing properties and the viscoelastic properties of these cells were quantified.

With reference to laminopathies, a test hypothesis was established that abnormalities in nuclear architecture cause mechanical weakness in cells. This involved comparing the load-bearing properties and the deformation behaviour of wild-type and LMNA knockout mouse fibroblasts.

The present chapter discusses the developed methods and techniques, the associated results, and their implications and recommendations for future research on pressure ulcers, laminopathies, as well as cell biomechanics in general. Finally, the overall conclusions that can be drawn from the work are summarised.

7.2 Loading device

The device to compress single attached cells was presented in chapter 2 . A schematic representation and photograph of the device are shown in figure 3.1. The complete experimental system was controlled by a custom-made software program written in LabVIEW (National Instruments, USA). An overview of the data-acquisition system is shown in figure 2.2.

The use of confocal microscopy allowed the quantification of cell deformation in the lateral and axial plane as a function of time. Other experimental techniques to directly load single cells used conventional brightfield microscopy and, as a consequence, are required to make assumptions regarding the geometry of the cell (Zhang et al., 1992; Thoumine and Ott, 1999; Guilak et al., 2002). The present device could be mounted on any microscopic system.

In contrast to other loading techniques, no video images were needed to measure the position of the piezo-actuators and the forces as a result of compression. For example, video images were used in studies employing micropipette aspiration to measure the extension of the surface of the cell into the micropipette (Hochmuth, 2000) and microplates to measure the deflection of the flexible microplate (Thoumine and Ott, 1999). This approach, however, would limit the temporal and spatial resolution of the technique.

Although the drift of the force transducer was large (up to 10 μ N within 24 hours), the sensitivity was not affected by this drift because the major proportion was related to the offset and not the gain of the transducer. The drift could be neglected in the experiments conducted in chapters 4 and 6, because each experiment was completed within 30 seconds. However, for the dynamic experiments performed in chapter 5,

the force signal was processed using a band-pass filter, to remove the low and high frequency components of the signal. As drift is a low frequency signal, this component was removed from the post-filtered signal. If the mechanical properties of cells under compression were to be examined over a period of several hours, the force transducer would have to be set to zero and a small load superimposed on the already existing load. Although absolute values of reaction forces can not be measured, changes in the mechanical properties during long-term compression can be evaluated.

A further advantage of the present device is that it examines the global mechanical properties of attached cells. Micropipette aspiration of cells also reveals the global mechanical properties, but is only applied to suspended cells. Another global measuring technique, developed by Thoumine et al. (1999), can be applied to cells, which are allowed to spread for 1 hour. Using this device, no differences in the elastic modulus between spread and round endothelial cells could be distinguished (Caille et al., 2002). It was concluded that the reorganisation of the cytoskeleton within endothelial cells was insufficient after this short incubation time. Longer incubation times caused migration of the cell towards the edge of the microplate. In the present study, C2C12 cells and fibroblasts were allowed to spread for at least 16 hours.

Perhaps the most important advantage of the device compared to existing devices, is the arrangement made to create optimal culture conditions during compression. Within the cell culture chamber of the device, the environmental conditions are similar to those of a regular CO₂ incubator. Cells remained viable for at least 24 hours, although it could be predicted that cells will remain viable for even longer periods of time. The optimised culture conditions make it possible to monitor morphological and mechanical property changes of the cell over time under physiological conditions.

7.3 Cell deformation

Confocal laser scanning microscopy was used to visualise the cell during compression experiments. Either three-dimensional images (chapter 3) or two-dimensional images were obtained (chapters 4 to 6) during these experiments, depending on the time provided to acquire the images.

In chapter 4, cells were subjected to 0.5 μm increments of axial displacement. After each increment, a three-dimensional image of the deformed cell was recorded. Several geometric parameters were estimated. For example, with applied deformation, there was a significant increase in cell width, cross-sectional area and surface area of the cell (figure 3.7). The apparent increase of surface area may be artefactual, as the folds and ruffles in the cell membrane cannot be resolved with confocal microscopy (Lee et al., 2000). As the maximum increase in surface area strain prior to rupture has been reported to be only approximately 3 % (Evans et al., 1976), it is likely that cell deformation induces the folds to unravel. However, it remains to be elucidated if and how the cell membrane in myoblasts is folded. Electron microscopy could resolve the ultrastructural detail at the cell surface, as previously demonstrated with chondrocytes (Lee et al., 2000).

Estimation of the mean volume of the cell during compression indicated a small increase with applied axial strain. However, the Student's *t*-test showed that this increase was not significant after deconvolution (figure 3.7). Furthermore, it should be noted that the estimated volume was affected by the limited axial resolution of the confocal microscope and axial distortion, because of a mismatch in refractive indices of the objective immersion medium (air) and the cell. The use of deconvolution compensated to a certain extent for this limited axial resolution (Kempen et al., 1997; Dumas et al., 2003), thereby reducing the overestimated height and volume of the cell. Typically, a 2 to 4 fold improvement in axial resolution can be achieved using deconvolution (Kano et al., 1996). A linear correction factor was used to compensate for the axial distortion as a result of the mismatch in refractive indices (Hell et al., 1993). This factor was calculated by dividing the refractive index of the cell by the refractive index of the objective medium. However, the refractive index of the cell could alter as a result of compression, thereby causing an incorrect estimation of the height and volume of the cell. Future research would be required to reveal whether the refractive index of the cell changes during compression.

An intriguing finding when observing the deformation of cells under compression was the anisotropic deformation: if a cell had a preferred direction of orientation, along its long axis, it deformed in a direction perpendicular to this axis. All C2C12 cells had this preferred orientation and deformed anisotropically, which was reflected by an increase of the shape factor κ_{21} (figure 3.8). In addition, fibroblasts, as examined in chapter 6, with a preferred orientation also deformed anisotropically (figure 7.1 F-H). It is interesting to note, however, that fibroblasts with no preferred orientation deformed isotropically (figure 7.1 B-D). In chapter 3, this anisotropic deformation was explained by considering the actin filaments throughout the cell, which were predominantly orientated along the long axis of the cell (figures 3.9 A and 7.1 E). In contrast, actin filaments were not orientated in cells with no preferred orientation (figure 7.1 A). Although the orientated actin filaments might well cause this anisotropic deformation, confirmation of this theory should be obtained in future compression experiments on cells with and without actin filaments.

The nuclei of C2C12 (figure 4.3) and MEF++ cells (figure 6.4) with a preferred direction of orientation also deformed anisotropically during compression. However, both MEF-- cells and A-type lamin rescued cells did not show this anisotropic deformation (figure 6.4). Apparently, the interconnection between nuclear components, such as lamins, and the cytoskeleton, was absent in these cells. Again, the involvement of actin filaments was considered. Indeed, careful examination of actin architecture in these cells did reveal abnormalities in actin filament formation in perinuclear areas, not seen in normal cells. In these areas, dots were observed consisting of either unpolymerised actin, or not correctly polymerised actin (figure 6.5 B, arrow).

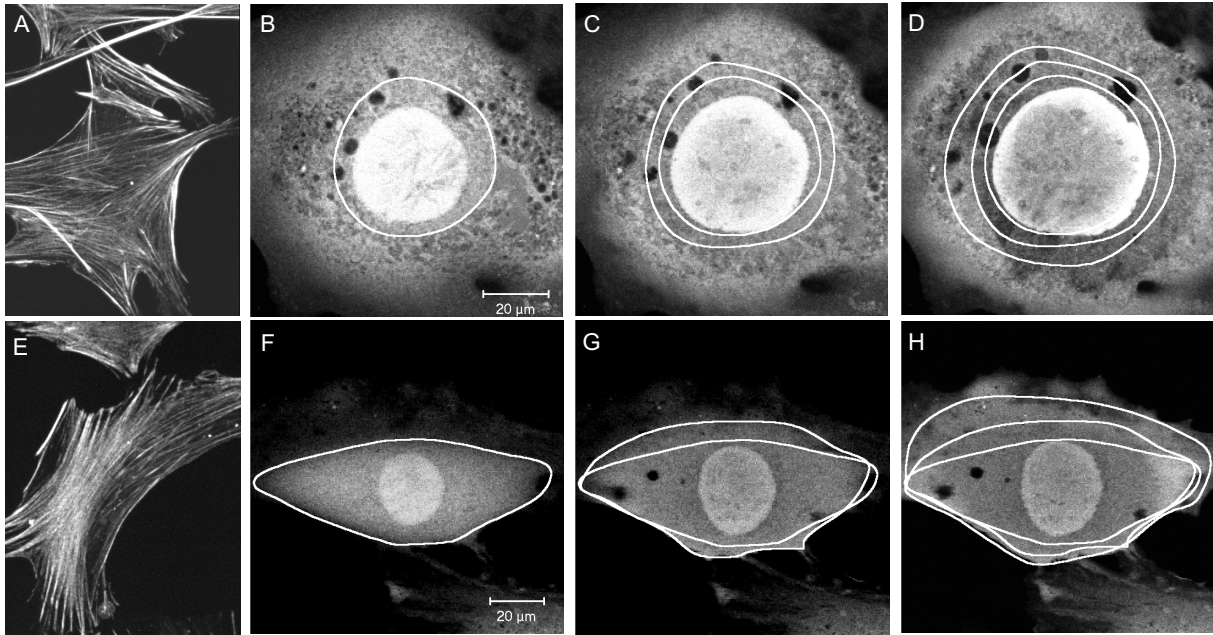


Figure 7.1: A: Actin cytoskeleton in a MEF++ cell without a preferred orientation. B-D: Deformation of a MEF ++ cell without a preferred orientation is isotropic. White circles track cell deformation through its vacuoles. E: Actin cytoskeleton in a MEF++ cell with a preferred orientation. F-H: Deformation of a MEF ++ cell with a preferred orientation is anisotropic. White ovals indicate the contour of the cell during compression.

7.4 Mechanical characterisation

7.4.1 Load-bearing properties

The load-bearing properties of single attached cells, as reflected in the force versus axial strain relationship and the bursting force, were determined by complete compression of the cell within a period of 15 seconds. These experiments were comparable to those performed by Zhang et al. (1991) on non-attached hybridoma cells. The mean bursting force of C2C12 cells ($8.7 \pm 2.5 \mu\text{N}$) and MEF++ cells ($8.7 \pm 3.0 \mu\text{N}$) were higher than the bursting force of non-attached hybridoma cells (approximately $3 \mu\text{N}$). These differences might be a result of the various cell types examined or, more probably, a direct result of the cell attachment in the present study with the associated involvement of the cytoskeleton and its structural organisation (Thoumine and Carodoso, 1999).

The experiments in chapter 6 showed the sensitivity of the loading device to discriminate between healthy and diseased cells through comparison of the load-bearing properties. From the mean force versus axial strain curves (figure 6.1 C) it was clear that the forces needed to compress the cell were larger for MEF ++ cells, compared to

MEF-- cells. Furthermore, the mean bursting force for MEF++ cells ($8.7 \pm 3.0 \mu\text{N}$) was significantly higher than for MEF-- cells ($2.9 \pm 1.9 \mu\text{N}$).

The Young's modulus of attached C2C12 cells was estimated by finite element simulations using an axisymmetric representation of the cell geometry and a Neo-Hookean constitutive model. The Neo-Hookean material model has also been successfully used to describe similar compression experiments on endothelial cells (Caille et al., 2002). Although an axisymmetric shape does not appear to be appropriate for a C2C12 cell (figure 3.5), the height and the base area of the axisymmetric finite element mesh were equal to those of the actual cell. Therefore, this assumption was considered to have a minor effect on the estimated Young's modulus.

The model, however, was unable to account for the anisotropic deformation of the cells, which is clearly a direct result of assuming an axisymmetric cell shape and isotropic material behaviour. Therefore, an improved finite element model is currently being developed, which incorporates a three-dimensional representation of the cell and an anisotropic material model describing the influence of actin filaments on the deformation behaviour of cells under compression. To develop and validate this model, additional experiments should be performed on cells, again in the presence or absence of actin filaments. Furthermore, transfection of these cells with fluorescently labelled actin will provide additional information on the deformation of these filaments during compression. The nucleus should also be introduced into this improved model to describe its anisotropic deformation in the cell during compression. To capture the mechanical properties of the nucleus, experiments could be performed on isolated nuclei (Guilak et al., 2000; Caille et al., 2002).

7.4.2 Viscoelastic properties

The viscoelastic behaviour of C2C12 cells was investigated in chapter 5. Series of dynamic experiments were performed over two frequency decades (0.1-10 Hz) and at different axial strains ($\sim 10 - 40 \%$). Viscoelasticity was reflected by the apparent hysteresis of the loading-unloading curves and the frequency-dependent response at a given amplitude (figure 5.4). These characteristics were in general agreement with other studies investigating cellular viscoelasticity (Thoumine and Ott, 1997b; Alcaraz et al., 2003; Petersen et al., 1982). Furthermore, the force versus axial strain curves reflected the non-linear behaviour of the cell (figure 5.4). This non-linear behaviour became more pronounced at high axial strains ($> 20 \%$) and high frequencies.

The experimental data could be described with a non-linear viscoelastic model, based on the standard linear solid model, which is often used to describe dynamic, relaxation, and creep experiments on cells (table 5.3). A standard linear solid model consists of a linear spring in parallel with a Maxwell element. In the non-linear viscoelastic model, the linear spring of the Maxwell element was replaced by a non-linear spring. The contribution of this spring was considerable at high frequencies, when the dashpot is a rather stiff structure. At low frequencies, the contribution of the non-linear spring

became less evident. Besides this non-linear spring, a geometric non-linearity was introduced by taking into account the increasing contact area between indenter and the cell with applied axial strain. The use of this non-linear model permitted the description of the viscoelastic behaviour over a wide range of applied strains and frequencies using only a single set of material parameters.

The geometric non-linearity introduced in this model was just a first approximation of the increasing contact area during compression. Therefore, a finite element model comparable to the one described in chapter 4 is currently being developed to describe this increasing contact area more accurately.

7.5 Clinical applications

7.5.1 Pressure ulcers

Understanding the aetiology of pressure ulcers may contribute to a decrease in the high prevalence figures. The work described in chapters 3, 4, and 5 of this thesis is part of a research programme at the Eindhoven University of Technology, which aims at the understanding of the basic pathways whereby mechanical loading leads to soft tissue breakdown in the form of pressure ulcers. Therefore, a hierarchical approach is adopted, incorporating experimental and numerical models at different length scales and levels of complexity (Bouten et al., 2003a,b). Experimental models include a single cell model, as presented in this thesis, engineered tissue models (Bouten et al., 2001; Breuls et al., 2003b), and an animal model (Bosboom et al., 2001, 2003). Numerical models include a single cell model (chapter 4), tissue models (Bosboom, 2001; Breuls et al., 2003c), and a model of a supported human buttock contact (Oomens et al., 2003).

The elastic and viscoelastic properties of the muscle cells as characterised in this thesis will be used as an input for the multiscale computer model as described in Breuls et al. (2003c). This will permit prediction of the internal microscopic mechanical environment from global, macroscopic loading conditions, such as interface pressures. The next question is how these internal conditions eventually lead to cellular damage and subsequent tissue breakdown. In earlier studies it has been hypothesised that cellular damage is caused by sustained cell deformation (Bosboom, 2001; Bouten et al., 2001; Breuls et al., 2003b). These studies, investigating the relationship between deformation and cellular damage in three-dimensional *in vitro* muscle models, indicated that cell damage increases with both magnitude and duration of compression.

A study on cell damage evolution as a result of sustained compression at the single cell level should be performed in the future to complement the studies using *in vitro* muscle models. This would allow investigating the deformation-induced cell damage with time, independent of other factors such as neighbouring cells, the extracellular matrix, and three-dimensional tissue configuration. The developed loading device with its controlled environment within the cell chamber is particularly suitable to perform such long-term experiments. In this thesis, the deformation of single cells under compression was

quantified using various geometric quantities and the shape factor.

In future experiments, a relationship should be established between the duration of cell compression, the resulting cell deformation in terms of changes of the geometric quantities and/or shape factor, and the degree of cell damage. Cell damage should then be defined as reversible or irreversible damage or cell death. Towards clinical practice, it would be useful to find a biochemical marker for early reversible cell damage. This marker would provide thresholds for cell damage and may even lead to the development of a screening tool in the form of a biosensor. Irreversible damage occurs when cells are in the stage of apoptosis, which may be defined as cell suicide or programmed cell death. Apoptosis occurs when a cell is no longer needed or has become damaged (Knight et al., 1999; Sandri and Carraro, 1999). Cell death is the ultimate result of apoptosis or necrosis. Necrotic cells die from damage or poisoning and typically swell and burst, releasing their contents into the extracellular matrix (Alberts et al., 1994). In fact, cell death can be easily determined using a fluorescent stain, such as Propidium Iodide, as used in all experimental studies of this thesis. Although Propidium Iodide does not discriminate between apoptotic or necrotic cell death, cell death in these experiments was presumably the result of necrosis because apoptosis typically takes several hours to cause cell death. Taken together, identifying the specific stages of damage would provide an insight into how cell deformation leads to cell damage.

In a pilot study, a few experiments were conducted in which the cell was compressed at an axial deformation of approximately 30 % for at least 12 hours. It was observed how the cell deformed and behaved during this time period, by recording confocal images at time intervals of 10 minutes. The cell was stained with CTG and PI, to observe cellular deformations and possible cell death. However, the cell moved towards the edge of the indenter, probably to avoid the compressive deformation (figure 7.2). Thus, future experiments investigating cell deformation and damage, should incorporate a means to immobilise a single cell. This could be achieved by coating the cover glass of the culture chamber with specific cell adhesive substrates, such as gelatin (Doktycz et al., 2003).

The influence of other factors affecting cell damage, related to clinically known risk factors, could also be relatively easily investigated by the loading device. For example, the contributions of temperature, nutrition, mechanical stimulation, and electric stimulation to cell damage could all be examined. An understanding of the influence of these risk factors on cell damage, could be of use to identify patients at specific risk and, potentially, to enhance the resistance of individuals to develop pressure ulcers.

Another way to identify patients at risk, is to determine the genetic or developmental predisposition to cell damage of individual patients. It would be interesting to investigate whether single cells taken from patients which suffer from pressure ulcers, would indeed be mechanically more vulnerable than cells taken from healthy patients without pressure ulcers.

As a final remark, it must be emphasised that the cells investigated in the present work are mouse skeletal myoblasts and not fully differentiated skeletal muscle cells. Unfortunately, fully differentiated muscle cells will only develop in a confluent

monolayer, which makes it almost impossible to compress a single cell without making contact with a neighboring cell. Compressing single skeletal muscle cells will require the isolation of one cell from its environment. A method to achieve this can be laser microdissection and pressure catapulting (Emmert-Buck et al., 1996; Sirivatanauksorn et al., 2002). With this technique, a single cell can be isolated from a monolayer of confluent cells, and subsequently catapulted into a collecting device.

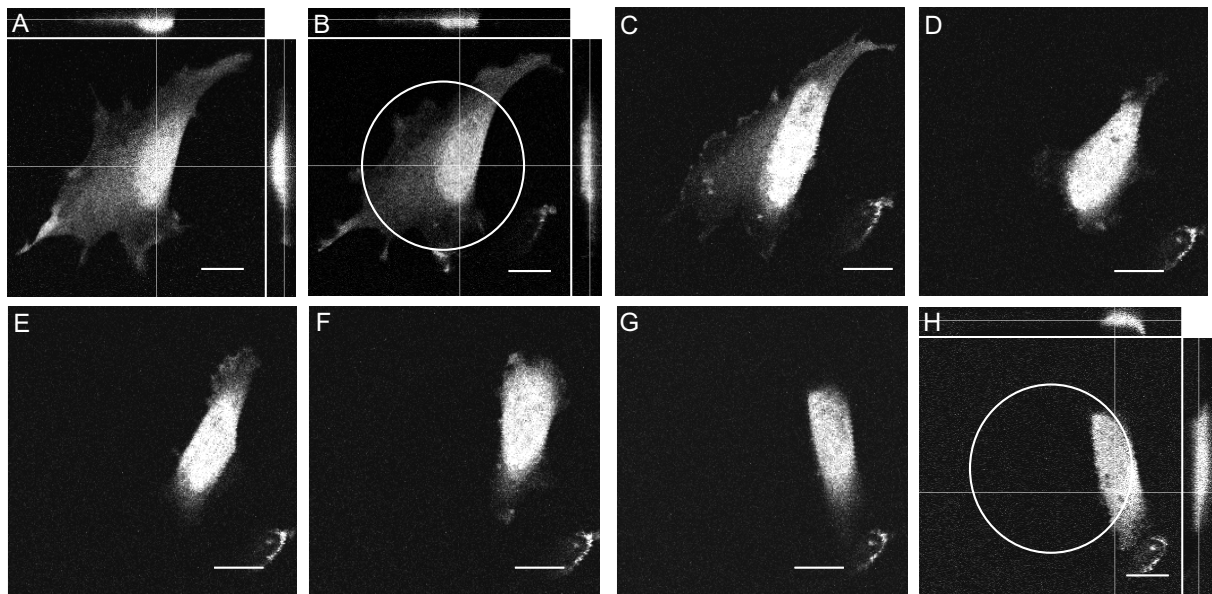


Figure 7.2: Long-term compression experiment on an individual C2C12 cell. The circle in images B and H indicates the position of the indenter. The scale bars indicate $20 \mu\text{m}$. A,B: Orthogonal projections of the undeformed cell (A) and the cell loaded with an axial strain of 30 %. C-G: Two-dimensional images of the cell at 3 (C), 6 (D), 9 (E), 12 (F) and 15 (G) hours after the axial strain was applied. H: Orthogonal projection of the cell after 15 hours.

7.5.2 Laminopathies

Laminopathies are inherited diseases caused by mutations in the LMNA gene, producing mainly lamin A and C. The *mechanical stress* hypothesis suggests that patients with laminopathies experience mechanical weakness in cells, caused by a disturbed nuclear architecture. Therefore, the role of A-type lamins in providing structural support to the nucleus and to cells in general was examined in chapter 6.

Compression experiments were performed to compare the load-bearing properties of two populations of cells: fibroblasts containing normal expression of the LMNA gene (MEF++ cells) and cells lacking expression of the LMNA gene (MEF-- cells).

These experiments showed that MEF^{-/-} cells were mechanically weaker than MEF^{+/+} cells (figure 6.1), which could be concluded from a significant decrease in mechanical resistance to deformation and a significantly lower bursting force. Partial rescue of the phenotype by transfection with either lamin A or lamin C-GFP prevented massive nuclear disruption, as seen in MEF^{-/-} cells (figure 6.3), but was unable to fully restore mechanical resistance to deformation in these cells (figure 6.2).

Simultaneous confocal images of the cell during a compression experiment revealed that the nuclei of MEF^{-/-} cells deformed isotropically, whereas the nuclei of MEF^{+/+} cells deformed anisotropically (figure 6.4). Strikingly, the three-dimensional architecture of cytoplasmic actin appeared to be disturbed in areas close to the nucleus of MEF^{-/-} cells (figure 6.5 B). Therefore, it was assumed that this isotropic deformation was caused by a lack of interaction between nuclear structures (i.e. lamins) and the cytoplasm via nesprin and actin. In addition, it was suggested that apart from the lack of nuclear lamins in MEF^{-/-} cells, the lost connection between the nucleus and the cytoplasm also contributes to the mechanical weakness as seen in these cells. This hypothesis could explain why laminopathies can cause muscle dystrophies, reminiscent to those seen if other actin-binding proteins are disturbed.

It remains to be elucidated what exactly caused the decreased mechanical resistance to deformation in MEF^{-/-} cells. Two possibilities include a mechanically weaker nucleus or the absence of the connection between the nucleus and the cytoskeleton. To support these suggestions, future experiments should be conducted on isolated nuclei, extracted from MEF^{-/-} and MEF^{+/+} cells.

Although LMNA knockout mice and the cell lines derived from these mice showed several characteristics of laminopathies (Sullivan et al., 1999), it should be investigated whether compression experiments on cells from patients with mutations in the LMNA gene reveal the same characteristics as the compression experiments on MEF^{-/-} cells. In addition, cells from normal volunteers and patients suffering from laminopathies should be compared. If similar differences are observed as in MEF^{+/+} and MEF^{-/-} cells, experiments on single cells of individual patients could be performed to identify patients at risk to develop laminopathies. Furthermore, the penetrance of the disease could be determined using these experiments. Hopefully, the loading device and the described experiments will provide diagnostic and prognostic tools in the near future.

7.6 Future perspectives on cell biomechanics

Owing to technological advancements, the field of cell biomechanics has grown rapidly over the last two decades. These technological advancements have been achieved on both an experimental and a computational level. From an experimental point of view, it is currently possible to resolve deformations and forces on the level of nanometers and piconewtons. A computational approach allows researchers to perform advanced finite element analyses, which were not possible a few years ago. Although studies on cell biomechanics clearly contributed to the characterisation of cellular properties

and understanding of various biological processes, still many discrepancies exist among these studies. As an example, some studies indenting the surface of an attached cell using atomic force microscopy report a higher stiffness at locations above the nucleus compared to the cell periphery (Miyazaki and Hayashi, 1999; Mathur et al., 2000), while other studies report the reverse effects (Grattarola et al., 1996; Haga et al., 2000; Sato et al., 2000). Furthermore, the values of elastic and viscoelastic parameters obtained by studies on cell biomechanics vary considerably (see table 5.3). These discrepancies are caused by several factors, such as differences in cell types, degree of cellular attachment, loading techniques and protocols, environmental conditions, and theoretical cell models used to estimate material parameters. All these factors tend to make it difficult and sometimes even impossible to compare the results from different studies. Standardisation of experimental procedures and techniques are required to allow and justify comparison between the outcomes of different studies on cell biomechanics. For non-attached cells, the micropipette aspiration technique has been successfully applied in many studies (reviewed in Hochmuth (2000)) and can almost be considered as a 'gold standard' technique. For attached cells, the loading technique presented in the current thesis could fulfil this task when made available to research institutions involved in the field of cell biomechanics.

7.7 General conclusions

In this thesis, the biomechanical response of single cells under compression was examined. Therefore, a loading device was developed to compress single attached cells and study their response. From experiments conducted with the device, the following conclusions can be drawn:

- The developed loading device can be used to examine the biomechanical response of single cells under well-defined conditions.
- Confocal laser scanning microscopy in conjunction with the three-dimensional image reconstruction and image analysis techniques presented in this thesis provides quantitative measures of cell deformation during compression.
- Cells, which have a preferred direction of orientation, deform perpendicular to this direction during compression. This might be attributed to the orientated actin cytoskeleton in these cells.
- Nuclei within these cells also deform perpendicular to this direction. This requires a correct connection between nuclear proteins and cytoskeletal structures. Within fibroblasts lacking A-type lamins, the connection between actin filaments and the nucleus was lost and resulted in an isotropic deformation of the nucleus during compression.

- The bursting force as well as the relationship between the applied axial strain and the accompanying force, provide useful measures to compare two different cell types with respect to their load-bearing properties.
- Cell bursting occurs when the applied axial strain exceeds 60 %, leading to the formation of bulges on the cell surface and eventually to rupturing of the cell membrane.
- Attached C2C12 muscle cells behave like a viscoelastic solid and exhibit non-linear material behaviour especially at loading frequencies higher than 1 Hertz. The elastic properties of C2C12 muscle cells can be captured by a Neo-Hookean material law.
- Alterations in the internal structure of a cell largely affect the load-bearing properties. Cells lacking A-type lamins have a reduced mechanical resistance to deformation and a lower bursting force.
- Nuclear A-type lamins are necessary to maintain the integrity of nuclei during compression.

Bibliography

- A-Hassan, E., Heinz, W. F., Antonik, M. D., D'Costa, N. P., Nageswaran, S., Schoenenberger, C. A., Hoh, J. H., 1998. Relative microelastic mapping of living cells by atomic force microscopy. *Biophysical Journal* 74, 1564–1578.
- Alberts, B., Bray, D., Lewis, J., Raff, M., Roberts, K., Watson, J. D., 1994. *Molecular biology of the cell*, 3rd Edition. Garland Publishing Inc., New York.
- Alcaraz, J., Buscemi, L., Grabulosa, M., Trepas, X., Fabry, B., Farre, R., D, D. N., 2003. Microrheology of human lung epithelial cells measured by atomic force microscopy. *Biophysical Journal* 84, 2071–2079.
- APUAP, 1989. Pressure ulcers prevalence, cost and risk assessment: consensus development conference statement. *Decubitus* 2, 24–28.
- Arnoczky, S. P., Lavagnino, M., Whallon, J. H., Hoonjan, A., 2002. In situ cell nucleus deformation in tendons under tensile load; a morphological analysis using confocal laser microscopy. *Journal of Orthopaedic Research* 20, 29–35.
- Artmann, G. M., Sung, K. L., Horn, T., Whittemore, D., Norwich, G., Chien, S., 1997. Micropipette aspiration of human erythrocytes induces echinocytes via membrane phospholipid translocation. *Biophysical Journal* 72, 1434–1441.
- Bader, D. L., Ohashi, T., Knight, M. M., Lee, D. A., Sato, M., 2002. Deformation properties of articular chondrocytes: a critique of three separate techniques. *Biorheology* 39, 69–78.
- Banes, A. J., 1993. Mechanical strain and the mammalian cell. In: Frangos, L. A. (Ed.), *Physical forces and the mammalian cell*, 1st Edition. Academic Press, Inc., London, Ch. 3, pp. 81–123.
- Banes, A. J., Sanderson, M., Boitano, S., Hu, P., Brigman, B., Tsuzaki, M., Fischer, T., Lawrence, W., 1994. Mechanical load and growth factors induce $[Ca^{2+}]$ release, cyclin D1 expression and DNA synthesis in avian tendon cells. In: Mow, V., Tran-Son-Tay, R., Guilak, F., Hochmuth, R. (Eds.), *Cell mechanics and cellular engineering*, 1st Edition. Springer-Verlag, New-York, Ch. 13, pp. 210–232.

- Banes, A. J., Tsuzaki, M., Hu, P., Brigman, B., Brown, T., Miller, L., 1995. Mechanoreception at the cellular level: the detection, interpretation, and diversity of responses to mechanical signals. *Biochemical Cell Biology* 73, 349–365.
- Barbenel, J. C., 1991. Pressure management. *Prosthetics and Orthotics International* 15, 225–231.
- Bathe, K. J., 1996. Finite element procedures. New Jersey: Prentice Hall, 1037.
- Bausch, A. R., Ziemann, F., Boulbitch, A. A., Jacobson, K., Sackmann, E., 1998. Local measurements of viscoelastic parameters of adherent cell surfaces by magnetic bead microrheometry. *Biophysical Journal* 75, 2038–2049.
- Ben-Ze'ev, A., 1991. Animal cell shape changes and gene expression. *Bioessays* 13 (5), 207–212.
- Bhadriraju, K., Hansen, L. K., 2002. Extracellular matrix- and cytoskeleton-dependent changes in cell shape and stiffness. *Experimental Cell Research* 278, 92–100.
- Biamonit, G., Giacca, M., Perinia, G., Contreas, G., Zentilin, L., Weighardt, F., Guerra, M., Valle, G. D., Saccone, S., Riva, S., Falaschi, A., 1992. The gene for a novel human lamin maps at a highly transcribed locus of chromosome 19, which replicates at the onset of S-phase. *Molecular Cell Biology* 12, 3499–3506.
- Bliss, M. R., 1993. Aetiogy of pressure sores. *Clinical Gerontology* 3, 379–397.
- Bluhm, W. F., McCulloch, A. D., Lew, W. Y. W., 1995. Active force in rabbit ventricular myocytes. *Journal of Biomechanics* 9, 1119–1122.
- Bonne, G., Barletta, M. R. D., Varnous, S., Becane, H. M., Hammouda, E. H., Merlini, L., Muntoni, F., Greenberg, C. R., Gary, F., Urtizberea, J. A., Duboc, D., Fardeau, M., Toniolo, D., Schwartz, K., 1999. Mutations in the gene encoding lamin A/C cause autosomal dominant Emery-Dreifuss muscular dystrophy. *Nature Genetics* 21, 285–288.
- Bosboom, E. M. H., 2001. Deformation as a trigger for pressure sore related muscle damage. Ph.D. thesis.
- Bosboom, E. M. H., Bouten, C. V. C., Oomens, C. W. J., Baaijens, F. P. T., Nicolay, K., 2003. Quantifying pressure sore related muscle damage using high-resolution MRI. *Journal of Applied Physiology* .
- Bosboom, E. M. H., Bouten, C. V. C., Oomens, C. W. J., van Straaten, H. W. M., Baaijens, F. P. T., Maderich, V. S., 2001. Quantification and localisation of damage in rat muscles after controlled loading; a new approach to study the aetiology of pressure sores. *Medical Engineering and Physics* 23, 195–200.

- Bours, G. J. J. W., Halfens, R. J. G., Abu-Saad, H. H., Grol, R. T. P. M., 2002. Prevalence, prevention, and treatment of pressure ulcers: descriptive study in 89 institutions in the Netherlands. *Research in Nursing and Health* 25, 99–110.
- Bouten, C. V., Breuls, R. G., Peeters, E. A., Oomens, C. W., Baaijens, F. P., 2003a. In vitro models to study compressive strain-induced muscle cell damage. *Biorheology* 40, 383–388.
- Bouten, C. V., Oomens, C. W., Baaijens, F. P., Bader, D. L., 2003b. The etiology of pressure ulcers: skin deep or muscle bound? *Archives of Physical Medicine and Rehabilitation* 84, 616–619.
- Bouten, C. V. C., Bosboom, E. M. H., Oomens, C. W. J., 1999. The aetiology of pressure sores: a tissue and cell mechanics approach. In: van der Woude et al., L. (Ed.), *Biomedical aspects of manual wheelchair propulsion*. IOS Press, Amsterdam, pp. 52–62.
- Bouten, C. V. C., Knight, M. M., Lee, D. A., Bader, D. L., 2001. Compressive deformation and damage of muscle cell subpopulations in a model system. *Annals of Biomedical Engineering* 29, 153–163.
- Breuls, R. G., Mol, A., Petterson, R., Oomens, C. W., Baaijens, F. P., Bouten, C. V., 2003a. Monitoring local cell viability in engineered tissues: a fast, quantitative, and nondestructive approach. *Tissue Engineering* 9, 269–281.
- Breuls, R. G., Sengers, B. G., Oomens, C. W., Bouten, C. V., Baaijens, F. P., 2002. Predicting local cell deformations in engineered tissue constructs: a multilevel finite element approach. *Journal of Biomechanical Engineering* 124, 198–207.
- Breuls, R. G. M., Oomens, C. W. J., Bouten, C. V. C., Bader, D. L., Baaijens, F., 2003b. Compression induced cell damage in engineered muscle tissue: an in-vitro model to study pressure ulcer aetiology. *Annals of Biomedical Engineering* 31, 1357–1364.
- Breuls, R. G. M., Oomens, C. W. J., Bouten, C. V. C., Bader, D. L., Baaijens, F., 2003c. A theoretical analysis of damage evolution in skeletal muscle tissue with reference to pressure ulcer development. *Journal of Biomechanical Engineering* 125, 902–909.
- Brodland, G. W., Veldhuis, J. H., 2002. Computer simulations of mitosis and interdependencies between mitosis orientation, cell shape and epithelia reshaping. *Journal of Biomechanics* 35, 673–681.
- Broers, J. L., Machiels, B. M., Kuijpers, H. J., Smedts, F., van den Kieboom, R., Raymond, Y., Ramaekers, F., 1997. A- and B-type lamins are differentially expressed in normal human tissues. *Histochemistry and Cell Biology* 107, 505–517.

- Broers, J. L. V., Machiels, B. M., van Eys, G. J. J., Kuijpers, H. J. H., Manders, E. M. M., van Driel, R., Ramaekers, F., 1999. Dynamics of the nuclear lamina as monitored by GFP-tagged A-type lamins. *Journal of Cell Science* 112, 3463–3475.
- Brown, T. D., 2000. Techniques for mechanical stimulation of cells in vitro: a review. *Journal of Biomechanics* 33, 3–14.
- Bucher, D., Scholz, M., Stetter, M., Obermayer, K., Pflüger, H. J., 2000. Correction methods for three-dimensional reconstructions from confocal images: I. tissue shrinking and axial scaling. *Journal of Neuroscience* 100, 135–143.
- Burke, B., Stewart, C. L., 2002. Life at the edge: the nuclear envelope and human disease. *Nature Reviews* 3, 575–585.
- Caille, N., Thoumine, O., Tardy, Y., Meister, J.-J., 2002. Contribution of the nucleus to the mechanical properties of endothelial cells. *Journal of Biomechanics* 35, 177–187.
- Cao, H., Hegele, R. A., 2000. Nuclear lamin A/C R482Q mutation in Canadian kindreds with Dunnigan-type familial partial lipodystrophy. *Human Molecular Genetics* 9, 109–112.
- Cao, H., Hegele, R. A., 2003. LMNA is mutated in Hutchinson-Gilford progeria (MIM 176670) but not in Wiedemann-Rautenstrauch progeroid syndrome (MIM 264090). *Journal of Human Genetics* 48, 271–274.
- Caplan, A., Carlson, B., Faulkner, J., Fischman, D., Garrett, W., 1988. Skeletal muscle. In: Woo, S. L.-Y., Buckwalter, J. A. (Eds.), *Injury and repair of the musculoskeletal soft tissues*. American Academy of Orthopaedic Surgeons, Park Ridge, pp. 213–291.
- Carmo-Fonseca, M., Kern, H., Hurt, E. C., 1991. Human nucleoporin p62 and the essential yeast nuclear pore protein NSP1 show sequence homology and a similar domain organization. *European Journal of Cell Biology* 55, 17–30.
- Chen, C. S., Ingber, D. E., 1999. Tensegrity and mechanoregulation: from skeleton to cytoskeleton. *Osteoarthritis and Cartilage* 7 (1), 81–94.
- Chen, C. S., Mrksich, M., Huang, S., Whitesides, G. M., Ingber, D. E., 1997. Geometric control of cell life and death. *Science* 276, 1425–1428.
- Chien, S., Sung, K. P., 1984. Effect of colchicine on viscoelastic properties of neutrophils. *Biophysical Journal* 46, 383–386.
- Choquet, D., Felsenfeld, D. P., Sheetz, M. P., 1997. Extracellular matrix rigidity causes strengthening of integrin-cytoskeleton linkages. *Cell* 88, 39–48.
- Clarke, M. S. F., Feedback, D. L., 1996. Mechanical load induces sarcoplasmic wounding and FGF release in differentiated human skeletal muscle cultures. *FASEB Journal* 10 (4), 502–509.

- Cohen, M., Lee, K. K., Wilson, K. L., Gruenbaum, Y., 2001. Transcriptional repression, apoptosis, human disease and the functional evolution of the nuclear lamina. *Trends in Biochemical Sciences* 26, 41–47.
- Cohen, M., Tzur, Y. B., Neufeld, E., Feinstein, N., Delannoy, M., Wilson, K., Gruenbaum, Y., 2002. Transmission electron microscope studies of the nuclear envelope in *Caenorhabditis elegans* embryos. *Journal of Structural Biology* 140, 232–240.
- Collinsworth, A. M., Zhang, S., Kraus, W. E., Truskey, G. A., 2002. Apparent elastic modulus and hysteresis of skeletal muscle cells throughout differentiation. *American Journal of Physiology: Cell Physiology* 283, 1219–1227.
- Coughlin, M. F., Stamenović, D., 1998. A tensegrity model of the cytoskeleton in spread and round cells. *Journal of Biomechanical Engineering* 120, 770–777.
- Cubitt, A. B., Heim, R., Adams, S. R., Boyd, A. E., Gross, L. A., Tsien, R. Y., 1995. Understanding, improving and using green fluorescent proteins. *Trends in Biochemical Sciences* 20, 448–455.
- Daily, B., Elson, E. L., 1984. Cell poking: determination of the elastic area compressibility modulus of the erythrocyte membrane. *Biophysical Journal* 45, 671–682.
- Daniel, R. K., Priest, D. L., Wheatly, D. C., 1981. Etiologic factors in pressure sores: An experimental model. *Archives of Physical and Medical Rehabilitation* 62, 492–498.
- Davies, P. F., Tripathi, S. C., 1993. Mechanical stress mechanisms and the cell: an endothelial paradigm. *Circulation Research* 72 (2), 239–244.
- Doktycz, M. J., Sullivan, C. J., Hoyt, P. R., Pelletier, D. A., Wu, S., Allison, D. P., 2003. AFM imaging of bacteria in liquid media immobilized on gelatin coated mica surfaces. *Ultramicroscopy* 97, 209–216.
- Dong, C., Skalak, R., 1992. Leukocyte deformability: finite element modeling of large viscoelastic deformation. *Journal of Theoretical Biology* 158, 173–193.
- Dong, C., Skalak, R., Sung, K. P., Schmid-Schönbein, G. W., Chien, S., 1988. Passive deformation analysis of human leukocytes. *Journal of Biomechanical Engineering* 110, 27–36.
- Dreuillet, C., Tillit, J., Kress, M., Ernoult-Lange, M., 2002. In vivo and in vitro interaction between human transcription factor MOK2 and nuclear lamin A/C. *Nucleic Acids Research* 30, 4634–4642.
- Dumas, D., Grossin, L., Cauchois, G., Gentils, M., Santus, R., Stoltz, J. E., 2003. Comparison of wide-field/deconvolution and confocal microscopy in bioengineering. Interest of multi-photon microscopy in the study of articular cartilage. *Biorheology* 40, 253–259.

- Dyer, J. A., Kill, I. R., Pugh, G., Quinlan, R. A., Lane, E. B., Hutchison, C. J., 1997. Cell cycle changes in A-type lamin associations detected in human dermal fibroblasts using monoclonal antibodies. *Chromosome Research* 5, 383–394.
- Elson, E. L., 1988. Cellular mechanics as an indicator of cytoskeletal structure and function. *Annual Review of Biophysics and Biophysical Chemistry* 17, 397–430.
- Emmert-Buck, M. R., Bonner, R. F., Smith, P. D., Chuaqui, R. F., Zhuang, Z., Goldstein, S. R., Weiss, R. A., Liotta, L. A., 1996. Laser capture microdissection. *Science* 274, 921–922.
- Eriksson, M., Brown, W. T., Gordon, L. B., Glynn, M. W., Singer, J., Scott, L., Erdos, M. R., Robbins, C. M., Moses, T. Y., Berglund, P., Dutra, A., Pak, E., Durkin, S., Csoka, A. B., Boehnke, M., Glover, T. W., Collins, F. S., 2003. Recurrent de novo point mutations in lamin A cause Hutchinson-Gilford progeria syndrome. *Nature* 423, 293–298.
- Errington, R. J., Fricker, M. D., Wood, J. L., Hall, A. C., White, N. S., 1997. Four-dimensional imaging of living chondrocytes in cartilage using confocal microscopy: a pragmatic approach. *American Journal of Physiology* 272, 104–1051.
- Evans, E., Yeung, A., 1989. Apparent viscosity and cortical tension of blood granulocytes determined by micropipet aspiration. *Biophysical Journal* 56, 151–160.
- Evans, E. A., Waugh, R., Melnik, L., 1976. Elastic area compressibility modulus of red cell membrane. *Biophysical Journal* 16, 585–595.
- Fatkin, D., MacRae, C., Sasaki, T., Wolff, M. R., Porcu, M., Frenneaux, M., Atherton, J., Vidaillet, H. J., Spudich, S., Girolami, U. D., Seidman, J. G., Seidman, C., Muntoni, F., Muehle, G., Johnson, W., McDonough, B., 1999. Missense mutations in the rod domain of the lamin A/C gene as causes of dilated cardiomyopathy and conduction-system disease. *The New England Journal of Medicine* 341, 1715–1724.
- Feng, J., Yan, J., Buzin, C. H., Towbin, J. A., Sommer, S. S., 2002. Mutations in the dystrophin gene are associated with sporadic dilated cardiomyopathy. *Molecular Genetics and Metabolism* 77, 119–126.
- Folch, A., Toner, M., 2000. Microengineering of cellular interactions. *Annual Review of Biomedical Engineering* 2, 227–256.
- Frangos, J. A., 1993. *Physical forces and the mammalian cell*. Academic Press, Inc., London.
- Frenette, J., Tidball, J. G., 1998. Mechanical loading regulates expression of talin and its mRNA, which are concentrated at myotendinous junctions. *American Journal of Physiology* 275, C818–C825.

- Furukawa, K., Hotta, Y., 1993. cDNA cloning of a germ cell specific lamin B3 from mouse spermatocytes and analysis of its function by ectopic expression in somatic cells. *EMBO Journal* 12, 97–106.
- Galbraith, C. G., Skalak, R., Chien, S., 1998. Shear stress induces spatial reorganization of the endothelial cell cytoskeleton. *Cell Motility and the Cytoskeleton* 40, 317–330.
- Genschel, J., Schmidt, H. H., 2000. Mutations in the LMNA gene encoding lamin A/C. *Human Mutation* 16, 451–459.
- Gerdes, H. H., Kaether, C., 1996. Green fluorescent protein: applications in cell biology. *FEBS Letters* 389, 44–47.
- Gittes, F., Mickey, B., Nettleton, J., Howard, J., 1993. Flexural rigidity of microtubules and actin filaments measured from thermal fluctuations in shape. *Journal of Cell Biology* 120 (4), 923–934.
- Goldman, R. D., Clement, S., Khuon, S., Moir, R., Trejo-Skalli, A., Spann, T., Yoon, M., 1998. Intermediate filament cytoskeletal system: dynamic and mechanical properties. *Biological Bulletin* 194, 361–363.
- Goldman, R. D., Khuon, S., Chou, Y. H., Opal, P., Steinert, P., 1996. The function of intermediate filaments in cell shape and cytoskeletal integrity. *Journal of Cell Biology* 134 (4), 971–983.
- Görlich, D., Kutay, U., 1999. Transport between the cell nucleus and the cytoplasm. *Annual Review of Cell and Developmental Biology* 15, 607–660.
- Grattarola, M., Ricci, D., Tedesco, M., 1996. Atomic force microscopy on cells adhering to a substrate: a tool for cellular engineering. In: *Cellular Engineering*. IEEE, pp. 2053–2054.
- Gruenbaum, Y., Wilson, K. L., Harel, A., Goldberg, M., Cohen, M., 2000. Review: nuclear lamins—structural proteins with fundamental functions. *Journal of Structural Biology* 129, 313–323.
- Gudi, S. R. P., Lee, A. A., Clark, C. B., Frangos, J. A., 1998. Equibiaxial strain and strain rate stimulate early activation of G proteins in cardiac fibroblasts. *American Journal of Physiology* 274 (5 Pt 1), C1424–1428.
- Guharay, F., Sachs, F., 1984. Stretch-activated single ion channel currents in tissue-cultured embryonic chick skeletal muscle. *Journal of Physiology* 352, 685–701.
- Guilak, F., 1995. Compression-induced changes in the shape and volume of the chondrocyte nucleus. *Journal of Biomechanics* 28 (12), 1529–1541.

- Guilak, F., Donahue, H. J., Zell, R. A., Grande, D., McLeod, K. J., Rubin, C. T., 1994. Deformation-induced calcium signaling in articular chondrocytes. In: Mow, V., Tran-Son-Tay, R., Guilak, F., Hochmuth, R. (Eds.), *Cell mechanics and cellular engineering*, 1st Edition. Springer-Verlag, New-York, Ch. 21, pp. 380–397.
- Guilak, F., Erickson, G. R., Ting-Beall, H. P., 2002. The effects of osmotic stress on the viscoelastic and physical properties of articular chondrocytes. *Biophysical Journal* 82, 720–727.
- Guilak, F., Ratcliffe, A., Mow, C., 1995. Chondrocyte deformation and local tissue strain in articular cartilage: a confocal microscopy study. *Journal of Orthopaedic Research* 13, 410–421.
- Guilak, F., Tedrow, J. R., Burgkart, R., 2000. Viscoelastic properties of the cell nucleus. *Biochemical and Biophysical Research Communications* 269, 781–786.
- Haga, H., Sasaki, S., Kawabata, K., Ito, E., Ushiki, T., Sambongi, T., 2000. Elasticity mapping of living fibroblasts by AFM and immunofluorescence observation of the cytoskeleton. *Ultramicroscopy* 82, 253–258.
- Hägerstrand, H., Danieluk, M., Bobrowska-Hägerstrand, M., Iglic, A., Wróbel, A., 2000. Influence of band 3 protein absence and skeletal structures on amphiphile- and Ca(2+)-induced shape alterations in erythrocytes: a study with lamprey (*Lampetra fluviatilis*), trout (*Onchorhynchus mykiss*) and human erythrocytes. *Biochimica et Biophysica Acta* 1466, 125–138.
- Hägerstrand, H., Kralj-Iglic, V., Bobrowska-Hägerstrand, M., Iglic, A., 1999. Membrane skeleton detachment in spherical and cylindrical microexovesicles. *Bulletin of Mathematical Biology* 61, 1019–1030.
- Harborth, J., Elbashir, S. M., Bechert, K., Tuschl, T., Weber, K., 2001. Identification of essential genes in cultured mammalian cells using small interfering RNAs. *Journal of Cell Science* 114, 4557–4565.
- Hell, S., Reiner, G., Cremer, C., Stelzer, E. H. K., 1993. Aberrations in confocal fluorescence microscopy induced by mismatches in refractive index. *Journal of Microscopy* 169, 391–405.
- Hochmuth, R. M., 2000. Micropipette aspiration of living cells. *Journal of Biomechanics* 33, 15–22.
- Hozak, P., Sasseville, A. M., Raymond, Y., Cook, P. R., 1995. Lamin proteins form an internal nucleoskeleton as well as a peripheral lamina in human cells. *Journal of Cell Science* 108, 635–644.

- Iglic, A., Hägerstrand, H., 1999. Amphiphile-induced spherical microexovesicle corresponds to an extreme local area difference between two monolayers of the membrane bilayer. *Medical and Biological Engineering and Computing* 37, 125–129.
- Ingber, D. E., 1993. Cellular tensegrity: defining new rules of biological design that govern the cytoskeleton. *Journal of Cell Science* 104, 613–627.
- Ingber, D. E., 1997. Tensegrity: the architectural basis of cellular mechanotransduction. *Annual Reviews of Physiology* 59, 575–599.
- Janmey, P. A., 1998. The cytoskeleton and cell signaling: component localization and mechanical coupling. *Physiological Reviews* 78 (3), 763–781.
- Janmey, P. A., Euteneuer, U., Traub, P., Schliwa, M., 1991. Viscoelastic properties of vimentin compared with other filamentous biopolymer networks. *Journal of Cell Biology* 113 (1), 155–160.
- Jones, W. R., Ting-Beall, H. P., Lee, C. M., Kelley, S. S., Hochmuth, R. M., Guilak, F., 1999. Alterations in the Young's modulus and volumetric properties of chondrocytes isolated from normal and osteoarthritic human cartilage. *Journal of Biomechanics* 32, 119–127.
- Kan, H., Shyy, W., Udaykumar, H. S., Vigneron, P., Tran-Son-Tay, R., 1999. Effects of nucleus on leucocyte recovery. *Annals of Biomedical Engineering* 27 (5), 648–655.
- Kano, H., Voort, H. T. M., Schrader, M., Kempen, G. M. P., Hell, S. W., 1996. Avalanche photodiode detection with object scanning and image restoration provides 2-4 fold resolution increase in two-photon fluorescence microscopy. *Bioimaging* 4, 187–197.
- Karcher, H., Lammerding, J., Huang, H., Lee, R. T., Kamm, R. D., Kaazempur-Mofrad, M. R., 2003. A three-dimensional viscoelastic model for cell deformation with experimental verification. *Biophysical Journal* 85, 3336–3349.
- Karlon, W. J., Hsu, P., Li, S., Chien, S., McCulloch, A. D., Omens, J. H., 1999. Measurement of orientation and distribution of cellular alignment and cytoskeletal organization. *Annals of Biomedical Engineering* 27, 712–720.
- Kempen, G. M. P., van Vliet, L. J., Verveer, P. J., van der Voort, H. T. M., 1997. A quantitative comparison of image restoration methods for confocal microscopy. *Journal of Microscopy* 185, 354–365.
- Knight, K. R., Messina, A., Hurley, J. V., Zhang, B., Morrison, W. A., Stewart, A. G., 1999. Muscle cells become necrotic rather than apoptotic during reperfusion of ischaemic skeletal muscle. *International Journal of Experimental Pathology* 80, 169–175.
- Knight, M. M., Lee, D. A., Bader, D. L., 1996. Distribution of chondrocyte deformation in compressed agarose gel using confocal microscopy. *Cellular Engineering* 1, 97–102.

- Koay, E. J., Shieh, A. C., Athanasiou, K. A., 2003. Creep indentation of single cells. *Journal of Biomechanical Engineering* 125, 334–341.
- Komuro, I., Katoh, Y., Kaida, T., Shibazaki, Y., Kurabayashi, M., Hoh, E., Takaku, F., Yazaki, Y., 1991. Mechanical loading stimulates cell hypertrophy and specific gene expression in cultured rat cardiac myocytes. *Journal of Biological Chemistry* 266 (2), 1265–1268.
- Kosiak, M., 1961. etiology of decubitus ulcers. *Archives of Physical and Medical Rehabilitation* 92, 19–29.
- Kralj-Iglic, V., Iglic, A., Hägerstrand, H., Peterlin, P., 2000. Stable tubular microexovesicles of the erythrocyte membrane induced by dimeric amphiphiles. *Physical Review E*. 61, 4230–4234.
- Krouskop, T. A., 1983. A synthesis of the factors that contribute to pressure sore formation. *Medical Hypotheses* 11, 255–267.
- Laurent, V. M., Henon, S., Planus, E., Fodil, R., Balland, M., Isabey, D., Gallet, F., 2002. Assessment of mechanical properties of adherent living cells by bead micromanipulation: comparison of magnetic twisting cytometry vs optical tweezers. *Journal of Biomechanical Engineering* 124, 408–421.
- Lee, D. A., Knight, M. M., Bolton, J. F., Idowu, B. D., Kayser, M. V., Bader, D. L., 2000. Chondrocyte deformation within compressed agarose constructs at the cellular and sub-cellular levels. *Journal of Biomechanics* 33, 81–95.
- Lin, F., Worman, H., 1993. Structural organization of the human gene encoding nuclear lamin A and nuclear lamin C. *Journal of Biological Chemistry* 268, 16321–16326.
- Lin, F., Worman, H. J., 1995. Structural organization of the human gene (LMNB1) encoding nuclear lamin B1. *Genomics* 27, 230–236.
- Liu, S. C., Derick, L. H., Duquette, M. A., Palek, J., 1989. Separation of the lipid bilayer from the membrane skeleton during discocyte-echinocyte transformation of human erythrocyte ghosts. *European Journal of Cell Biology* 49, 358–365.
- Lloyd, D. J., Trembath, R. C., Shackleton, S., 2002. A novel interaction between lamin A and SREBP1: implications for partial lipodystrophy and other laminopathies. *Human Molecular Genetics* 11, 769–777.
- Luna, E. J., Hitt, A. L., 1992. Cytoskeleton-plasma membrane interactions. *Science* 258, 955–963.
- Machiels, B. M., Broers, J. L., Raymond, Y., de Ley, L., Kuijpers, H. J., Caberg, N. E., Ramaekers, F. C., 1995. Abnormal A-type lamin organization in a human lung carcinoma cell line. *European Journal of Cell Biology* 67, 328–335.

- Machiels, B. M., Zorenc, A. H. G., Endert, J. M., Kuijpers, H. J. H., van Eys, G. J. J. M., Ramaekers, F. C. S., Broers, J. L. V., 1996. An alternative splicing product of the lamin A/C gene lacks exon 10. *Journal of Biological Chemistry* 271, 9249–9253.
- Maksym, G. N., Fabry, B., Butler, J. P., Navajas, D., Tschumperlin, D. J., Laporte, J. D., Fredberg, J. J., 2000. Mechanical properties of cultured human airway smooth muscle cells from 0.05 to 0.4 Hz. *Journal of Applied Physiology* 89, 1619–1632.
- Mancini, M. A., Shan, B., Nickerson, J. A., Penman, S., Lee, W. H., 1993. The retinoblastoma gene product is a cell cycle-dependent, nuclear matrix-associated protein. *Proceedings of the National Academy of Sciences of the USA* 91, 418–422.
- Maniotis, A. J., Chien, C. S., Ingber, D. E., 1997. Demonstration of mechanical connections between integrins, cytoskeletal filaments, and nucleoplasm that stabilize nuclear structure. *Proceedings of the National Academy of Sciences of the United States of America* 94, 849–854.
- Markiewicz, E., Dechat, T., Foisner, R., Quinlan, R. A., Hutchison, C. J., 2002. Lamin A/C binding protein LAP2alpha is required for nuclear anchorage of retinoblastoma protein. *Molecular Biology of the Cell* 13, 4401–4413.
- Mathur, A. B., Collinsworth, A. M., Reichert, W. M., Kraus, W. E., Truskey, G. A., 2001. Endothelial, cardiac muscle and skeletal muscle exhibit different viscous and elastic properties as determined by atomic force microscopy. *Journal of Biomechanics* 34, 1545–1553.
- Mathur, A. B., Truskey, G. A., Reichert, W. M., 2000. Atomic force and total internal reflection fluorescence microscopy for the study of force transmission in endothelial cells. *Biophysical Journal* 78, 1725–1735.
- McConnaughey, W. B., Petersen, N. O., 1980. The cell poker: An apparatus for stress-strain measurements on living cells. *Review of Scientific Instruments* 51, 575–580.
- McMahon, D. K., Andersson, P. A. W., Nassar, R., Bunting, J. B., Saba, Z., Oakeley, A. E., Malouf, N. N., 1994. C₂C₁₂ cells: biophysical, biochemical and immunocytochemical properties. *American Journal of Physiology. Cell Physiology* 266, 1795–1802.
- Mislow, J. M., Holaska, J. M., Kim, M. S., Lee, K. K., Segura-Totten, M., Wilson, K. L., McNally, E. M., 2002. Nesprin-1alpha self-associates and binds directly to emerin and lamin A in vitro. *FEBS letters* 525, 135–140.
- Miyazaki, H., Hayashi, K., 1999. Atomic force microscopic measurement of the mechanical properties of intact endothelial cells in fresh arteries. *Medical and Biological Engineering and Computing* 37, 530–536.

- Moir, R. D., Spann, T. P., Herrmann, H., Goldman, R. D., 2000. Disruption of nuclear lamin organization blocks the elongation phase of DNA replication. *Journal of Cell Biology* 149, 1179–1191.
- Mol, A., Bouten, C. V., Zund, G., Gunter, C. I., Visjager, J. F., Turina, M. I., Baaijens, F. P., Hoerstrup, S. P., 2003. The relevance of large strains in functional tissue engineering of heart valves. *The Thoracic and Cardiovascular Surgeon* 51, 78–83.
- Mooney, D., Hansen, L., Vacanti, J., Langer, R., Farmer, S., Ingber, D., 1992. Switching from differentiation to growth in hepatocytes: control by extracellular matrix. *Journal of Cell Physiology* 151, 497–505.
- Moore, S. W., 1994. A fiber optic system for measuring dynamic mechanical properties of embryonic tissues. *IEEE Transactions of Biomedical Engineering* 41, 45–50.
- Mounkes, L. C., Kozlov, S., Hernandez, L., Sullivan, T., Stewart, C. L., 2003. A progeroid syndrome in mice is caused by defects in A-type lamins. *Nature* 423, 298–301.
- Muchir, A., Bonne, G., van der Kool, A. J., van Meegen, M., Baas, F., Bolhuis, P. A., de Visser, M., Schwartz, K., 2000. Identification of mutations in the gene encoding lamins A/C in autosomal dominant limb girdle muscular dystrophy with atrioventricular conduction disturbances (LGMD1B). *Human Molecular Genetics* 9, 1453–1459.
- Muchir, A., van Engelen, B. G., Lammens, M., Mislow, J. M., McNally, E., Schwartz, K., 2003, G. B., 2003. Nuclear envelope alterations in fibroblasts from LGMD1B patients carrying nonsense Y259X heterozygous or homozygous mutation in lamin A/C gene. *Experimental Cell Research* 298, in press.
- Needham, D., Hochmuth, R. M., 1990. Rapid flow of passive neutrophils into a 4 μm pipet and measurement of cytoplasmic viscosity. *Journal of Biomechanical Engineering* 112, 269–276.
- Nola, G. T., Vistnes, L. M., 1980. Differential response of skin and muscle in the experimental production of pressure sores. *Plastic and Reconstructive Surgery* 66, 728–733.
- North, K. N., Beggs, A. H., 1996. Deficiency of a skeletal muscle isoform of alpha-actinin (alpha-actinin-3) in merosin-positive congenital muscular dystrophy. *Neuromuscular Disorders* 6, 229–235.
- Oomens, C. W. J., Bressers, O. F. J. T., Bosboom, E. M. H., Bouten, C. V. C., Bader, D., 2003. Can loaded interface characteristics influence strain distributions in muscle adjacent to bony prominences? *Computational Methods in Biomechanics and Biomedical Engineering* 6, 171–180.

- Ozaki, T., Saijo, M., Murakami, K., Enomoto, H., Taya, Y., Sakiyama, S., 1994. Complex formation between lamin A and the retinoblastoma gene product: identification of the domain on lamin A required for its interaction. *Oncogene* 9, 2649–2653.
- Peeters, E. A. G., Bouten, C. V. C., Oomens, C. W. J., Baaijens, F. P. T., 2003. Monitoring the biomechanical response of individual cells under compression: a new compression device. *Medical and Biological Engineering and Computing* 41, 498–503.
- Penman, S., 1995. Rethinking cell structure. *Proceedings of the National Academy of Sciences of the United States of America* 92, 5251–5257.
- Perrone, C. E., Fenwick-Smith, D., Vandeburgh, H. H., 1995. Collagen and stretch modulate autocrine secretion of insulin-like growth factor-1 and insulin-like growth factor binding proteins from differentiated skeletal muscle cells. *Journal of Biological Chemistry* 270 (5), 2099–2106.
- Petersen, N. O., McConnaughey, W. B., Elson, E. L., 1982. Dependence of locally measured cellular deformability on position on the cell, temperature, and cytochalasin B. *Proceedings of the National Academic of Science of the USA* 79, 5327–5331.
- Puig-De-Morales, M., Grabulosa, M., Alcaraz, J., Mullol, J., Maksym, G. N., Fredberg, J. J., Navajas, D., 2001. Measurement of cell microrheology by magnetic twisting cytometry with frequency domain demodulation. *Journal of Applied Physiology* 91, 1152–1159.
- Ra, H. J., Picart, C., Feng, H., Sweeney, H. L., Discher, D. E., 1999. Muscle cell peeling from micropatterned collagen: direct probing of focal and molecular properties of matrix adhesion. *Journal of Cell Science* 112, 1425–1436.
- Ricci, D., Tedesco, M., Grattarola, M., 1997. Mechanical and morphological properties of living 3T6 cells probed via scanning force microscopy. *Microscopy Research and Technique* 36, 165–171.
- Röber, R. A., Sauter, H., Weber, K., Osborn, M., 1990. Cells of the cellular immune and hemopoietic system of the mouse lack lamins A/C: distinction versus other somatic cells. *Journal of Cell Science* 95, 587–598.
- Röber, R. A., Weber, K., Osborn, M., 1989. Differential timing of nuclear lamin A/C expression in the various organs of the mouse embryo and the young animal: a developmental study. *Development* 105, 365–378.
- Sandre-Giovannoli, A. D., Bernard, R., Cau, P., Navarro, C., Amiel, J., Boccaccio, I., Lyonnet, S., Stewart, C., Munnich, A., Merrer, M. L., Levy, N., 2003. Lamin A truncation in Hutchinson-Gilford progeria. *Science* 300(5628), 2055.

- Sandre-Giovannoli, A. D., Chaouch, M., Kozlov, S., Vallat, J. M., Tazir, M., Kassouri, N., Szepetowski, P., Hammadouche, T., Vandenberghe, A., Stewart, C., Grid, D., Levy, N., 2002. Homozygous defects in LMNA, encoding lamin A/C nuclear-envelope proteins, cause autosomal recessive axonal neuropathy in human (Charcot-Marie-Tooth disorder type 2) and mouse. *American Journal of Human Genetics* 70, 726–736.
- Sandri, M., Carraro, U., 1999. Apoptosis of skeletal muscles during development and disease. *International Journal of Biochemistry and Cell Biology* 31, 1373–1390.
- Sato, M., Nagayama, K., Kataoka, N., Sasaki, M., Hane, K., 2000. Local mechanical properties measured by atomic force microscopy for cultured bovine endothelial cells exposed to shear stress. *Journal of Biomechanics* 33, 127–135.
- Sato, M., Theret, D. P., Wheeler, L. T., Ohshima, N., Nerem, R. M., 1990. Application of the micropipette technique to the measurement of cultured porcine aortic endothelial cell viscoelastic properties. *Journal of Biomechanical Engineering* 112, 263–268.
- Schmid-Schönbein, G. W., Sung, K.-L. P., Tözeren, H., Skalak, R., 1981. Passive mechanical properties of human leukocytes. *Biophysical Journal* 36, 243–256.
- Schroder, R., Reimann, J., Salmikangas, P., Clemen, C. S., Hayashi, Y. K., Nonaka, I., Arahata, K., Carpen, O., 2003. Beyond LGMD1A: myotilin is a component of central core lesions and nemaline rods. *Neuromuscular Disorders* 13, 451–455.
- Sheppard, J., 1989. Axial resolution of confocal fluorescence microscopy. *Journal of Microscopy* 154, 237–241.
- Shiu, C., Zhang, Z., Thomas, C. R., 1999. A novel technique for the study of bacterial cell mechanical properties. *Biotechnology Techniques* 13, 707–713.
- Srivatanauksorn, Y., Srivatanauksorn, V., Lemoine, N. R., 2002. DNA fingerprinting from cells captured by laser microdissection. *Methods in Enzymology* 356, 289–294.
- Sokabe, M., Sachs, F., Jing, Z., 1991. Quantitative video microscopy of patch clamped membranes stress, strain, capacitance, and stretch channel activation. *Biophysical Journal* 59, 722–728.
- Speckman, R. A., Garg, A., Du, F. H., Bennett, L., Veile, R., Arioglu, E., Taylor, S. I., Lovett, M., Bowcock, A., 2000. Mutational and haplotype analyses of families with familial partial lipodystrophy (Dunnigan variety) reveal recurrent missense mutations in the globular C-terminal domain of lamin A/C. *American Journal of Human Genetics* 66, 1192–1198.
- Stoltz, J. F., Wang, X., 2002. From biomechanics to mechanobiology. *Biorheology* 39, 5–10.

- Stuurman, N., Heins, S., Aebi, U., 1998. Nuclear lamins: their structure, assembly and interactions. *Journal of Structural Biology* 122, 42–66.
- Sullivan, T., Escalante-Alcalde, D., Bhatt, H., Anver, M., Bhat, N., Nagashima, K., Stewart, C. L., Burke, B., 1999. Loss of A-type lamin expression compromises nuclear envelope integrity leading to muscular dystrophy. *Journal of Cell Biology* 147, 913–920.
- Takamatsu, H., Kumagai, N., 2002. Survival of biological cells deformed in a narrow gap. *Journal of Biomechanical Engineering* 124, 780–783.
- Takamatsu, H., Rubinski, B., 1999. Viability of deformed cells. *Cryobiology* 39, 243–251.
- Theret, D. P., Levesque, M. J., Sato, M., Nerem, R. M., Wheeler, L. T., 1988. The application of a homogeneous half-space model in the analysis of endothelial cell micropipette measurements. *Journal of Biomechanical Engineering* 110, 190–199.
- Thoumine, O., Carodoso, O., 1999. Changes in the mechanical properties of fibroblasts during spreading: a micromanipulation study. *European Biophysical Journal* 28, 222–234.
- Thoumine, O., Meister, J.-J., 2000. Dynamic and adhesive rupture between fibroblasts and fibronectin: microplate manipulations and deterministic model. *European Biophysical Journal* 29, 409–419.
- Thoumine, O., Ott, A., 1997a. Comparison of the mechanical properties of normal and transformed fibroblasts. *Biorheology* 34, 309–326.
- Thoumine, O., Ott, A., 1997b. Time scale dependent viscoelastic and contractile regimes in fibroblasts probed by microplate manipulation. *Journal of Cell Science* 110, 2109–116.
- Thoumine, O., Ott, A., 1999. Biomechanical properties of fibroblasts. *MRS Bulletin* 24 (10), 22–26.
- Thoumine, O., Ott, A., Cardoso, O., Meister, J., 1999. Microplates: a new tool for manipulation and mechanical perturbation of individual cells. *Journal of Biochemical and Biophysical Methods* 39, 47–62.
- Tran-Son-Tay, R., 1993. Techniques for studying the effects of physical forces on mammalian cells and measuring cell mechanical properties. In: Frangos, L. A. (Ed.), *Physical forces and the mammalian cell*, 1st Edition. Academic Press, Inc., London, Ch. 1, pp. 1–59.
- Vandenburgh, H. H., 1992. Mechanical forces and their second messengers in stimulating cell growth in vitro. *American Journal of Physiology* 262, R350–R355.

- Venables, R. S., McLean, S., Luny, D., Moteleb, E., Morley, S., Quinlan, R. A., Lane, E. B., Hutchison, C. J., 2001. Expression of individual lamins in basal cell carcinomas of the skin. *British Journal of Cancer* 84, 512–519.
- Vesenka, J., Mosher, C., Schaus, S., Ambrosio, L., Henderson, E., 1995. Combining optical and atomic force microscopy for life sciences research. *Biotechniques* 19, 240–253.
- Visser, T. D., Oud, J. L., Brakenhoff, G. J., 1992. Refractive index and axial distance measurements in 3D microscopy. *Optik* 90, 17–19.
- Wang, N., Butler, J. P., Ingber, D. E., 1993. Mechanotransduction across the cell surface and through the cytoskeleton. *Science* 260, 1124–1127.
- Wang, N., Ingber, D. E., 1994. Control of cytoskeletal mechanics by extracellular matrix, cell shape and mechanical tension. *Biophysical Journal* 66, 2181–2189.
- Watson, P. A., 1991. Function follows form: generation of intracellular signals by cell deformation. *FASEB Journal* 5, 2013–2019.
- Wilson, T., 1989. Optical sectioning in confocal fluorescent microscopes. *Journal of Microscopy* 154, 143–156.
- Worman, H. J., Courvalin, J. C., 2002. The nuclear lamina and inherited disease. *Trends in Cell Biology* 12, 591–598.
- Wu, J. Z., Herzog, W., 2000. Finite element simulation of location- and time-dependent mechanical behaviour of chondrocytes in unconfined compression tests. *Annals of Biomedical Engineering* 28, 318–330.
- Wu, Z.-Z., Zhang, G., Long, M., Wang, H.-B., Song, G.-B., Cai, S.-X., 2000. Comparison of the viscoelastic properties of normal hepatocytes and hepatocellular carcinoma cells under cytoskeletal perturbation. *Biorheology* 37, 279–290.
- Yamada, K. M., Miyamoto, S., 1995. Integrin transmembrane signaling and cytoskeletal control. *Current Opinion in Cell Biology* 7, 681–689.
- Yamada, S., Wirtz, D., Kuo, S. C., 2000. Mechanics of living cells measured by laser tracking microrheology. *Biophysical Journal* 78, 1736–1747.
- Yoshikawa, Y., Yasuike, T., Yagi, A., Yamada, T., 1999. Transverse elasticity of myofibrils of rabbit skeletal muscle studied by atomic force microscopy. *Biochemical and Biophysical Research Communications* 256, 13–19.
- You, H. X., Lau, J. M., Zhang, S., Yu, L., 2000. Atomic force microscopy imaging of living cells: a preliminary study of the disruptive effect of the cantilever tip on cell morphology. *Ultramicroscopy* 82, 297–305.

- Zhang, Q., Ragnauth, C., Greener, M. J., Shanahan, C. M., Roberts, R. G., 2002. The nesprins are giant actin-binding proteins, orthologous to *Drosophila melanogaster* muscle protein MSP-300. *Genomics* 80, 473–481.
- Zhang, Q., Skepper, J. N., Yang, F., Davies, J. D., Hegyi, L., Roberts, R. G., Weissberg, P. L., Ellis, J. A., Shanahan, C. M., 2001. Nesprins: a novel family of spectrin-repeat-containing proteins that localize to the nuclear membrane in multiple tissues. *Journal of Cell Science* 114, 4485–4498.
- Zhang, Z., Ferenczi, M. A., Lush, A. C., Thomas, C. R., 1991. A novel micromanipulation technique for measuring the bursting strength of single mammalian cells. *Applied Microbiology and Biotechnology* 36, 208–210.
- Zhang, Z., Ferenczi, M. A., Thomas, C. R., 1992. A micromanipulation technique with a theoretical cell model for determining mechanical properties of single mammalian cells. *Chemical Engineering Science* 6, 1347–1354.
- Zhen, Y. Y., Libotte, T., Munck, M., Noegel, A. A., Korenbaum, E., 2002. NUANCE, a giant protein connecting the nucleus and actin cytoskeleton. *Journal of Cell Science* 115, 3207–3222.
- Zhu, C., Bao, G., Wang, N., 2000. Cell mechanics: mechanical response, cell adhesion, and molecular deformation. *Annual Review of Biomedical Engineering* 2, 189–226.

Samenvatting

Eukaryotische cellen reageren actief op mechanische stimuli. Deze stimuli en de bijbehorende celvervormingen veroorzaken een aantal verschillende biologische processen, zoals morfologische veranderingen, differentiatie, veranderingen in genexpressie en eiwitsynthese. Het onderzoeksgebied celbiomechanica behelst hoe cellen bewegen, vervormen, op elkaar inwerken, alsmede hoe ze mechanische stimuli voelen, genereren en daarop reageren. Celbiomechanica wordt bestudeerd door gebruik te maken van verschillende experimentele technieken en computermodellen. Vervormingen worden aangebracht op specifieke delen van de cel (lokale vervorming) of op de gehele cel (globale vervorming).

In dit proefschrift wordt de biomechanica van gehechte cellen onderzocht. Deze cellen zijn verankerd aan een substraat *in vitro* en aan de extracellulaire matrix *in vivo*. Daarom is een nieuw belastingsapparaat ontwikkeld om individuele, gehechte cellen samen te drukken. Cellen kunnen zowel statisch als dynamisch belast worden, terwijl de bijbehorende krachten gemeten worden. Met dit apparaat kunnen de globale mechanische eigenschappen van de cel onderzocht worden. Het belastingsapparaat heeft als voordeel dat de kweekomstandigheden tijdens samendrukken optimaal zijn. De mechanische eigenschappen van cellen kunnen daarom onder fysiologische omstandigheden geëvalueerd worden, met de mogelijkheid om lange termijn experimenten uit te voeren. In dit proefschrift wordt de biomechanische respons van gehechte cellen onderzocht en toegepast op twee verschillende klinische problemen, waarbij mechanische factoren en vooral de biomechanica van cellen een belangrijke rol spelen. De eerste toepassing richt zich op decubitus en de tweede op laminopathieën.

Doorligwonden zijn pijnlijk, moeilijk te behandelen en vormen een belangrijke kostenpost ten aanzien van de gezondheidszorg in vele landen. Ondanks het gegeven dat decubitus ontstaat door een langdurige mechanische belasting, is de etiologie van decubitus nog lang niet duidelijk. In dit proefschrift worden spiercellen bestudeerd, omdat met name spierweefsel gevoelig is voor compressie en de meest problematische doorligwonden vaak in diepliggende spierlagen ontstaan. Om de mechanobiologische paden die tot schade leiden te begrijpen, is het belangrijk om de biomechanische respons van afzonderlijke spiercellen tijdens compressie te bestuderen. Dit onderzoek legt de nadruk op de vervorming en het mechanisch gedrag van spiercellen tijdens compressie. Met behulp van driedimensionale beelden, verkregen tijdens stapsgewijze compressie van cellen, zijn verschillende geometrische parameters berekend om

celvorming te kunnen kwantificeren. Deze parameters zijn nuttig voor het bepalen van drempelwaarden voor celschade bij een bepaalde mate van celvorming. De experimenten toonden aan dat de cel en de celkern loodrecht op de lengteas vervormen, indien de gehechte cel een voorkeursoriëntatie heeft. Deze anisotrope vervorming kan wellicht veroorzaakt worden door georiënteerde actine vezels, die indirect verbonden zijn met de celkern en het onderliggende substraat.

Om het mechanisch gedrag te kunnen karakteriseren, zijn er twee soorten experimenten uitgevoerd. In het eerste experiment werd de gehele cel in 15 seconden gecompriëerd. Dit leverde een niet-lineair kracht indentatie verband op, waaruit de knapsterkte, de bijbehorende axiale vervorming en een eerste afschatting van de Youngs modulus bepaald konden worden. In de tweede serie experimenten werden cellen dynamisch belast om het viscoelastische gedrag te onderzoeken. Een niet-lineair viscoelastisch model werd gebruikt om dit gedrag te beschrijven. Samenvattend beschreven deze experimenten de elastische en viscoelastische eigenschappen van cellen en zullen dienen als input voor computermodellen van natuurlijke of artificiële weefsels. Uiteindelijk zullen deze modellen celvormingen en mogelijke schade of adaptatie beschrijven ten gevolge van weefsel compressie, zoals bij decubitus het geval is.

Laminopathieën zijn erfelijke ziektes die veroorzaakt worden door mutaties in het lamine A/C (LMNA) gen. Voorbeelden hiervan zijn Emery Dreifuss spierdystrofie, gedilateerde cardiomyopathie en gedeeltelijke vetdystrofie. Ondanks dat de onderliggende mechanismen van deze ziektes vrijwel onbekend zijn, worden er twee mogelijke hypothesen gehanteerd. De eerste hypothese stelt dat mutaties in A-type lamines afwijkingen in genexpressie veroorzaken. De tweede stelt dat patiënten met laminopathieën mechanisch verzwakte cellen hebben door afwijkingen in de structuur van de celkern. Deze laatste hypothese is getoetst met behulp van het belastingsapparaat. Wild-type en LMNA knock-out muis fibroblasten werden vergeleken en een significant verhoogde mechanische weerstand tegen deformatie van wild-type cellen werd aangetoond. Confocaal microscopie toonde aan dat de kernen van LMNA knock-out cellen, in tegenstelling tot de kernen van wilde-type cellen, ernstig beschadigd waren na compressie. Een andere belangrijke bevinding was de anisotrope kernvorming van wild-type cellen. De kernen van knock-out cellen vervormden isotroop. Er werd verondersteld dat dit verschil te wijten was aan een verstoorde verankering van de kern aan het actine cytoskelet. Visualisatie van actine filamenten toonde een verstoord actine cytoskelet aan rond de kern van knock-out cellen en bevestigde daarmee dit vermoeden. Op deze manier werd de relatie tussen de afwezigheid van LMNA eiwitten en celkwetsbaarheid gelegd, en werd de hypothese ondersteund.

Concluderend kan worden gesteld dat het belastingsapparaat en de experimentele technieken bewezen hebben een nuttige bijdrage te leveren om celbiomechanica in het algemeen en de etiologie van doorligwonden en laminopathieën in het bijzonder, te bestuderen.

Dankwoord

Graag wil ik een aantal mensen bedanken zonder wie dit proefschrift niet geworden zou zijn wat het nu is. Allereerst wil ik Cees en Carlijn bedanken. Samen bestreken jullie een enorm kennisgebied, waar ik ruim van heb mogen profiteren. Bedankt voor jullie betrokkenheid, enthousiasme en motiverende gesprekken. Frank Baaijens wil ik bedanken voor het mogelijk maken van dit onderzoek, de inhoudelijke bijdrage en natuurlijk voor het kerstmodel. I would also like to thank Dan Bader for the fruitful discussions on my thesis, science and life in general. It has been a pleasure working with you. Luc Snoeckx, bedankt voor de plezierige samenwerking en de begeleiding van mijn afstudeerder. En natuurlijk zal ik Jos Broers niet vergeten die mij vroeg experimenten te doen op lamine deficiënte cellen. Dit was het begin van een prachtig onderzoek. Ik waardeer je onderzoeksgretigheid en je onuitputtelijke motivatie.

En natuurlijk mag ik 'de mannen van de werkplaats' en in het bijzonder Rob van den Berg niet vergeten. Dankzij hun koffie en vakmanschap werkt het belastingsapparaat zoals het zou moeten werken. Tevens wil ik Frans Kuijpers graag bedanken voor het maken van de veel te kleine stempeltjes om mijn cellen in te kunnen drukken. Leo en Patrick, bedankt voor de geboden eerste hulp bij al mijn computerproblemen. Willem-Pier, Leon, Gerrit, Mark, Ralf en Marcel (alle drie): bedankt voor de vele nuttige discussies. I would like to thank Zhibing Zhang for the interesting discussions on micromanipulation and for giving me the opportunity to visit his lab. Natuurlijk mag ik de AIO's van het hele decubitus team niet vergeten: Roel, Mariëlle, Debby en Anke.

Afstudeerder Roel en stagiair Ivo wil ik graag bedanken voor hun inspanningen. Ik kan wel zeggen dat jullie jezelf als pioniers mogen beschouwen. Martijn Cox wil ik bedanken voor het schrijven van het businessplan. De collega's, maar natuurlijk mijn kamergenoten van de family-room 4.105 Leonie, Mascha, Roy, Debby en Katy wil ik bedanken voor alle rariteiten, discussies en white-board onzin. Zonder mijn vrienden was deze promotie zeker een stuk minder leuk geworden. Bedankt voor de uitlaatkleppen op allerlei gebied. Jullie weten wel wat ik bedoel.

Tenslotte wil ik mijn ouders en mijn broer bedanken voor de onvoorwaardelijke steun, heerlijke etentjes en vooral de gesprekken daarna. En natuurlijk Debby. Jij kan altijd een lach op mijn gezicht toveren en bent er het laatste jaar altijd voor me geweest. Ik zal het natuurlijk onthouden, want over een kleine drie jaar ben jij aan de beurt..

Emiel Peeters,
Eindhoven, januari 2004

Curriculum Vitae

Emiel Peeters werd geboren op 25 maart 1975 in Geldrop. Na zijn VWO diploma behaald te hebben in 1993 aan het Anton van Duinkerken College te Veldhoven, heeft hij in 1994 zijn propedeuse Werktuigbouwkunde behaald aan de Technische Universiteit Eindhoven. Vanwege zijn interesses op het gebied van biologie, wiskunde en natuurkunde heeft hij vervolgens gekozen voor de postpropedeutische opleiding Werktuigkundige Medische Technologie. Als deel van zijn studie heeft hij een stage gevolgd aan de Queen Mary University of London. Daar is zijn interesse ontstaan voor celbiomechanica. In juni 1999 studeerde hij af op een project wat tot doel had om een vaatprothese te ontwikkelen met dezelfde mechanische eigenschappen als een natuurlijk bloedvat. Door zijn blijvende interesse voor celbiomechanica en de komst van het laboratorium voor celmechanica en tissue engineering aan de faculteit Biomedische Technologie begon hij in 1999 met zijn promotieonderzoek, waarvan dit proefschrift het resultaat is.